MSc thesis

Numerical modelling of internal waves in the Browse Basin

C.M. Van der Boon

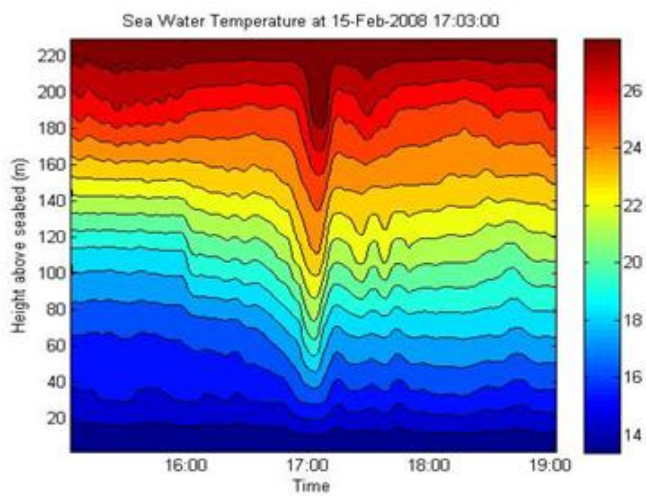

Graduation committee:

Prof. Dr. J.D. Pietrzak (TU Delft)
J.Flynn (Senior Metocean Engineer Shell)
Dr. Ir. R.J. Labeur (TU Delft)
Prof. Dr. Ir. G.S. Stelling (TU Delft)
Prof. Dr. Ir. M.J.F. Stive (TU Delft)
Prof. Dr. K.G. Lamb (University of Waterloo)

Delft, October 2011

Summary

Shell is developing a floating liquefied natural gas (FLNG) facility named Prelude to extract and process natural gas in the Browse Basin on the North West Shelf of Australia. This shelf break area is known for its strong tidal currents and year-round stratification. Tidal currents transporting stratified water over steep bathymetry can generate large internal waves called solitary waves (sometimes called solitons). A field survey in the Browse Basin commissioned by Shell showed that internal solitary waves have passed the Prelude location on several occasions. Solitons are known to have severely disrupted offshore operations in other areas in the past. In the case of the Prelude FLNG project, the production risers, steel tubular water intake risers and mooring chains can all be subject to fatigue or clashing due to internal wave events. The safety and effectiveness of the FLNG project can be improved if it is possible to forecast when solitons will occur and what their magnitude will be.

For that reason, Shell wants to use a numerical model that is capable of predicting the internal wave activity in the Browse Basin. Finlab is a non-hydrostatic, finite element model that solves the full Navier-Stokes equations on unstructured grids. It was designed for small-scale flow problems with complex topography. However it has never been extensively tested for internal flow problems.

Therefore, the objectives of this project are to investigate whether Finlab can be used for the numerical simulation of internal waves in the Browse Basin and to gain a better understanding of internal wave dynamics in the Browse Basin through data analysis and numerical simulations.

Two published laboratory test cases of internal waves are simulated with Finlab. This is done to assess the capabilities and limitations of the model. The first test case consists of a two-layer fluid with a tilted interface in a closed tank. The second test studies the generation of lee waves by two-layer flow over a small bottom obstacle. The model is validated by comparing the numerical and laboratory results. Very good agreement was observed. Especially the results of the tilting tank experiment were very accurate. However, the computed waves had small amplitude and phase errors when compared to the laboratory data. A likely cause for the time lags is diffusion of the interface which is considerably larger in the numerical tests than in the laboratory tests. For enough accuracy, a high resolution grid is required. Some difficulties were experienced with the open outflow boundary during the lee wave experiment as it influenced the flow upstream. Extending the numerical domain solved this problem.

The field data collected by Shell is analyzed to gain a better understanding of the internal wave dynamics in the Browse Basin. Large internal solitary waves were observed 12-15 times per year with amplitudes of 30-50 m and wave periods of 15-30 min. Most solitons occurred 1-3 days before neap tide. A clear generation mechanism has not been found, but it is hypothesized that the solitons are generated by the steepening of the baroclinic tide over the steep shelf break. Three dimensional effects are assumed to play an important role.

The results from the data analysis and model validation are combined to simulate a number of Browse Basin scenarios. The stratification used in the numerical study is based on measured density profiles.

The shelf is modelled from the deep ocean (5500 m water depth) to 100 m water depth. A tidal velocity is imposed at the deep-water boundary and results in the generation of an internal tide that steepens towards the shallower part of the domain. However, due to a limitation of the mesh generator, the resolution of this grid was not high enough to capture the generation of internal solitary wave packets from this steepening effect.

Simplified cross-sections of the Browse Basin near Scott Reef and Seringapatam Reef are modelled. Located some 150 km west of Prelude, the shorter two-dimensional cross-sections could be modelled with a higher resolution than the entire shelf itself. Simulation results now showed packets of solitons generated near the top of the reef and propagating away in opposite directions. A tidal velocity was used at the deep-water open boundary which resulted in the generation of wave packets every tidal cycle.

Overall, it can be concluded that Finlab is capable of simulating internal waves in two-dimensional sections (300-500 km length) of the Browse Basin. Requirements for the resolution and time step for simulations of Browse Basin scale have been found. The mesh generator became a critical limiting factor for this study because it was not possible to get a high enough resolution on the shelf.

Scott Reef and Seringapatam Reef have been identified as likely generation areas of internal wave packets. Further simulations taking the Coriolis force, deep water stratification and three-dimensional bathymetric and tidal effects into account should be set up to verify this hypothesis. Simulations on finer grids are necessary to study the generation of solitary internal waves on the shelf.

Acknowledgements

This report is the outcome of my MSc graduation project at Delft University of Technology. The research has been carried out at Shell Global Solutions under the guidance of the section of Environmental Fluid Mechanics at the Faculty of Civil Engineering.

I would like to thank my daily supervisors Jan Flynn and Julie Pietrzak for their guidance and feedback during this project. I would also like to thank Robert Jan Labeur for all his help and patience when I was learning how to use the numerical model and Guus Stelling, Kevin Lamb and Marcel Stive for their valuable advice and ideas about the project. Furthermore I want to thank Octavio Sequeiros from Shell Metocean for all his help with Linux and Matlab.

Many thanks go to the Shell Metocean team and my fellow interns at Shell, as they made my time there very interesting and very enjoyable.

Delft, October 2011,

Mariska van der Boon

Table of contents

Chapter 1 – Introduction

1.1 Context

Shell Development Australia Proprietary Limited (SDA) proposes to develop the Prelude gas reserves in the Browse Basin, 400 km off the Kimberley coast, Western Australia (see Figure 1). Shell is the 100% equity holder and operator of the WA-371-P permit, an area which covers around 1000 square kilometres in the Browse Basin. During 2007, Shell discovered the Prelude gas field and in March 2009 discovered the ''Concerto'' gas field in the permit area.

Figure 1. Left: Browse Basin. (Source: maps.google.com). Right: Artist impression of the FLNG facility. (Source: shell.com.au).

A Floating Liquefied Natural Gas (FLNG) facility (Figure 2) is being developed to process natural gas and condensate in this area. The facility processes gas entirely offshore. This avoids the need for export pipelines, an onshore liquefaction plant and export jetties and therefore reduces both the project costs and the environmental footprint of LNG development compared to traditional development methods. FLNG technology is particularly suitable in remote areas such as the Browse Basin.

The Prelude FLNG facility will be approximately 480 m long and 75 m wide. It will be moored at the gas field location during the entire period of production in water depths of 250 m.

The development of the FLNG facility comprises a series of subsea wells tied back to the barge via flexible risers. Furthermore, twelve tubular water intake risers will provide cooling water for LNG processing and four bundles of six steel catenary mooring chains provide the mooring of the vessel to the seabed.

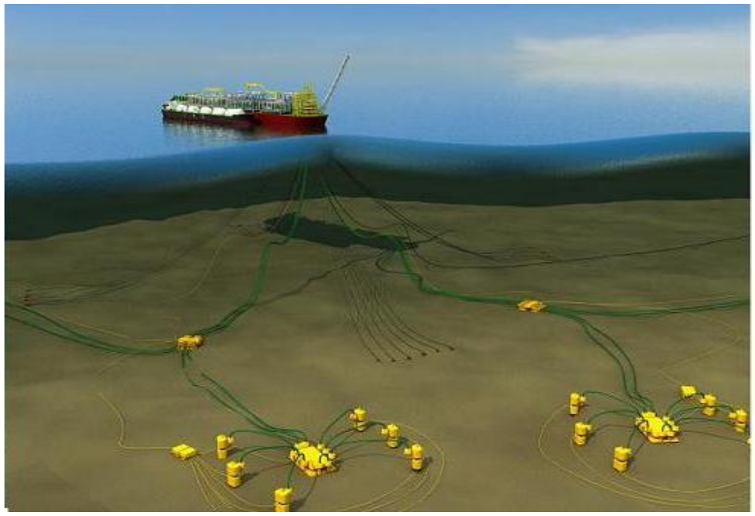

Figure 2. Subsea FLNG equipment. (Source: www.projectconnect.com.au).

The Prelude FLNG facility is designed to withstand a 1 in 10000 year tropical cyclone and has an estimated operational lifetime of 25 years. It is scheduled to start production in 2016. The facility will be capable of producing around 3.6 million tonnes of LNG, 1.3 million tonnes of condensate and 0.4 million tonnes of Liquefied Petroleum Gas per year.

There are currently no FLNG facilities deployed anywhere in the world.

1.2 Problem definition

Shell Development Australia Pty Ltd commissioned a survey to provide the metocean design criteria for the Prelude FLNG project. For two and a half years (2007-2010), meteorological and oceanographic conditions in one location in the Browse Basin were recorded. From this data set, the operational design conditions were derived.

The data showed that tropical cyclones dominate the extreme metocean environment near Prelude. Three to five tropical storms per year pass through the Browse Basin. The area also knows strong tidal currents and an intense thermocline (Van Gastel et al.(2009). This provides good conditions for the generation and propagation of solitary internal waves, called solitons (Vlasenko et al. 2005). These are waves that travel beneath the water surface and cause sudden increases in current speed, accompanied with sudden temperature changes in the water column.

The survey instruments were able to capture soliton activity. Current meters had a high sampling rate of 1 minute. Several events with current speed spikes and sudden temperature changes were observed during the measuring period. This indicates that solitons do indeed occur in the Browse Basin area.

The increased velocity and shear associated with solitons have severely disrupted offshore operations in the past. This led to an expensive loss of work time and assets (Goff et al. 2010). In the case of the Prelude FLNG project, the production risers, steel tubular water intake risers and mooring chains can all be subject to fatigue or clashing due to soliton events. The safety and effectiveness of the FLNG project can be improved if it is possible to forecast where and when these waves will occur and how large the maximum currents and shear over the vertical may be.

Although two and a half years is relatively long for a measurement survey, it does not provide enough information to predict the frequency of occurrence and the magnitude of solitons in the Browse Basin for the FLNG operational lifetime of 25 years. Therefore, Shell wants to develop a numerical model that is able to resolve the baroclinic tidal forcing and soliton activity in the Browse Basin. The field data collected by Shell can be used to validate the model. It can then be run over a longer timescale to predict the frequency of occurrence and intensity of solitons in the Prelude area.

1.3 Goals

The long term goal of this project is to develop a numerical tool that can predict the frequency of occurrence and intensity of solitons in the Browse Basin area. The NWS has been the focus area of many field and numerical studies on internal wave activity. Most were focused on the interaction of baroclinic and barotropic tidal motions with bathymetry. Hydrostatic models can be used for this. This thesis will focus on the shorter waves that are generated when the baroclinic tide propagates onto the shelf. Non-linear effects become important on the shelf slope and hydrostatic models can no longer be used. Finlab is a non-hydrostatic, finite-element model that was designed for small-scale flow problems with complex topography. It might be very suitable for this project but has not yet been tested extensively for density-driven, subsurface flow problems. Within the framework of the project goal set by Shell, the objective of this Master thesis is to investigate whether or not the numerical model Finlab can be used for the numerical simulation of internal solitary waves. The scientific goal of this MSc thesis is to gain a better understanding of the internal wave dynamics in the Browse Basin through data analysis and numerical simulations.

The objectives can be reached by finding answers to the following questions:

1. What are the capabilities and limitations of the numerical model in simulating internal solitary waves?
2. What can be understood from the data regarding internal wave characteristics in the Browse Basin?
3. What can be understood from the numerical simulations regarding generation, propagation and transformation of internal waves in the Browse Basin?

1.4 Approach

To answer the questions formulated in paragraph 3, a number of steps must be taken. First, a literature study is undertaken to gain a general understanding of the physical processes that are important in the Browse Basin and the specific conditions under which internal solitary waves are generated.

The next step is to investigate if the numerical model Finlab can resolve the physical parameters in the Browse Basin. Finlab is a non-hydrostatic, finite element model that may be suitable for modelling internal solitary waves. To gain better insight into its capabilities and limitations, several validation tests will be done.

Next, the data from the Shell met-ocean survey are analyzed. The soliton events will be filtered from the data by looking for high current speeds accompanied with rapid temperature changes. The correlations of the occurrence of solitons with the tidal cycle and the stratification will be investigated.

The analyzed data and bathymetry will then be used to simulate (in two dimensions) some of the wave characteristics found in the data. The numerical results will be compared to the data. While these tests miss important details of the three-dimensional flows, this is a first step in the direction of simulating internal solitary waves in the Browse Basin. The two-dimensional simulations presented here allow us to investigate the grid resolution and time step needed to resolve solitons in the Browse Basin. If the two-dimensional simulations show a reasonable resemblance to the observations and known physics, it can be assumed that it is worth taking the next step and investing in three-dimensional simulations. The numerical set up can then be used for future, more complex simulations of internal wave activity in the Browse Basin.

The model validation, data analysis and Browse Basin simulations will provide a solid basis for further development of the numerical model, i.e. expansion into three-dimensions and running over longer timescales. They will also provide more insight into the characteristics of internal solitary waves in the Browse Basin.

1.5 Thesis outline

This report is organized as follows. Chapter 1 serves as an introduction to the subject in which the context and goals of the project are explained.

Chapter 2 gives a description of the bathymetry and the oceanographic conditions in the Browse Basin based on previous research in the area and a first analysis of the field data collected by Shell.

Chapter 3 discusses the theoretical background of internal wave dynamics that is required to understand the generation and propagation mechanisms of internal solitary waves.

In chapter 4, a description of the numerical model Finlab is given and the parameters that are important for the model validation are introduced.

Chapter 5 gives an overview of the validation tests that were performed and discusses the capabilities and limitations of Finlab.

In chapter 6, the met-ocean data is analyzed by looking at the temperature profiles and current speeds in the entire water column and the influence of the tidal cycle and the stratification.

Simulation results of the Browse Basin solitons are shown and analyzed in chapter 7.

A discussion on the assumptions made for the numerical simulations and their justification is presented in chapter 8.

In chapter 9, general conclusions of the project are discussed and recommendations for further research are proposed.

Chapter 2 – Oceanographic conditions in the Browse Basin

2.1 Introduction

The Browse Basin is located on the Australian North West Shelf (NWS) and this area has been the subject of considerable scientific research on internal tide and internal wave dynamics (Apel 2002). Studies include satellite observations (Baines 1981), field measurements (Holloway and Chatwin 2000); (Bluteau et al. 2010; Rayson et al. 2011) and numerical studies (Holloway 1996); Rayson, Ivey et al. 2011). The area of focus of these studies was mainly in the southern part of the NWS (Dampier, North Rankin, see Figure 3) although island generated internal waves were studied near Scott Reef (Wolanski and Deleersnijder 1998) and more recently numerical and field research was started in the Browse Basin (Rayson et al. 2011).

In this section, the previously studied oceanographic features in the Browse Basin will be discussed. The information comes from previous field studies and the SDA commissioned field study.

2.2 The Australian NWS and the Browse Basin

The North West Shelf of Western Australia is located in the Indian Ocean between North West Cape and Dampier. It is an extensive oil and gas region.

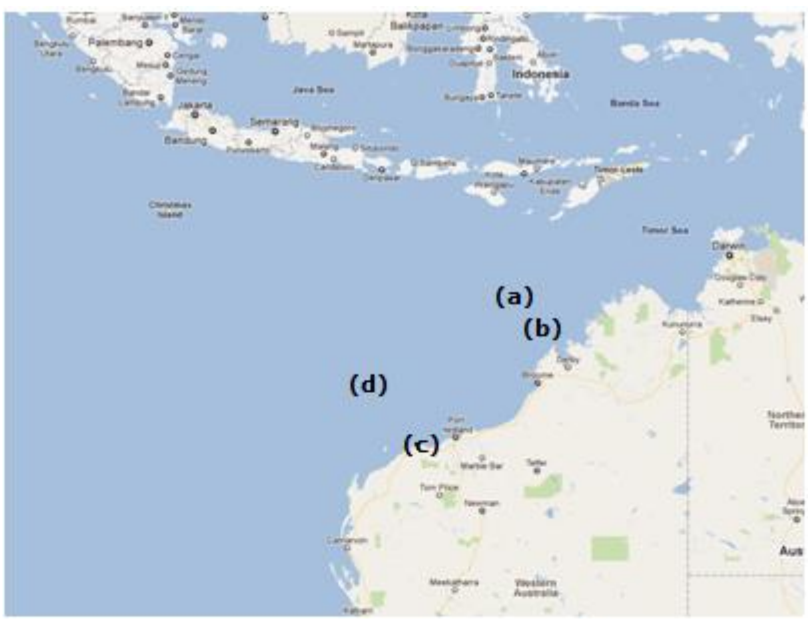

Figure 3. (a) Scott Reef, (b) Prelude, (c) Dampier, (d) North Rankin (Source: Google Maps).

The Browse Basin is a large, offshore basin of approximately 185,000 square kilometres in the northern part of the NWS. It has a complex topography (Rayson et al. 2011). Water depths in the basin range from 20 to 2000 m. The Browse Basin has an inner shelf break with a slope of 0.5-1.0% and an outer shelf break with a slope of 3-4%.

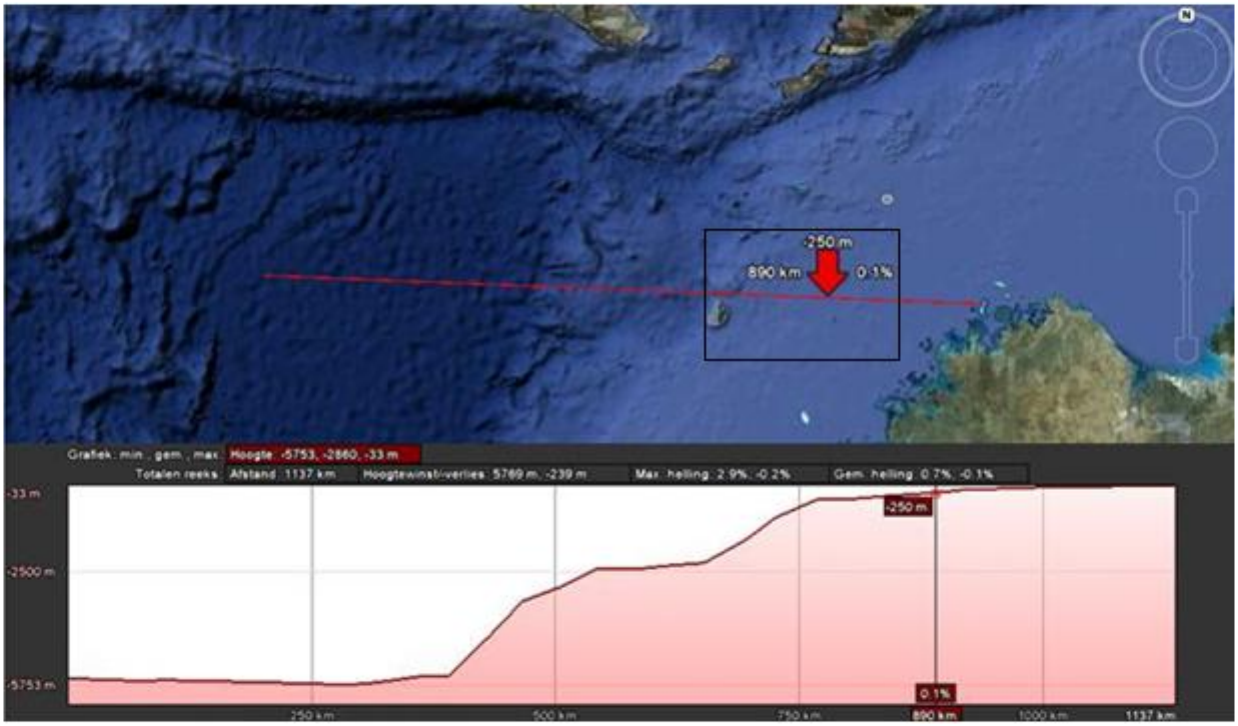

Figure 4. Shelf break topography with FLNG location (red arrow) and Browse Basin (black box). (Source: Google Maps).

2.3 Oceanographic conditions

The area has an energetic oceanographic environment (Condie and Andrewartha 2008). The region has large tides (amplitudes of 4 m in some regions) decreasing in amplitude from north to south (Marine and Biodiversity Division 2008). Also, cyclones and strong regional currents play an important role. The cyclone season is from November to April with a peak in January and the most severe storms occurring in December and March-April. Wind driven current speeds of 0.7 m s^{-1} have been observed (Flynn 2010).

The ocean currents on the North West Shelf change between seasons and between years (Marine and Biodiversity Division 2008). The major currents include the Indonesian Throughflow, the Leeuwin Current, the South Equatorial Current and the Eastern Gyral Current. The regional circulation is schematized in Figure 5. See (Condie and Andrewartha 2008) for a description of the regional scale flows in the region.

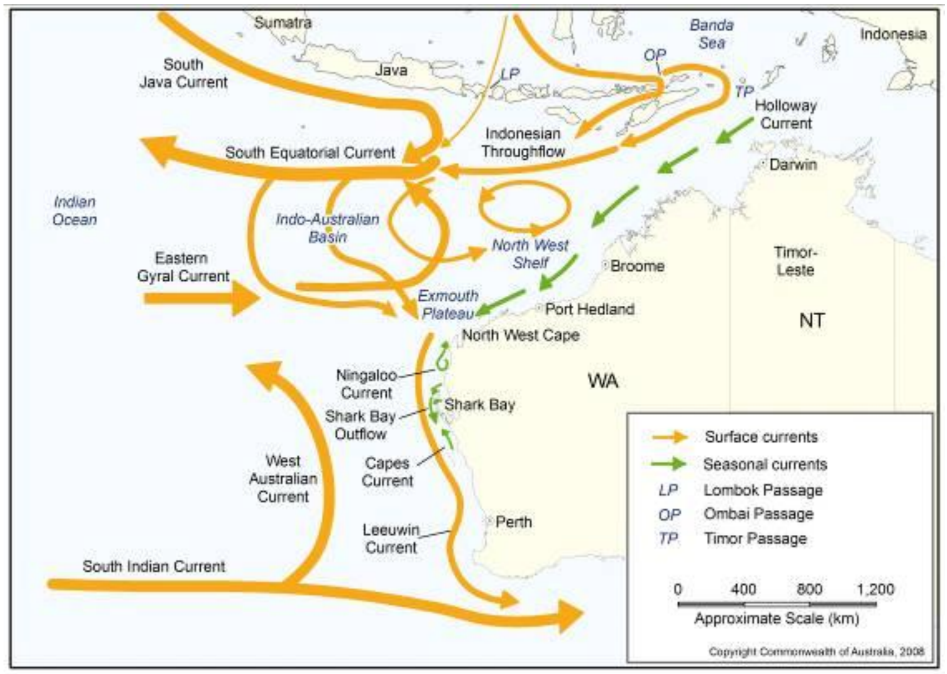

Figure 5. Surface current influencing the NWS. Reproduced from National Oceans Office (2008).

The tides are predominantly semidiurnal with a small diurnal inequality (Van Gastel et al. 2009). The tidal components M2 and S2 are dominant (Holloway 1994) and tidal amplitudes reach 4 m at the Prelude location (Flynn 2010). Wolanski and Deleersnijder (1998) studied field data collected at Scott Reef (some 150 km from Prelude) and found a spring tide of 4 m and a neap tide of 1 m. Strong reversing tidal currents were observed with maximum speeds of 0.7 m/s.

Tidal Level	Symbol	Elevation (m relative to LAT)
Highest astronomical tide	HAT	5.089
Mean High Water Spring	MHWS	4.784
Mean Higher High Water	MHHW	4.092
Mean Lower High Water	MLHW	3.703
Mean High Water Neap	MHWN	3.278
Mean Sea Level	MSL	2.515
Mean Low Water Neap	MLWN	1.764
Mean Higher Low Water	MHLW	1.272
Mean Lower Low Water	MLLW	0.919
Mean Low Water Spring	MLWS	0.264
Lowest Astronomical Tide (Chart Datum)	LAT (CD)	0.000

Figure 6. Tidal elevations at Prelude relative to Lowest Astronomical Tide (LAT). From: Metocean Reference Document.

The tidal currents are predominantly in the cross-shelf direction (Marine and Biodiversity Division 2008). Water in the Browse Basin is stratified throughout the year due to strong solar heating and low precipitation in the region (Van Gastel et al. 2009). In addition to the heating of surface water through solar activity, the Indonesian Through flow and the Leeuwin Current transport warm water along the outer NWS.

The F-Block data set showed that the water temperature ranges on average from 13^{o}C near the ocean bottom (water depth of 257 m) to 30^{o}C at the water surface. The largest seasonal variations occur in the first 150 m of water below the sea surface. The salinity does not vary significantly during the year (no more than 0.2 PSU), nor is there a large variation of salinity with depth (no more than 0.4 PSU). On average the salinity is 34.6 PSU.

The density in the water column was calculated from the observed temperature data (and a constant salinity of 34.6 PSU) by means of the equation of state as formulated by Mellor (1996). The monthly average was taken in each water depth and the density difference between the water at the surface and near the bottom was calculated. Results are shown in Figure 7. The yearly averaged density difference is 5.2 kg/m^3. The stratification is most pronounced in November, December, March and April. During the winter months (June to September), the thickness of the upper mixed layer increases and the thermocline is located deeper down.

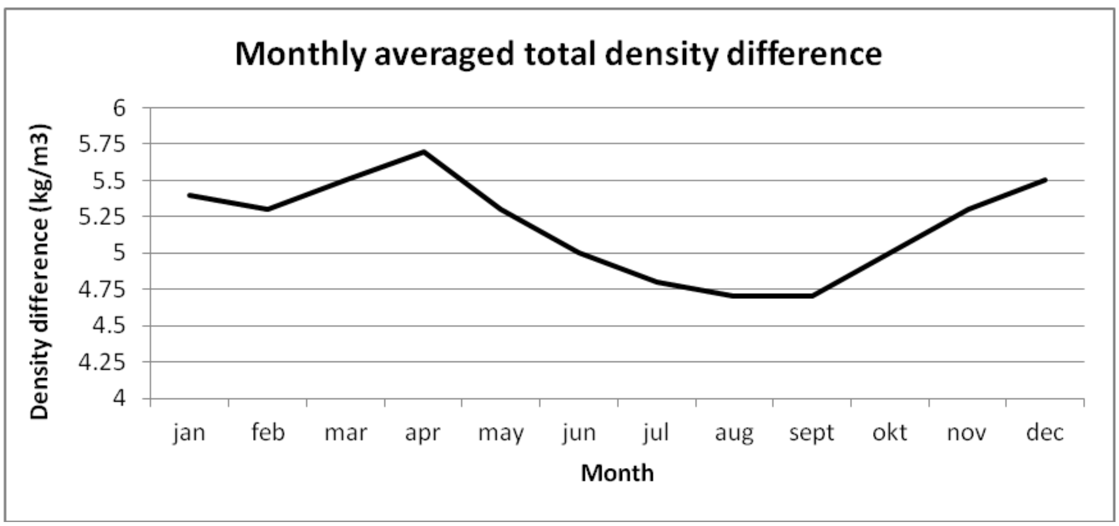

Figure 7. Bottom to surface density difference over the year. Based on Shell field data.

2.4 Internal wave observations

The interaction of barotropic tidal currents with sloping topography in stratified waters can generate an internal tide (Van Gastel et al. 2009). Observations by Holloway (1983, 2001) have shown that the North West Shelf is such an area. He suggests that the slope in water depths of 400-1000 m generates a strong barotropic tide with a semidiurnal spring-neap cycle.

The nonlinear steepening of the internal tide may generate short internal solitary waves. These short waves are the topic of this study and their generation mechanisms will be discussed in more detail in chapter 3. Changes in topography at 125 m and 200 m water depths on the North West Shelf and at depths of between 400–1000 m on the Exmouth Plateau have been identified as internal wave generation areas (Holloway 1996). Another study (Wolanski and Deleersnijder 1998) has identified the Scott Reef as a generation area. This reef is located on the edge of the continental shelf, some 150 km west of Prelude and rises very steeply from the sea floor on the western side. Scott Reef comprises North Reef, South Reef and Sandy Hook Inlet. North and South Reef are separated by a channel of 2-4 km width and a depth of 500 m. The reefs only emerge at low tide. Another reef, called Seringapatam Reef, is located approximately 23 km north of North Scott Reef. More information on Scott Reef can be found in chapter 7.

The data set collected by Shell Development Australia showed a large number of spike-like temperature and current speed changes that have been identified as internal solitary waves. The events happened throughout the year and a variety of waves were seen to occur. Elevation and depression waves, as well as higher mode waves were observed propagating both alone and in groups. A more detailed analysis of the dataset is discussed in chapter 6.

2.5 Conclusion and scientific scope

The Browse Basin is located in a shelf break-area, knows strong stratification in large parts of the year and there are strong semi-diurnal tidal currents. These are the three conditions required for internal wave generation and this makes the Browse Basin a likely region for significant internal solitary wave generation. Previous field studies have shown the frequent occurrence of these waves in different parts of the North West Shelf and a first analysis of the Shell field data has shown several internal wave events in the Browse Basin itself. They are a potential hazard to the FLNG facility development and further research is therefore required.

Many studies on the NWS have focused on large scale barotropic and baroclinic tidal motions and their interaction with the shelf break topography. Nonlinearity causes the internal tide to steepen and when it is steep enough, short waves are created as a result of dispersion. These waves are the study object of this thesis. The focus of this research will be on the effects of varying stratification and bathymetry on these nonlinear internal waves.

Chapter 3 – Internal solitary wave theory

3.1 Introduction

Internal waves occur in density stratified fluids and are common features in the oceans (Lamb 1998). They can occur wherever there is the right combination of stratification, bathymetry and currents. These conditions are often met in coastal regions, where internal waves are generated by flow over banks, seamounts, mid-ocean ridges and shelf breaks. Solitons are also found near fjords and in lakes (Apel 2002).

The planned FLNG facility will be located the Browse Basin, on the Australian North West Shelf break in water depths around 250m. Therefore, this chapter will focus on internal waves in the ocean, in the vicinity of shelf breaks.

Internal waves are important for a number of reasons. They can have a significant impact on offshore structures because of the vertical shear stresses accompanying the waves. This has been the reason for many studies and is the reason for this project. Furthermore, they are mainly responsible for deep ocean mixing thus creating a rich biological environment. Finally, internal waves can affect the propagation of sound in the ocean and are for that reason of potential importance for defence purposes.

Internal waves differ from surface waves in several aspects. As internal density gradients are much smaller than those at the water surface, internal wave typically have much lower frequencies and higher amplitudes than surface waves. Where surface waves can only travel horizontally, internal waves can travel horizontally along isopycnals (lines of constant density) and vertically across a density gradient.

Solitary internal waves (solitons) are a particular type of internal waves. They are non-sinusoidal, nonlinear and theoretically they preserve their height, shape and propagation due to a balance between dispersion and nonlinearity. In reality however, no exact solitons exist due to viscosity effects and other factors.

The complex generation and propagation processes of solitary internal waves require a good understanding of the physics of density-driven flows and tide-topography interaction. In this chapter, the theoretical background that is relevant for this thesis is discussed.

3.2 Stratification

Stratification is the formation of vertically varying density in the water column. Density differences can be caused by pressure, salinity and temperature differences, by suspended sediment or dissolved substances. Considering only the first three, the relationship between density ρ, temperature T, salinity S and pressure p can be written as:

$$\rho = f(T, S, p) \tag{3.1}$$

Equation (3.1) is referred to as the Equation of State.

A parameter to express the strength of stratification in a fluid is the Brunt-Väisälä frequency or buoyancy frequency N. It is the frequency of small free oscillations of water particles near the water level z and is defined by:

$$N^2(z) = -\left(\frac{g}{\rho_0}\frac{d\rho_0}{dz}\right) \quad (\text{for incompressible flow}) \tag{3.2}$$

The variation in density may be continuous or discontinuous. When a distinct interface separates two fluid layers, it can be considered as two-layer fluid (Figure 8).

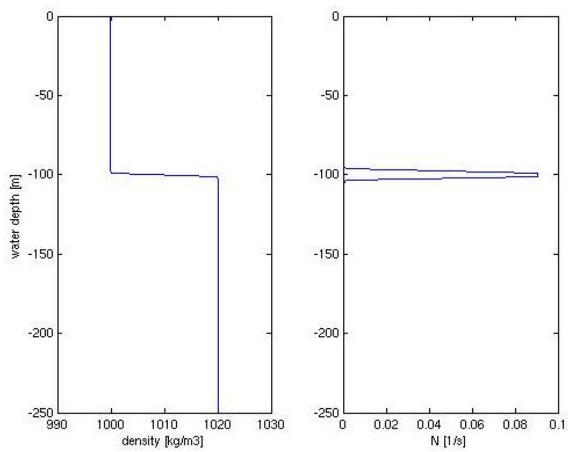

Figure 8. Two-layer density profile (left) and buoyancy frequency (right).

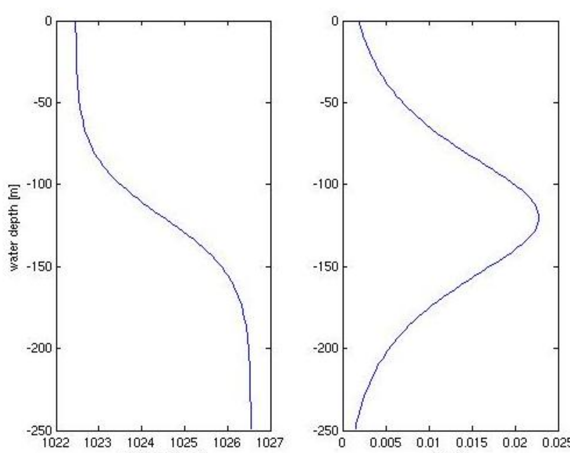

Figure 9. Density (left) and buoyancy frequency (right) profiles in the Browse Basin.

Figure 9 shows a typical density distribution in the Browse Basin at the Prelude location (left figure) and its associated buoyancy frequency (right figure). The upper water layer is usually well mixed. The water temperature in the layer near the ocean bottom is almost constant and in between is a layer in which density rapidly increases with depth due to a decrease of temperature. This is the thermocline. The depth and thickness of a thermocline in the ocean are mainly affected by seasonal weather variations, tides and currents. A stratification is stable if heavy fluid particles settle under lighter ones, so if $\frac{dp_0}{dz} < 0$. Internal waves propagate along the thermocline; the isopycnal displacements are largest where the density gradient is largest (for mode one waves).

3.3 Governing flow equations

The governing general set of equations describing internal wave dynamics consists of a momentum balance equation, a mass balance equation and a density balance equation. Assuming incompressible fluid, the equations can be written as:

$$\rho \frac{D\boldsymbol{v}}{Dt} = -\underset{\text{pressure gradient}}{\nabla p} - \underset{\text{gravity force}}{\rho g \boldsymbol{k}} - \underbrace{\rho 2\boldsymbol{\Omega} \times \boldsymbol{v}}_{\text{Coriolis force}} + \underset{\text{other forces}}{\boldsymbol{F}(\boldsymbol{v})} \tag{3.3}$$

$$\frac{\partial u}{\partial x} + \frac{\partial v}{\partial y} + \frac{\partial w}{\partial z} = 0 \tag{3.4}$$

$$\frac{D\rho}{Dt} + u\frac{\partial \rho}{\partial x} + v\frac{\partial \rho}{\partial y} + w\frac{\partial \rho}{\partial z} + w\frac{\partial \rho_0}{\partial z} = 0 \tag{3.5}$$

Depending on the stratification, this set of equations can be rewritten into a set of equations for an N-layer model (usually two-layer) or for a continuous density profile.

3.4 Generation mechanisms

About 50% of the energy in the internal wave field in the ocean is associated with tidal flow over bottom topography (the other 50% is associated with wind) (King et al. 2009). However, exact generation mechanisms are not yet fully understood and two different hypotheses have been formulated in the past (Apel 2002). They seem to depend on local conditions as evidence for both has been found in different studies.

One commonly used explanation of solitary internal wave generation over bathymetry is the lee wave mechanism (Maxworthy 1979). When a fluid particle flows over an obstacle, it will be displaced vertically. As the particle has a higher density than its surroundings, a buoyancy force will push it downwards. The particle obtains potential energy by flowing over the topography. This is converted into kinetic energy that will cause the particle to overshoot its equilibrium level and undergo a series of oscillations. If the internal flow is sub- or near critical, a series of internal lee waves form (Pietrzak et al. 1991). The condition for this is:

$$F = \frac{|U_0|}{|c_r|_{\lambda\to\infty}} \leq 1 \tag{3.6}$$

Where U_0 is the mean horizontal velocity of the background flow and c_r is the phase velocity relative to the flowing fluid in the long wave limit.

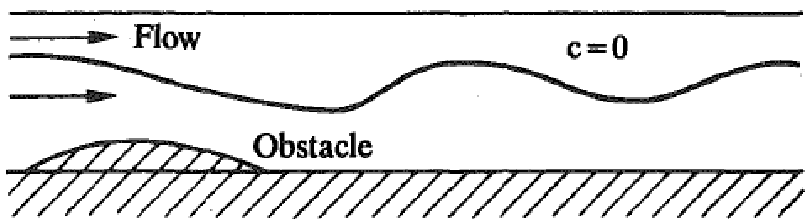

Figure 10. Lee waves downstream obstacle. Source: Pietrzak, Kranenburg et al. (1991)

It is assumed that the obstacle occupies an interval given by $-l \leq x \leq l$. The linear solution for the lee wave represents a simple harmonic wave. For a two-layer fluid it is given by equation (27) in Kranenburg and Pietrzak (1990):

$$\eta = \frac{F_2^2}{kbH}\int_{-l}^{l} h_b(\xi)\sin k\frac{\xi - x}{H}\,d\xi, \tag{3.7}$$

where η the height of the interface, k a dimensionless wave number, H the total water depth, ξ a dummy variable, z the horizontal distance and h_b the height of the obstacle. F_2 is the internal Froude number and can be written as:

$$F_2^2 = S_2\frac{u_2^2}{g'h_2} \tag{3.8}$$

With S a profile coefficient assumed constant:

$$S_2 = \frac{\langle u^2\rangle_2}{u_2^2} \tag{3.9}$$

The expression for b is:

$$b = \frac{u_1^2 h_1 + u_2^2 h_2}{3g' h^2} \tag{3.10}$$

Where g’ is the reduced gravitational acceleration $g\Delta\rho/\rho_0$, u_1 and u_2 the flow velocities in the upper and lower layer and h_1 and h_2 the thickness of the upper and lower layer respectively.

For a cosine-shaped obstacle, the height can be expressed as:

$$h_b = h_b \cos\frac{\pi}{2}\frac{x}{l} \qquad for -l \le x \le l \tag{3.11}$$

Substituting this in equation (3.7) then gives the following equation for the lee wave amplitude and phase at the centre of the obstacle:

$$\eta = \frac{\pi}{b}\frac{F_2^2}{k^2}\cdot\frac{k\frac{l}{H}\cos k\frac{l}{H}}{\left(k\frac{l}{H}\right)^2 - \frac{\pi^2}{4}}\cdot h_b \sin k\frac{x}{H} \tag{3.12}$$

Evidence for this generation mechanism exists from the Knight Inlet in Canada (Farmer and Armi 1999).

Lee waves that originate at the time of peak off-shelf tidal flow propagate on-shelf. However, off-shelf propagating waves have also been observed during off-shelf tidal flow. In this case, the lee wave mechanism can no longer explain the origin of the waves (Jeans and Sherwin 2001).

Other studies on soliton generation suggest that the operative process is tide-topography interaction (Holloway and Chatwin 2000);(Jeans and Sherwin 2001). The tidal motion over a ridge or slope in a stratified ocean continually disturbs the thermocline. Waves are created at the tidal frequency. This is the internal tide or baroclinic tide. The linear internal tide propagates shoreward over the sloping bottom of the continental shelf. Non-linear steepening of the baroclinic tide causes an internal tidal bore. This generates a packet of solitons with the largest waves travelling at the front of the group, and the smallest waves at the rear.

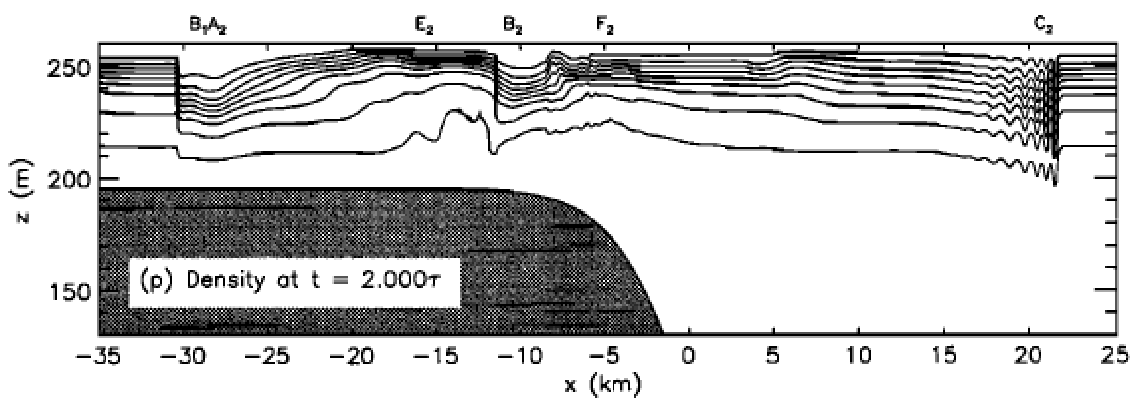

Figure 11. Soliton generation at a shelf break. From (Lamb 1994).

Holloway has extensively studied this generation mechanism on the North West Australian Shelf through numerical model simulations and field studies (Holloway 1994; Holloway 1996).

Both generation mechanisms have been extensively studied through laboratory tests and numerical simulations, mostly for two-layer flow. For example, Horn et al. (1998) did a series of laboratory tests to study the generation, propagation and degeneration of internal waves in lakes.

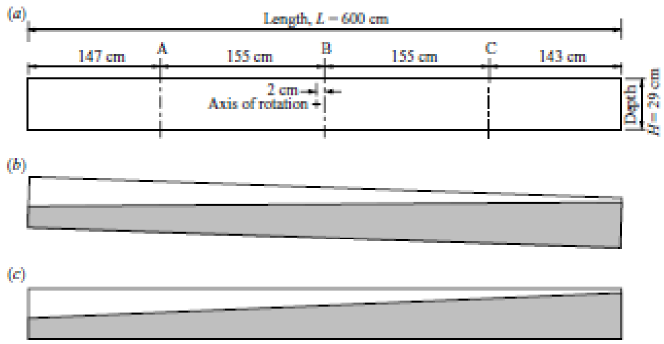

Figure 12. Laboratory set up. Reproduced from Horn et al. (1998).

In lakes, wind blows warm surface water to the downwind end of a lake. This results in a tilted thermocline. When the wind dies, the thermocline is released, creating a nonlinear basin-scale wave that steepens until dispersion results in internal solitary waves. This nonlinear and dispersive process is the same for internal tides.

The laboratory experiments by Horn et al. (1998) were carried out in a tank with two layer stratification. An initial baroclinic pressure gradient was created by tilting the tank to a small angle. This caused the lower layer to flow towards the downwelled end and the upper layer into the opposite direction towards the upwelled end. The initial wave steepened into an internal surge. This surge evolved into a packet of solitary waves.

The goal of the study was to examine the degeneration of large-scale internal waves in lakes and the transfer of energy from the basin-scale to much smaller scales. By varying the initial angle of tilt and the interface depth, different degeneration mechanisms were simulated. For small angles of tilt, the nonlinear steepening was weak and the motion was dampened by viscous effects. By increasing the angle of tilt and therefore the nonlinearity of the initial wave, the basin-scale wave was observed to steepen and evolve into a packet of solitons. In some experiments with very large tilts, an undular bore was observed, accompanied with local shear instabilities and turbulence.

In some areas, the generation mechanism is very clear because there is a very pronounced, isolated bottom obstacle. In other areas the bathymetry is more complex. There can be several soliton generation sites and solitons propagating away might be transformed by interaction with sea floor topography further away from the shelf break. For example, the interaction of a soliton with a sill can generate a higher mode solitary wave. When a soliton-type disturbance encounters a bottom obstacle, the wave splits into pairs of reflected and transmitted waves of first and second mode (Vlasenko and Hutter 2001).

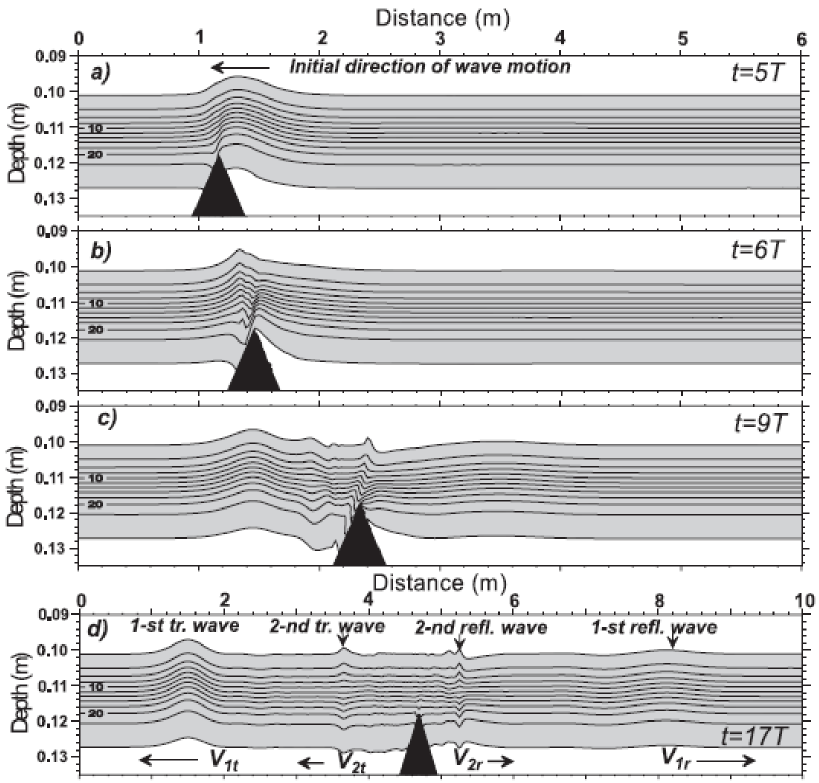

Figure 13. Generation of second mode waves. Reproduced from Vlasenko and Hutter (2001).

The likely generation mechanism of internal waves in the Browse Basin will be discussed in chapter 5 after analysis of the field data.

The laboratory tests by Kranenburg and Pietrzak (1990) and Horn et al. (1998) will be simulated with Finlab and the numerical results will be compared to the laboratory test results. The reason for this is twofold: to validate Finlab for two non-hydrostatic internal flow cases, namely internal lee waves and internal solitary waves and to gain a better understanding of the different degeneration mechanisms of solitary internal waves. The validation results can be found in chapter 5.

3.5 Linear flow theory

The laboratory tests described above are for two-layer flow systems. In the Browse Basin however, the stratification is continuous. As both systems will be simulated numerically, linear flow theory for two-layer stratification and for continuous stratification will be treated in this section. Nonlinear wave theory will be treated in section 3.6.

3.5.1 Two-layer stratification

In the case of a two-layer system, assuming hydrostatic flow and neglecting the Coriolis terms, the continuity and momentum equations for each layer become:

$$\frac{\partial h_1}{\partial t} + \frac{\partial}{\partial x} h_1 u_1 = 0 \tag{3.13}$$

$$\frac{\partial h_2}{\partial t} + \frac{\partial}{\partial x} h_2 u_2 = 0 \tag{3.14}$$

$$\frac{\partial h_1}{\partial t} + u_1 \frac{\partial u_1}{\partial x} + g \frac{\partial}{\partial x}(h_b + h_1 + h_2) = -\frac{s_0 - s_1}{\rho_1 h_1} \tag{3.15}$$

$$\frac{\partial h_2}{\partial t} + u_2 \frac{\partial u_2}{\partial x} + g \frac{\partial}{\partial x}(h_b + h_2) = -\frac{s_1 - s_2}{\rho_2 h_2} \tag{3.16}$$

where u_1 and u_2 are the vertically averaged velocities in the upper and lower water layer. The velocity at the bottom is assumed to be zero, and s_n is the shear stress for layer n, defined as:

$$s_n = -k_n \rho_n \left| u_n - u_{n+1} \right| (u_n - u_{n+1}) \tag{3.17}$$

Therefore s_0 is the wind stress, and s_1 is the interfacial stress, and s_2 is zero. In this equation, k is a coefficient that must be determined experimentally but k_0 and k_1 typically have values between $8x10^{-4}$ to $25x10^{-4}$ and $4x10^{-4}$ to $15x10^{-4}$ respectively.

In the presence of an interface or a free surface, non-stationary flow generally has a wave character. As a consequence of the hydrostatic approximation, the layer model is only valid for long waves. Assuming the density differences between the layers are small, two types of waves can be discerned: external waves, travelling on the water-air interface, and internal waves, propagating on the interface between water layers with different densities.

Equations (3.13)-(3.16) form a set of partial differential equations. The method of characteristics can be used to derive equations for the propagation speeds of the internal (c_i) and external (c_e) waves:

$$c_i = \frac{h_1 u_2 + h_2 u_1}{H} \pm \sqrt{\frac{h_1 h_2}{H^2}\left[\varepsilon g H - (u_1 - u_2)^2 \right]} \tag{3.18}$$

$$c_e = \frac{h_1 u_1 + h_2 u_2}{H} \pm \sqrt{gH} \tag{3.19}$$

Where the total water depth $H = h_1 + h_2$ and the relative density difference $\varepsilon = (\rho_2 - \rho_1) / \rho_2$.

The external waves propagate with a wave speed that is in the same order as the wave speeds for one layer flow. Due to the reduced gravity effect, the propagation speed of the internal waves is much lower.

3.5.2 Continuous stratification

The stratification in the Browse Basin cannot be approximated as a two-layer system as density gradients there are continuous. As mentioned before, continuous stratification means that the fluid has a vertical density variation and therefore waves can travel in both the horizontal and vertical directions. However, in the presence of bottom and surface boundaries horizontally propagating modal waves exist.

The momentum balance equation (3.3) can be linearized (non-linear terms are neglected) using the Boussinesq approximation and the f-plane approximation, with:

$$f = 2\Omega \sin\varphi \tag{3.20}$$

with Ω the angular velocity and φ the latitude. This gives:

$$\frac{\partial u}{\partial t} - fv = -\frac{1}{\rho_0}\frac{\partial p}{\partial x} \tag{3.21}$$

$$\frac{\partial v}{\partial t} + fu = -\frac{1}{\rho_0}\frac{\partial p}{\partial y} \tag{3.22}$$

$$\frac{\partial w}{\partial t} = -\frac{1}{\rho_0}\frac{\partial p}{\partial z} - g\frac{\rho}{\rho_0} \tag{3.23}$$

The density conservation equation (3.5) can also be linearized and becomes:

$$\frac{\partial \rho}{\partial t} + w\frac{\partial \rho_0}{\partial z} = \frac{\partial g'}{\partial t} - N^2 w = 0 \tag{3.24}$$

By cross-derivating these expressions a single equation for the vertical velocity w in an internal wave can be derived. This gives:

$$\frac{\partial^2}{\partial t^2}\nabla^2 w + f^2\frac{\partial^2 w}{\partial z^2} + N^2(z)\nabla^2{}_h w = 0 \tag{3.25}$$

Where ∇^2 is the three-dimensional and $\nabla^2{}_h$ the horizontal Laplacian. Solutions in the (x,z)-plane are sought of the form:

$$w = W(z)e^{i(kx-\omega t)} \tag{3.26}$$

Substitution of (3.26) into (3.25) gives:

$$\frac{\partial^2 W}{\partial z^2} + k^2\frac{N^2(z) - \omega^2}{\omega^2 - f^2}W = 0 \tag{3.27}$$

This is called the Taylor-Goldstein equation. An expression is introduced for convenience:

$$m^2(z) = k^2 \frac{N^2(z) - \omega^2}{\omega^2 - f^2} \tag{3.28}$$

Boundary conditions are posed on the bottom and the water surface:

W = 0 at *z*=0, *z*=-*H*, with H the water depth.

When *N (z)* is constant, the general solution is:

$$W = C_1 \sin(mz) + C_2 \cos(mz), \tag{3.29}$$

The boundary conditions can be gathered in a matrix:

$$\begin{pmatrix} 0 & 1 \\ -\sin mH & \cos mH \end{pmatrix} \begin{pmatrix} C_1 \\ C_2 \end{pmatrix} = \begin{pmatrix} 0 \\ 0 \end{pmatrix} \tag{3.30}$$

To have non-trivial solutions for C_1 and C_2, the determinant of the matrix must be zero. This gives for *m*:

$$m_n = \frac{n\pi}{H} \tag{3.31}$$

This leads to the internal wave dispersion relation:

$$k_n = \pm \frac{n\pi}{H} \left(\frac{\omega^2 - f^2}{N^2 - \omega^2} \right)^{1/2} \tag{3.32}$$

These equations shows that if $k \to 0$ (long wave limit), the wave frequency ω approaches f. If $k \to \infty$ (short wave limit), ω approaches N.

The wave frequency can be expressed as a function of *k* and *n*:

$$\omega^2 = \frac{N^2 k^2 + f^2 \left(\frac{n\pi}{H} \right)^2}{k^2 + \left(\frac{n\pi}{H} \right)^2} \tag{3.33}$$

Differentiating the expression for the wave frequency to *k* gives the horizontal group velocity:

$$c_g = \frac{\partial \omega}{\partial k} = \pm \left(\frac{H}{n\pi} \right) \frac{\left(\omega^2 - f^2 \right)^{1/2} \left(N^2 - \omega^2 \right)^{3/2}}{\omega \left(N^2 - f^2 \right)} \tag{3.34}$$

The horizontal wave speed is given by:

$$c = \frac{\omega}{k} = \pm\left(\frac{H\omega}{n\pi}\right)\frac{\left(N^2-\omega^2\right)^{1/2}}{\left(\omega^2-f^2\right)} \tag{3.35}$$

Equations (3.34) and (3.35) show that higher modes propagate more slowly. Furthermore, the wave speed varies with *k*, which means that internal waves are dispersive. Waves of the same mode but with different wave numbers have different phase and group speeds and cannot therefore propagate as a coherent group.

An infinite number of vertical wave modes is allowed in a continuously stratified fluid (Pietrzak et al. 1991). For uniform stratification, the vertical modes become:

$$W_n = \sin\left(\frac{n\pi z}{H}\right) for\, n = 1,2,3\ldots \tag{3.36}$$

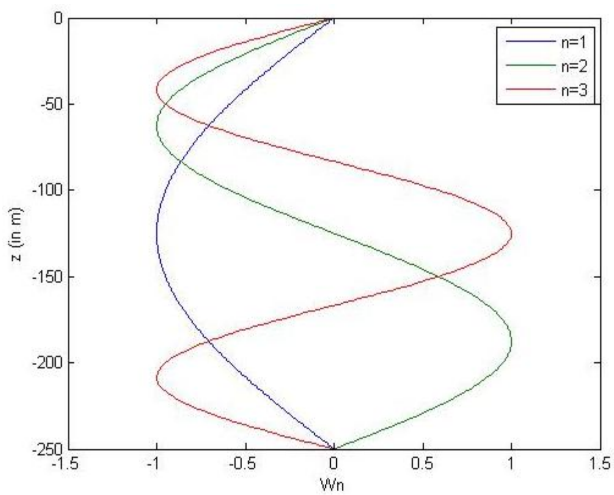

Figure 14. First three vertical modes for a water column of 250 m.

The general solutions for the vertical velocity *w* and the horizontal velocity *u* are a superposition of eigenfunctions:

$$w = \sum_n a_n W_n \cos(k_n x - \omega t) \tag{3.37}$$

$$u = -\sum_n a_n \frac{n\pi}{k_n H}\cos(\frac{n\pi z}{H})\sin(k_n x - \omega t) \tag{3.38}$$

Where a_n is a constant to be determined.

3.6 Non-linear waves

3.6.1 Solitons

So far, only linear flow theory has been considered. This is a valid approximation when small amplitude internal waves are considered. However, the amplitudes of the internal waves in the Browse Basin are very large (30-50 m in 250 m water depth). To correctly model these waves, non-linear effects must be taken into account.

Another criterion for the applicability of linear equations is the Froude number (Gerkema and Zimmerman 2008):

$$Fr = \frac{U}{NH} << 1 \tag{3.39}$$

Where *U* is the fluid velocity and *NH* is approximately the horizontal wave speed. This criterion can be interpreted as the restriction that fluid velocities must be much smaller than the wave speed. Thus, the linear approach is only justified if the Froude number is much less then unity. Wave speeds of the solitons in the Browse Basin are unknown, but values found in literature (Internal wave atlas) indicate that values of 0.5-0.7 m/s are not uncommon for solitons. This results in Froude numbers that are not low enough to justify the linear approach.

A possible effect of non-linearity is wave steepening and eventually wave breaking (Gerkema and Zimmerman 2008). In section 3.5.2 it was shown that internal waves are dispersive. Under certain conditions, non-linear steepening can be balanced by dispersion. This yields a wave of constant shape called internal solitary wave, or soliton.

3.6.2 Korteweg-de Vries equation

Solitons owe their existence to a balance between non-linearity and dispersion. Non-linearity alone would make the wave steepen and break. Dispersion alone would make the wave break up into its Fourier components.

An equation that has soliton solutions is the Korteweg-de Vries (KdV) equation. It was derived at the end of the 19th century and is one of the most well-known non-linear wave equations. The one-dimensional KdV equation can be written as:

$$\frac{\partial \eta}{\partial t} + c_0 \left(\frac{\partial \eta}{\partial x} + \alpha \eta \frac{\partial \eta}{\partial x} + \gamma \frac{\partial^3 \eta}{\partial x^3} \right) = 0 \tag{3.40}$$

In this equation, η is the displacement of the interface, c_0 the linear long wave speed for internal waves, α is a nonlinear coefficient and γ is a dispersion coefficient.

For a two layer system, c_0 and the coefficients α and γ in equation (3.40) are:

$$c_0 = \sqrt{g \frac{\Delta\rho}{\rho_2} \frac{h_1 h_2}{h_1 + h_2}} \qquad \alpha = \frac{3}{2} \frac{h_1 - h_2}{h_1 h_2} \qquad \gamma = \frac{1}{6} h_1 h_2 \tag{3.41}$$

For continuously stratified fluids, the coefficients are more complicated integral expressions. Several versions of these expressions can be found in the literature, but differ quite significantly from each other (Apel 2002).

A shape preserving soliton solution to the two-layer KdV equation is:

$$\eta = a \ \mathrm{sech}^2 \left(\frac{x - ct}{\lambda} \right) \tag{3.42}$$

where a is the wave amplitude, c the propagation speed and λ the wave length.

These parameters are given by:

$$c = c_0 \left[1 + \frac{1}{2} a \frac{h_1 - h_2}{h_1 h_2} \right], \qquad \lambda = \frac{2 h_1 h_2}{\left[3a(h_1 - h_2) \right]^{1/2}} \tag{3.43}$$

Figure 15 shows two soliton solutions for different wave amplitudes.

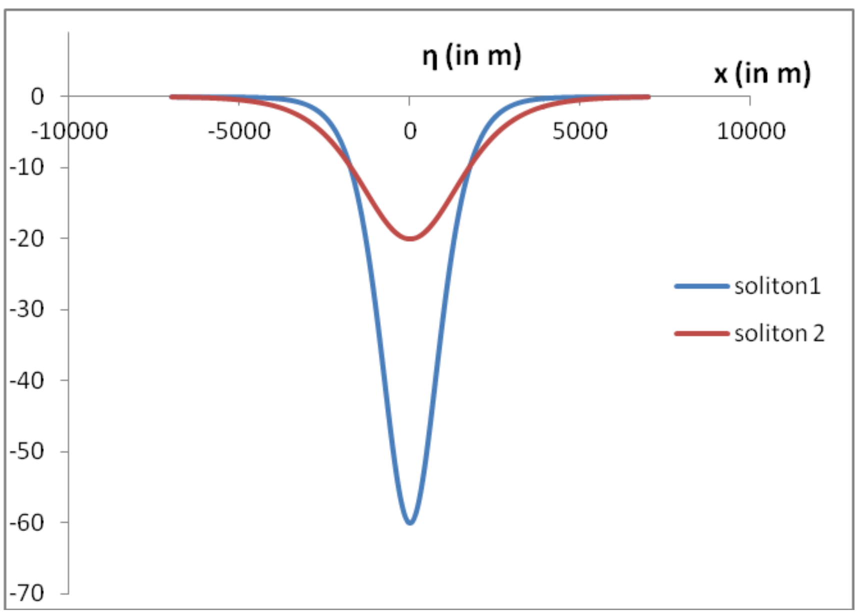

Figure 15. Two soliton solutions with different amplitudes.

The non-linearity of the waves is evident in the expression for the wave speed, because it depends on the wave amplitude. Additionally, it follows from the expression for l that:

$$a(h_1 - h_2) > 0 \tag{3.44}$$

In the ocean, in general h1 < h_2. Therefore the wave amplitude must be negative and the soliton is a wave of depression. This can be applied to the field data to gain a better understanding of when waves of depression or elevation can be expected. Figure 15 shows that solitons with large amplitudes are shorter than solitons with lower amplitudes. The expression for the wave speed c in (3.41) further shows that if the upper layer is thinner than the lower layer and as a result the amplitude is negative, it follows that solitons with larger amplitudes propagate faster than smaller ones. This results in the rank-ordered wave trains with the largest amplitudes waves leading the group. Also, the phase speed of the soliton (c) will exceed the linear long-wave phase speed (c_0).

3.7 Conclusions

Internal waves occur in oceans with the right combination of bathymetry, stratification and currents. Their appearance varies from large scale baroclinic motions such as those associated with the internal tides to short nonlinear solitary waves. The development and propagation of solitons can be mathematically described by the first-order nonlinear model advanced by Korteweg and De Vries. The vertical structure is described with the Taylor-Goldstein equation.

Solitary waves can be generated through a lee wave mechanism or tide-topography interaction. Previous laboratory studies have increased the knowledge about the exact generation mechanisms. These were usually tests with two-layer flow. Numerical models were used to study the interaction between the baroclinic tide and bathymetry. They are models suitable for large-scale motions. They make use of the hydrostatic approximation and are for that reason not suitable for simulations of the solitons propagating onto the shelf in shallower water.

In the next chapter, a numerical model will be introduced that could be suitable. Finlab is a non-hydrostatic flow model designed for flow problems with complex topography. It will be tested and applied to simulate internal waves on the shelf break in the Browse Basin.

Chapter 4 – Model description

4.1 Introduction

The conclusions in chapter 3 showed that a number of aspects of internal waves are critical when attempting to numerically model them.

First, the non-hydrostatic characteristics of solitary internal waves must be taken into account. The hydrostatic approximation is only valid for waves that are very long compared to the water depth. The ratio of the amplitude of the internal tide to ocean depth of the ocean is usually small enough to make the hydrostatic approximation. However, nonlinearity causes the tide to steepen and energy is transferred to smaller length scales. Therefore a non-hydrostatic model is needed to simulate the smaller-scale waves that are generated at the front of the tidal wave.

Chapter 3 further highlighted the strong interaction between currents and sea floor topography. Irregular bathymetry will lead to complicated meshes and a numerical model must be adapted to solve the full flow equations on those meshes.

Finlab is a fully 3-dimensional, non-hydrostatic flow model. It is based on the incompressible Navier-Stokes equations and uses the finite element method. It was developed at Svasek and Delft University of Technology by Robert Jan Labeur. The model works with fully unstructured grids with moving free surfaces. The model was developed for a wide range of hydraulic engineering problems involving complex, small-scale geometries.

Finlab thus meets the requirements for modelling internal waves. However, it has never been extensively tested for internal flow situations. Validation tests will be performed to see if Finlab has the capability to simulate solitary internal waves in the Browse Basin.

In this chapter, a short description of Finlab is given. A more detailed description can be found in (Labeur 2009). In the next chapter, the results of the validation tests will be discussed.

4.2 Governing equations

As mentioned in the introduction, Finlab is based on the incompressible Navier-Stokes equations. In vector form, the momentum equation is:

$$\frac{\partial(\rho \boldsymbol{u})}{\partial t} + \nabla \cdot (\rho \boldsymbol{u} \otimes \boldsymbol{u}) + \nabla p - \nabla \cdot \left(2\mu \nabla^{s} \mathbf{u}\right) = \mathbf{F} \tag{4.1}$$

With $\mathbf{F}$ the external forces in N/m^3, $\boldsymbol{u}$ the velocity vector in m/s, p the fluid pressure in N/m^2, t the time in s, ρ the fluid density kg/m^3 and μ the fluid viscosity in kg/ms. $\mathbf{F}$ includes amongst others the buoyant forcing term, Δρ' g/ρ. The second term on the left hand side of equation (4.1) is the advective term, with $(\boldsymbol{u}\otimes\boldsymbol{u})_{ij} = u_i u_j$. The diffusive part is the last term on the left hand side, with ∇^s the symmetric gradient operator, $\nabla^s = \frac{1}{2}\nabla(\cdot) + \frac{1}{2}\nabla(\cdot)^T$. The continuity equation can be written as:

$$\nabla \cdot \boldsymbol{u} = 0 \tag{4.2}$$

The model also takes transport of mass into account. For a relative density difference $\tilde{\rho}$:

$$\tilde{\rho} = \frac{(\rho - \rho_0)}{\rho_0} \tag{4.3}$$

The transport equation is:

$$\frac{\partial \tilde{\rho}}{\partial t} + \boldsymbol{u} \cdot \nabla \tilde{\rho} - \nabla \cdot (\kappa \nabla \tilde{\rho}) = f \tag{4.4}$$

Where κ is the turbulent diffusivity and f the source term.

4.3 Mesh partitioning and discretization

A numerical model can only solve the continuous problem given by equations (4.1), (4.2) and (4.4) if it is discretized into an algebraic system of equations. Finlab uses the finite element method for the discretization.

First, the solution region is divided into a number of small regions called elements. Each element is formed by the connection of a certain number of nodes, in this case three. An advantage of the finite element method is the flexibility and freedom in mesh partitioning. The elements are unstructured and so the discretization can be refined in sub-regions. This allows the total number of elements to remain low while the results stay accurate. An example of an unstructured mesh is shown in Figure 16.

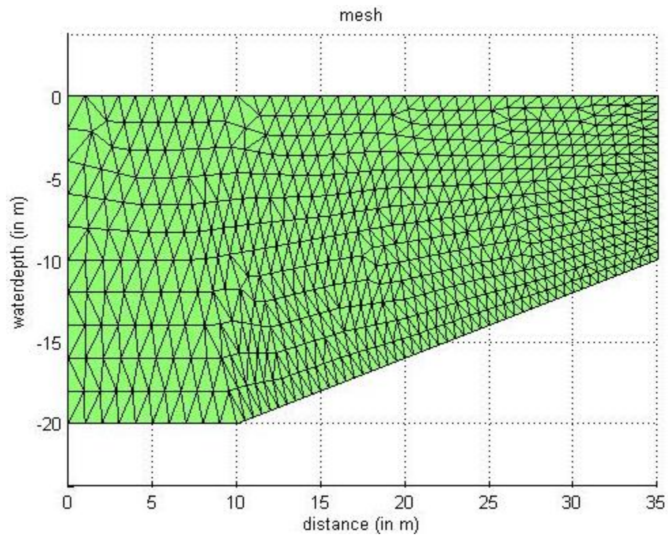

Figure 16. Example of mesh with triangular grid elements.

After the mesh partitioning, the solution is approximated in each element by a polynomial function. These functions represent the nature of the solution within each element and are called basis functions (Lewis et al. 2004). Substitution into the continuous equations directly yields analytical solutions from which the evolution of the flow field is evaluated.

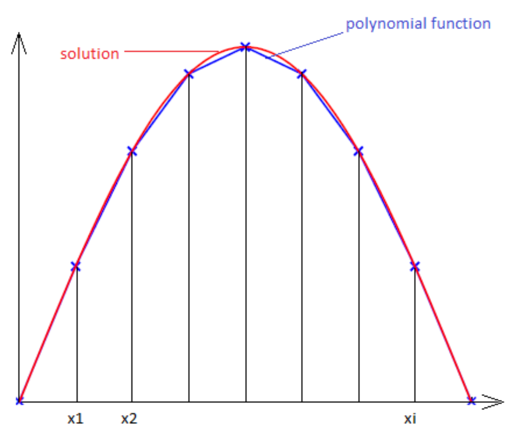

Figure 17. Finite element method.

4.4 Time integration method

Flow problem solutions will usually evolve in time. The time interval is partitioned into discrete time levels t_0, t_1, t_n with interval size Δt. The solution at time t_n is calculated from the previous time level. Time integration schemes implemented in Finlab are the Θ-scheme and the Fractional Step scheme. For Θ=0 (Euler Forward scheme) and Θ=1 (Euler Backward scheme), the solution will be first-order accurate. For Θ=0.5 (Crank-Nicolson scheme), the solution is second order accurate but the method will be weakly stable only. The Fractional Step scheme is both second-order accurate and strongly stable. It splits every time step in three sub-steps: $t_n \to t_{n+\alpha} \to t_{n+1-\alpha} \to t_{n+1}$. In the first and last step, the one step Θ-scheme with parameter Θ is applied and in the second step parameter 1- Θ is applied (Labeur 2009).

The Euler Backward scheme is very suitable for steady state flows as its strong damping characteristics accelerate convergence. However in this project we consider tidal currents in the Browse Basin, which are strongly time dependant.

The Crank-Nicolson scheme has theoretically no amplitude damping. The Fractional Step scheme on the other hand does have some amplitude damping due to its smoothing properties.

Therefore, the Crank-Nicolson time integration scheme will be used for the model validation as it has no damping properties and is second-order accurate.

4.5 Turbulence closure models

Ocean flows are turbulent and therefore turbulence modelling must be considered in this project. The Navier-Stokes equations can be solved to the smallest turbulence scale where dissipation occurs (called the Kolmogorov scale). However, this is time-consuming and requires much computation power, which also makes it expensive. Therefore, a turbulent model is used that makes some simplifications of the flow features on the smallest scales. Each variable in the equations is split in a mean and a fluctuating part. For the velocity term for example:

$$u = \overline{u} + u' \tag{4.5}$$

Substituting the mean and fluctuating terms into the momentum equation and averaging gives:

$$\frac{\partial \overline{u}}{\partial t} + \frac{\partial \overline{u}\overline{u}}{\partial x} + \frac{\partial \overline{u}\overline{v}}{\partial y} + \frac{\partial \overline{u}\overline{w}}{\partial z} + \frac{1}{\rho}\frac{\partial \overline{p}}{\partial x} - f\overline{v} - \upsilon \Delta u + \left[\frac{\partial \overline{u'u'}}{\partial x} + \frac{\partial \overline{v'u'}}{\partial y} + \frac{\partial \overline{w'u'}}{\partial z} \right] = 0 \tag{4.6}$$

$$\frac{\partial \overline{v}}{\partial t} + \frac{\partial \overline{v}\overline{u}}{\partial x} + \frac{\partial \overline{v}\overline{v}}{\partial y} + \frac{\partial \overline{v}\overline{w}}{\partial z} + \frac{1}{\rho}\frac{\partial \overline{p}}{\partial y} + f\overline{u} - \upsilon \Delta v + \left[\frac{\partial \overline{u'v'}}{\partial x} + \frac{\partial \overline{v'v'}}{\partial y} + \frac{\partial \overline{w'v'}}{\partial z} \right] = 0 \tag{4.7}$$

$$\frac{\partial \overline{w}}{\partial t} + \frac{\partial \overline{u}\overline{w}}{\partial x} + \frac{\partial \overline{v}\overline{w}}{\partial y} + \frac{\partial \overline{w}\overline{w}}{\partial z} + \frac{1}{\rho}\frac{\partial \overline{p}}{\partial z} + g - \upsilon \Delta w + \left[\frac{\partial \overline{u'w'}}{\partial x} + \frac{\partial \overline{v'w'}}{\partial y} + \frac{\partial \overline{w'w'}}{\partial z} \right] = 0 \tag{4.8}$$

These are the Reynolds averaged Navier-Stokes equations. The extra terms between brackets are the Reynolds stresses. They are generally non-zero in turbulent flows. A turbulence closure model can now be used. In Finlab, the Reynolds stresses can be solved using the k-epsilon, Large Eddy Simulation or mixing length turbulence models (Labeur 2009).

It can be assumed that the Kolomogorov scales are determined by the viscosity (υ_t) and the dissipation (ε) as kinetic energy is destroyed by viscous forces (Davidson 2011). The mixing length model and k-epsilon model are based on the Boussinesq assumption that relates the Reynolds stresses to the velocity gradients and the turbulent viscosity (Uijttewaal 2010) .

The mixing length model uses the following expression for the turbulent viscosity υ_t :

$$\upsilon_t = l_{mix}^2 \cdot \left| \frac{\partial U}{\partial z} \right| \tag{4.9}$$

The mixing length l_{mix} can be described directly. However, it is often not known in advance and must be determined.

The Large Eddy Simulation (LES) method computes the mixing length from the grid element width h_e using:

$$l_{mix} = C_s h_e \tag{4.10}$$

C_s is Smagorinsky's constant. It can range from 0.05 to 0.20 (Labeur 2009).

The k-epsilon model determines the kinetic energy k and turbulence dissipation rate ε with two transport equations. They are related to the turbulent viscosity according to:

$$\upsilon_t = c_\mu \frac{k^2}{\varepsilon} \tag{4.11}$$

with c_μ a constant. The mixing length model is unsuitable for complex flows because it is very difficult to estimate the distribution of the mixing length. It will therefore not be used for the simulation of internal waves. The k-epsilon model makes assumptions for all the turbulence scales while the LES method only models the smallest scales and resolves all the larger scale motions. However, the k-epsilon is widely used, easy to implement and computationally cheap. Simulations with the k-epsilon model and LES model will be run to determine which method performs better for this particular flow problem.

4.6 Boundary conditions

To solve the flow equations, boundary conditions are required at all the boundaries of the flow domain.

In- and outflow boundaries

At inflow boundaries a flow velocity can be imposed. The velocity profile can be uniform or vary in the vertical direction. In the case of two-layer flow, two inflow boundaries can be defined that each have a different flow velocity specified. Velocities can be constant or change in time (for example sinusoidal to simulate tidal flow). At the outflow boundary, a water level can be imposed.

Closed boundaries

A closed boundary implies that no water flows across the boundary. It can be further specified as:

- No slip: there is no flow along the boundary.
- Partial slip: slip depends on shear stress at the wall (Hanif 2004).

- Free slip*:* there can be flow along the boundary but not perpendicular or normal to it.

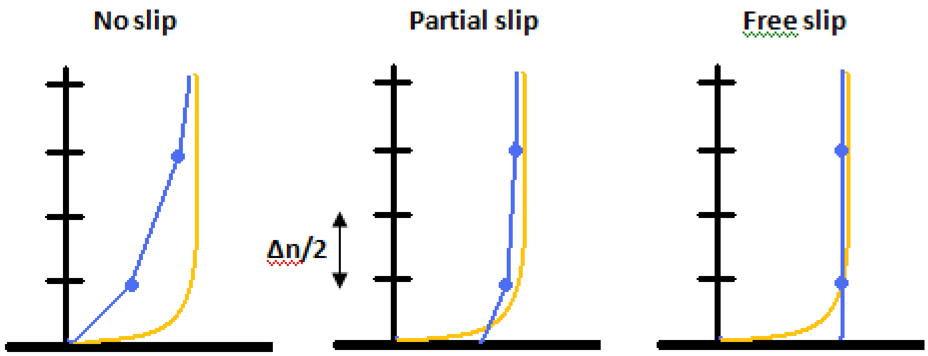

Figure 18. Solid boundary conditions.

Closed boundaries in Finlab can be partial slip (called 'wall') or free slip (called 'symm') conditions. Partial slip conditions will be used as this is physically more realistic.

Surface boundary

The water surface boundary can be defined as a free surface boundary or a rigid lid boundary. In the case of a free surface boundary the computational grid is continuously changing and adapts itself to the position of the free surface (Labeur and Pietrzak 2004). The rigid lid approach means that the upper boundary is at z=o.

4.7 Initial conditions

As initial condition a density field is given in the entire computational domain. The density can vary in both the horizontal and vertical direction and may be discontinuous or continuous. The density distribution is implemented in Finlab by means of a relative density transport variable R_0 that represents the relative density difference in the flow domain (equation 4.3) and a concentration value that can vary in the horizontal and vertical directions and multiplied with R_0, gives the relative concentration everywhere in the domain. For example, a two-layer system with a density difference of 20 kg/m^3 will be represented by R_0=0.02, a concentration value of 0 in the upper layer and 1 in the lower layer.

The initial velocity is zero everywhere in the computational domain.

4.8 Output

The output of the model has the form of a matrix with values of the flow velocities in three directions, the density and the x- and y-coordinates for each grid point and after each time step. This output data can be analyzed and visualized with the computing software program Matlab.

Chapter 5 - Model validation

5.1 Introduction

The numerical model Finlab (and its precursor FINEL) has been tested for linear internal wave theory and for an internal lee wave test. In this chapter, the capabilities and limitations of the model regarding internal flow are further tested by validating the model against two laboratory test cases described in literature (see section 3.4).

The first test case is based on the tilted tank experiment done by Horn et al. (2001). A series of laboratory experiments were undertaken to study the generation mechanisms of internal waves in lakes. This is a relevant validation test for this project, because the nonlinear/dispersive evolution of a seiche in a lake and of an internal tide in the ocean is the same process. As mentioned in section 3.1, the nonlinear steepening of an internal tide can generate solitary waves in the ocean. In a similar way, solitary waves can be generated from the steepening of a surge in a lake where a wind stress has tilted the interface in a stratified basin.

The second validation test case is the lee wave experiment described by Kranenburg and Pietrzak (1990), also mentioned in section 3.4. They compared a mathematical model and laboratory experiments that deal with lee wave generation by two-layer flow over small-scale bottom topography. This is another common internal wave generation mechanism that is relevant for the solitary wave project.

The model validation will help to define the best numerical set up and to assess the reliability and accuracy of simulations in the next phase of the project. The laboratory tests studied the different soliton generation mechanisms and will for that reason also help understand how solitons are generated and how they propagate.

In the following paragraphs, a short description of the laboratory set up is given, followed by a description of the numerical set up, the numerical sensitivity analysis and flow behaviour tests.

5.2 Tilted tank test case

Horn et al. (1998 and 2001) did a series of laboratory tests to study the generation, propagation and degeneration of internal waves in closed basins. Their experiments were carried out in a fully enclosed clear acrylic tank 600 cm long, 29 cm deep and 30 cm wide.

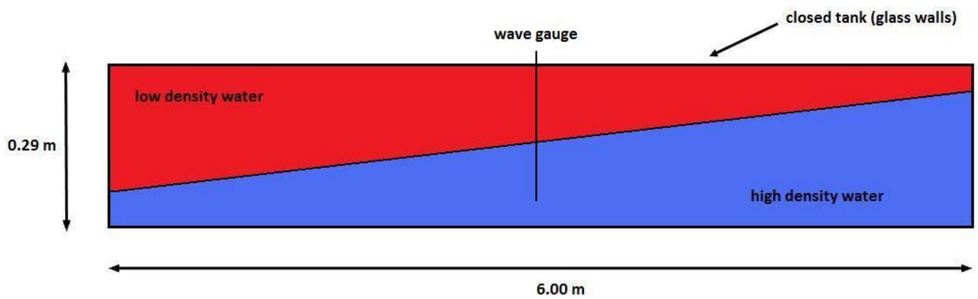

Figure 19. Schematic diagram of the experimental set up.

The tank could rotate around its centre. A two-layer stratification was established by tilting the tank through an angle of 23^0 and partly filling it with fresh water. Salt water was then slowly inserted into the bottom of the tilted tank. After filling, the tank was slowly lowered to its horizontal position. The overall density difference between the upper and lower layer was kept constant at $\Delta\rho$=20 kg/m^3. The maximum initial interface thickness was 1 cm. To commence the experiment, the tank was slowly rotated to the required angle of tilt θ and quickly returned to a horizontal position. The evolving wave field and the interface displacements were recorded by three wave gauges in the tank.

When the initially tilted tank was returned to the horizontal position, the baroclinic pressure gradient caused the lower layer to flow towards the downwelled end and the upper layer into the opposite direction towards the upwelled end. The initial wave steepened into an internal surge. This surge evolved into a packet of internal solitary waves. Figure 20 shows the steepening of an initial basin-scale wave and the generation of a packet of solitary waves for one particular test case with $h_2/H = 0.3$, $\theta=1.5^0$, $\eta_0/h_2=0.9$ where h_1 and h_2 are respectively the upper and lower layer thicknesses and η_0 is the initial interface displacement above h_2.

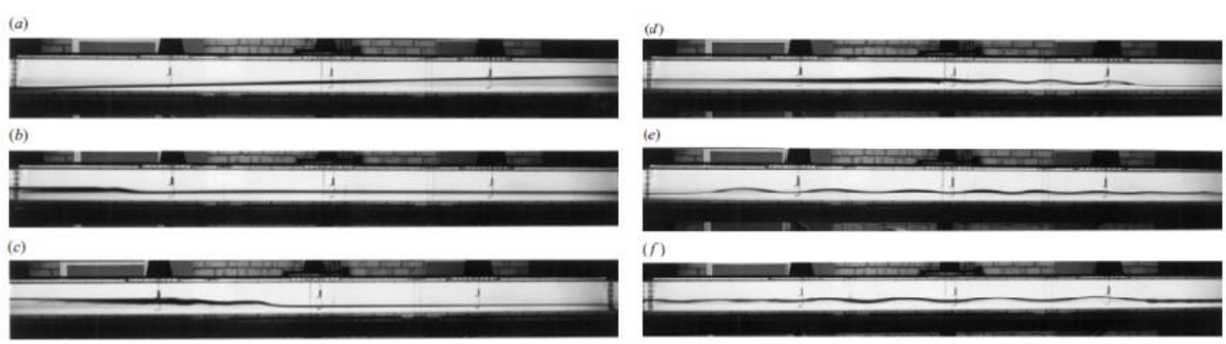

Figure 20. Photographs showing the steepening of an initial basin-scale wave to form a packet of solitons. Reproduced from Horn et al. (2001).

For small angles of tilt, the nonlinear steepening was weak and the motion was dampened by viscous effects. By increasing the angle of tilt and therefore the nonlinearity of the initial wave, the basin-scale wave was observed to steepen and evolve into a packet of solitons. In some experiments with very large tilts, an undular bore was observed, accompanied with local shear instabilities and turbulence.

5.2.1 Simulation set up

The experiments done in the laboratory tank are simulated with FINLAB. The laboratory tank with a length of 600 cm and a height of 29 cm is modelled as a rectangular mesh consisting of triangular elements (with horizontal element size Δx and vertical element size Δz). Figure 21 shows an example.

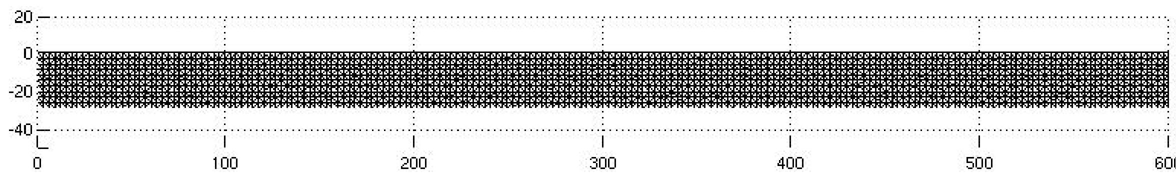

Figure 21. Mesh with 200 horizontal points and 10 vertical points.

All boundary conditions are closed boundaries with partial slip. The laboratory tank is made of glass, therefore a low wall roughness coefficient k_N of 1.10^{-4} m is chosen. The relative density difference between the two layers is 0.020, equivalent to a density difference of 20 kg/m^3. A turbulence closure model LES is chosen with a Smagorinksy constant of 0.15. The initial condition is a tilted interface at an angle similar to the tests done in the laboratory.

5.2.2 Sensitivity study

5.2.2.1 Introduction

A sensitivity study of FINLAB is performed to study the effect of varying input parameters on the model output. This analysis is also used to find the parameters that provide a good balance between numerical accuracy and computational time. The sensitivity analysis of the tilted tank experiment comprises studying the influence of changing the grid resolution, the time step, the boundary conditions, the viscosity, the turbulence closure model, the wall roughness and the Smagorinsky constant.

All numerical results will be compared to a time series of the interface displacement measured at the wave gauge in the middle of the tank for a test case where $h_2/H = 0.3$, $\theta=1.5^0$ and $\eta_0/h_2=0.9$. See Figure 22. For a more quantitative analysis, the amplitude and phase of three different peaks (see Figure 22) are calculated from the time series and compared to the numerical simulation results. The relative phase error and the amplitude error are defined as:

$$error = \left| \frac{(measured - computed)}{measured} \right| \quad (5.1)$$

With this formula, the time lag is defined as the time between the maximum of the measured peak and the maximum of the corresponding computed peak. The measured and computed peak amplitudes are compared regardless of the phase error (i.e. only height is considered, not corresponding time). Raw data of the laboratory measurements were not available. The wave periods, wave lengths and amplitudes are estimated visually from figures in the paper and therefore might contain a small estimation error.

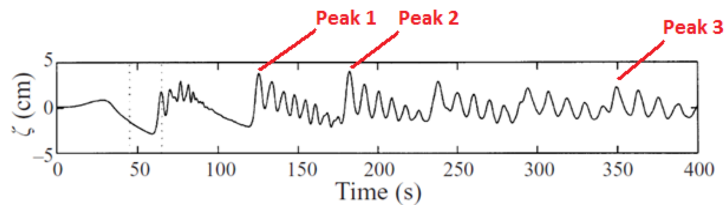

Figure 22. Time series at wave gauge B. From Horn et al. (2001).

Peak 1 has a wave length of 1 m and a wave period T of 10 s. This will be used to calculate the number of horizontal grid points per wavelength N_L and the number of time steps per wave period N_T that are required to simulate the wave with sufficient accuracy.

5.2.2.2 Grid resolution

A series of tests are undertaken to study the influence of the grid element size on the model output. The number of horizontal and vertical grid points is increased with the ratio horizontal/vertical points kept constant at 20:1, so that Δx=Δz. The time step Δt used in this series is 0.1 s.

In Figure 23, the time lags and amplitude errors are calculated for eight grids with different resolution. They decrease for higher grid resolutions. The time lags for peak 3 are larger than those for peak 1. This is because the time lag becomes larger for longer simulation times.

Figure 24 shows simulation results for the same eight grid resolutions. The legend boxes show the grid resolution (number of horizontal gridpoints x number of vertical gridpoints). The higher the resolution, the more the results resemble the laboratory results. It can be observed that Finlab reproduces both the basin-scale motion and the smaller waves riding on top. However, the smallest wave at the rear end of a wave packet is not captured. Also, the laboratory results show that the 4th peak is larger than the 3rd, the simulation results do not agree with that. The red lines in Figure 24 denote the peaks 1,2 and 3 in the numerical results. It can be observed that there is a time lag between the laboratory waves and the waves computed by Finlab. The time lag decreases for higher resolution grids.

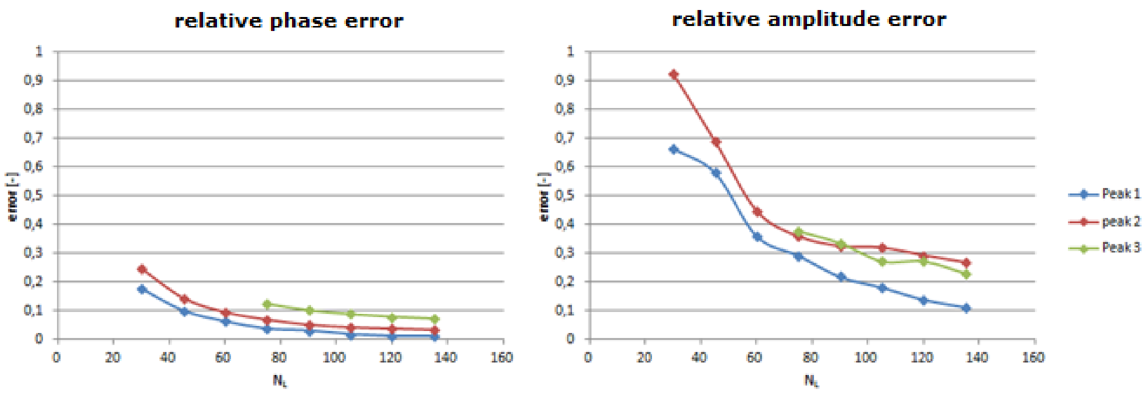

Figure 23. Relative phase and amplitude errors for simulations with different grid resolutions.

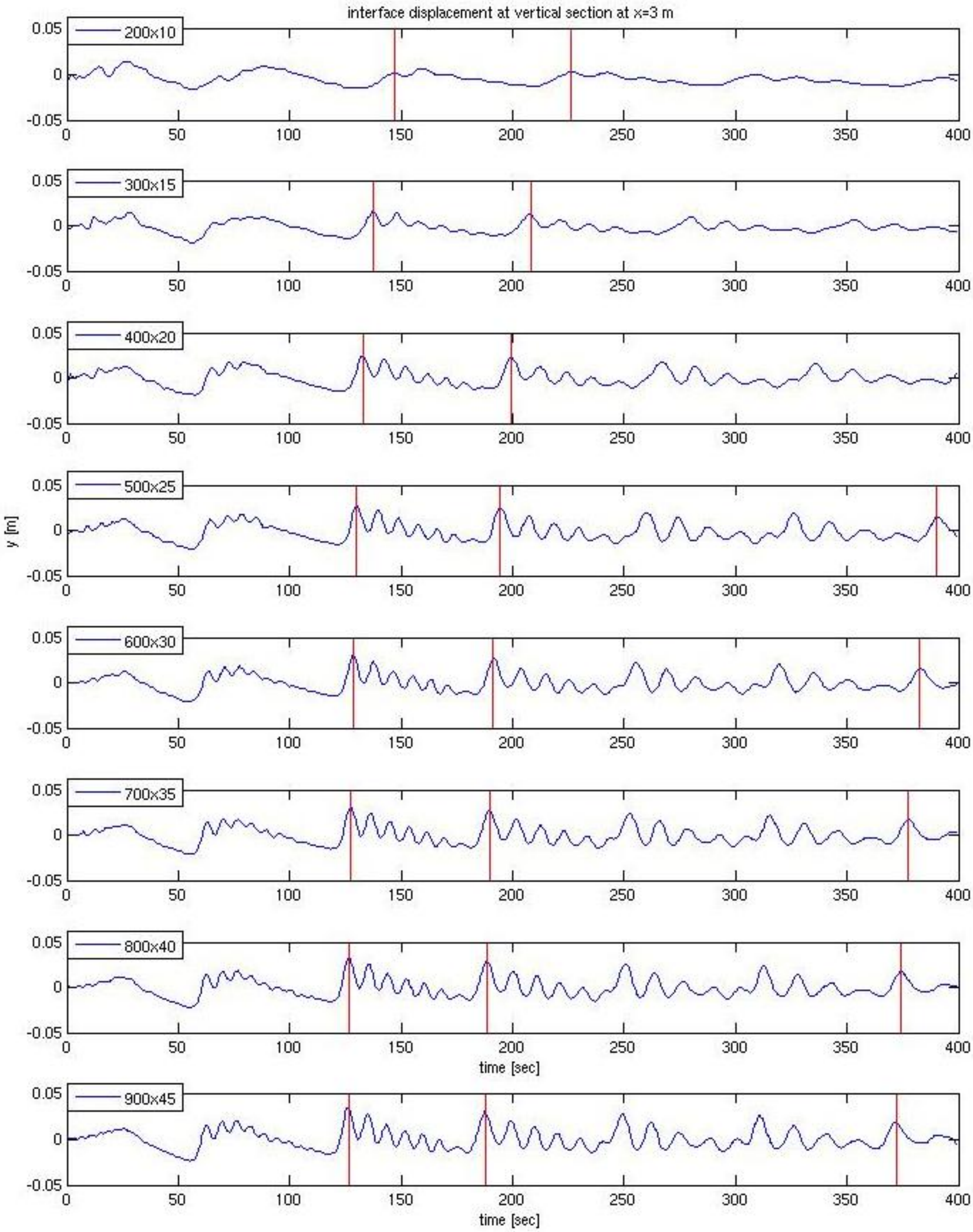

Figure 24. Numerical results for varying mesh resolutions.

An explanation for the time lag is diffusion of the interface layer. In the laboratory tests, the interface layer was approximately 1 cm at the start of a test and would thicken to 2 cm at the end. Figure 25 shows the density profiles for a vertical cross-section in the middle of the tank (x = 3 m) at the beginning and at the end of a simulation for grids with different numbers of vertical layers and a constant horizontal resolution. It can be observed that the finer grids have thinner interface layers after a simulation. This difference becomes much less pronounced for very fine meshes. For example, there is large difference between the interface thickness with 15 or 30 vertical layers, but there is a negligible difference between 50 and 85 layers. This implies that there is a limit to what increasing the vertical grid density can do for more accurate results. Even the finest grid has an interface thickness of 8 cm at the end of the simulation. This is much more than the 2 cm interface measured in the laboratory tests.

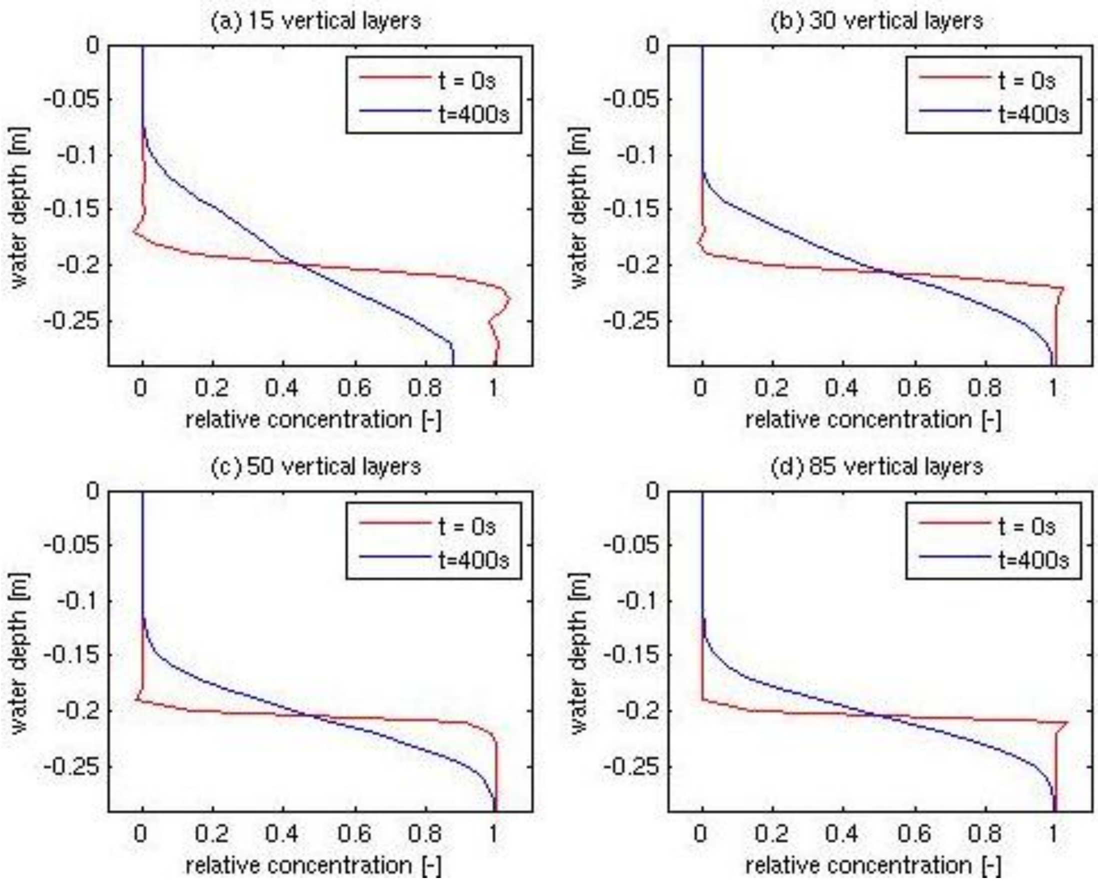

Figure 25. Density gradient over the vertical before and after the simulation for different meshes. Each mesh has 600 horizontal mesh points.

Figure 26 shows the time lags and amplitude errors if the horizontal grid size is kept constant at 90 horizontal elements per wave length and only the number of vertical layers is varied. It can be concluded that smaller element sizes give more accurate numerical results. In general, time lags are much smaller than amplitude errors. The amplitude error decreases very fast for increasing grid density. A minimum of 100 horizontal elements per wave length and 35 vertical layers must be used for good results.

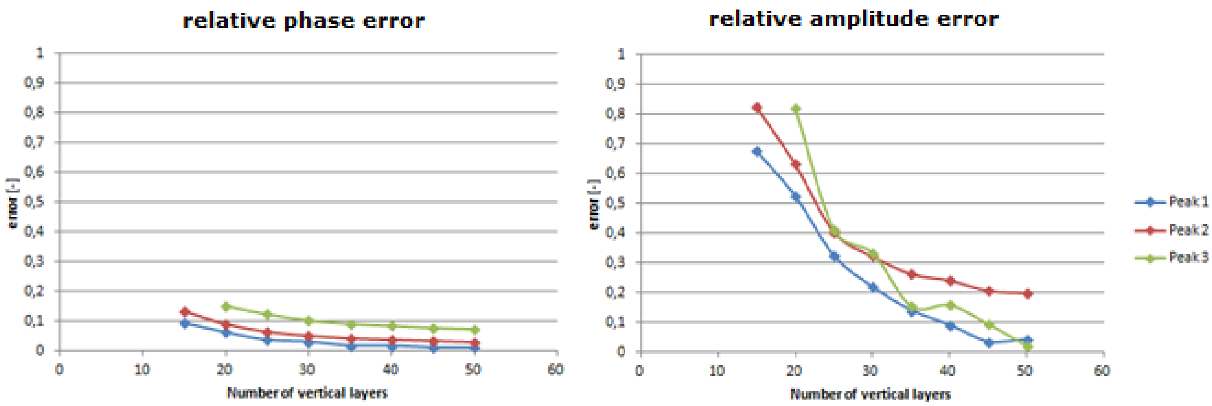

Figure 26. Time lags and amplitude errors for simulations with different amount of vertical layers.

5.2.2.3 Time step

A series of tests is carried out to study the influence of the time step on the simulation results. Table 1 gives the input parameters for each test. The Courant wave numbers have been calculated with:

$$Courant\ wave\ number = \frac{c \cdot \Delta t}{\Delta x} \tag{5.2}$$

In this equation, c is defined as the propagation speed of the wave leading the wave group after approximately 120 s.

A mesh with 90 horizontal elements per wavelength and 30 vertical layers has been used for these tests. Figure 27 shows the simulation results for different time steps. The first plot shows the laboratory solution.

Δt (s)	N_T	U (m/s)	Courant wave number (-)
0,05	202	0.097	0.48
0,075	135	0.097	0.73
0,1	101	0.097	0.97
0,15	67	0.097	1.45
0,2	51	0.097	1.94
0,25	40	0.097	2.42
0,3	34	0.097	2.90
0,4	25	0.097	3.87
0.5	20	0.097	4.84
1.0	10	0.097	9.68
1.5	7	0.097	14.52

Table 1. Time steps.

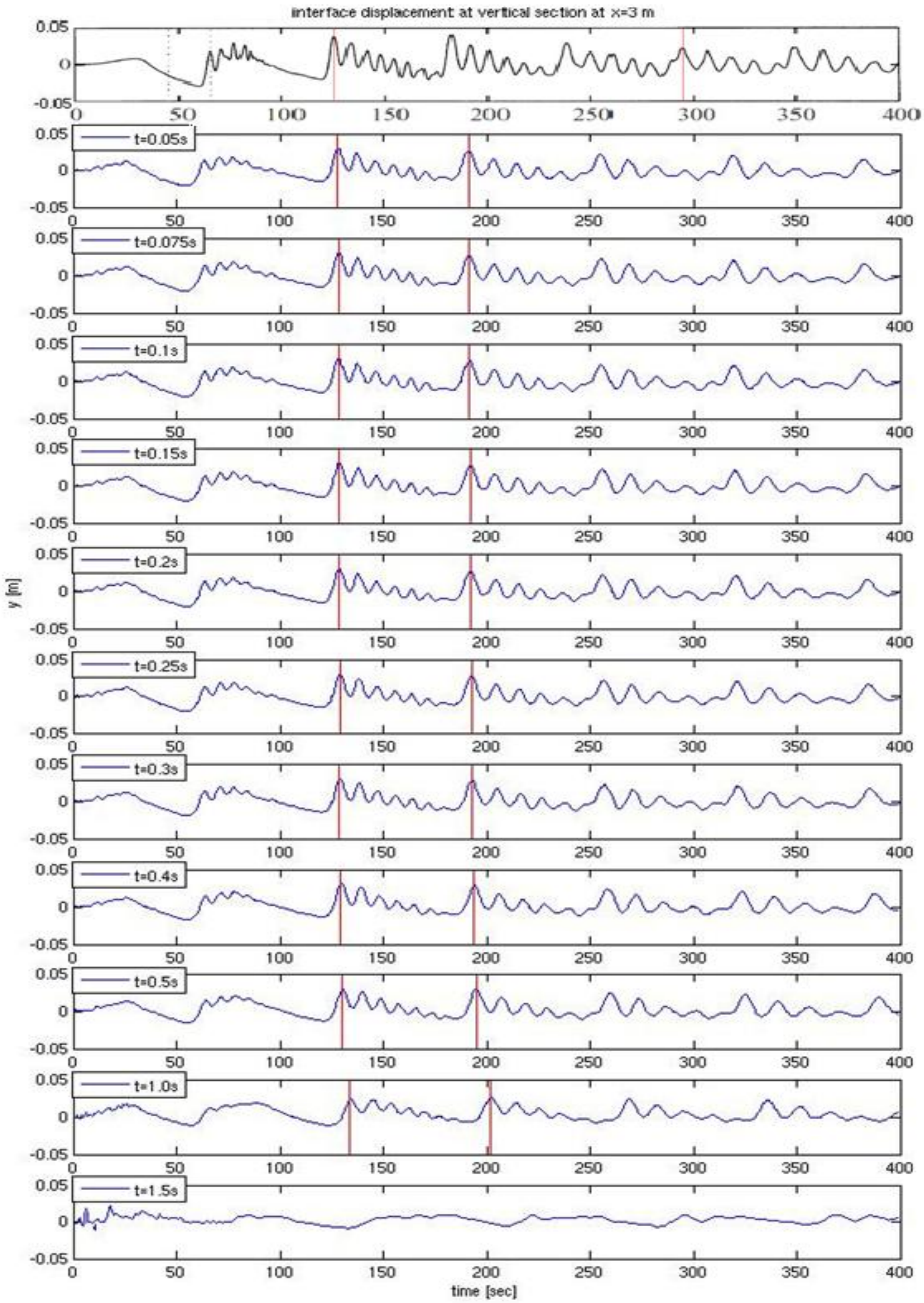

Figure 27. Laboratory result (first plot) and numerical results for varying time steps (t = time step in this figure).

Figure 28 shows the time lags and amplitude errors for the simulations from Table 1. The difference between the simulation results for varying time steps are much smaller than for varying element sizes. The errors do not decrease much with decreasing time step.

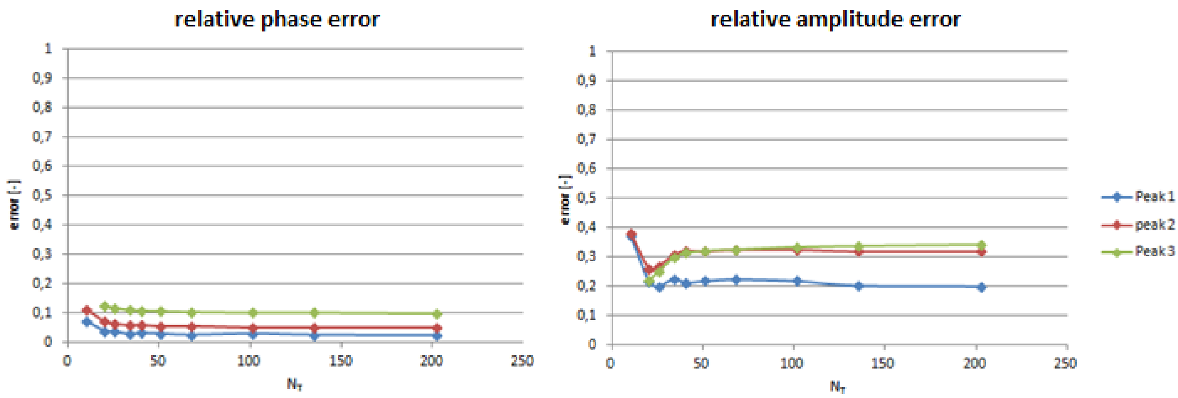

Figure 28. Phase error and amplitude errors.

It can be concluded that the time step does not have a large influence on the amplitudes and phases of the waves in the tank, provided that $N_T > 50$. Results become less accurate for time steps larger than 1 s (see Figure 27). This coincides with Courant numbers approaching 10. Based on Figure 28, it is recommended to take a minimum of 50 time steps per wave period.

5.2.2.4 Other parameters

Some other numerical parameters are now looked into. For these tests, 100 horizontal elements per wave length and 35 vertical layers have been used. A time step of 0.1 s is taken.

- **Kinematic viscosity**

First, a series of tests is carried out to study the influence of the kinematic viscosity on the simulation results. The kinematic viscosity of a fluid is directly related to its temperature. Six simulations were carried out with values for the viscosity in the range of $0.5E^{-6}$ to $1.5E^{-6}$ (related to water temperatures ranging from 5 to 60°C). One simulation was set up with a viscosity of $1E^{-5}$. Figure 29 shows the results. It can be observed that the results are not influenced by the viscosity for values around $1E^{-6}$. However, the result for $1E^{-5}$ (blue line) shows a big difference. The wave lengths are longer and the wave amplitudes are dampened much faster.

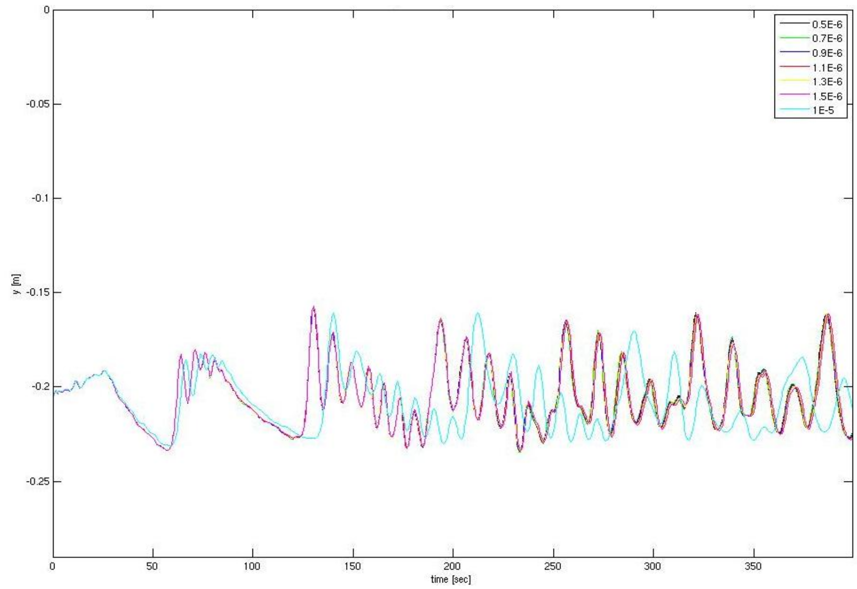

Figure 29. Interface displacement in the middle of the tank for six simulations with different kinematic viscosity.

- **Boundary conditions**

The influence of the boundary conditions is studied. The tank consists of four glass walls. Therefore all four boundary conditions are closed boundaries. As mentioned in the model description, closed boundaries can have a partial slip (some friction) or a free slip condition (no friction). The figures below illustrates the difference in the horizontal velocity profile for partial slip boundaries (with k_N = 1x10^{-4} m) and free slip boundaries. As could be expected, the horizontal velocity is influenced by the partial slip boundaries and experiences some friction at the boundaries.

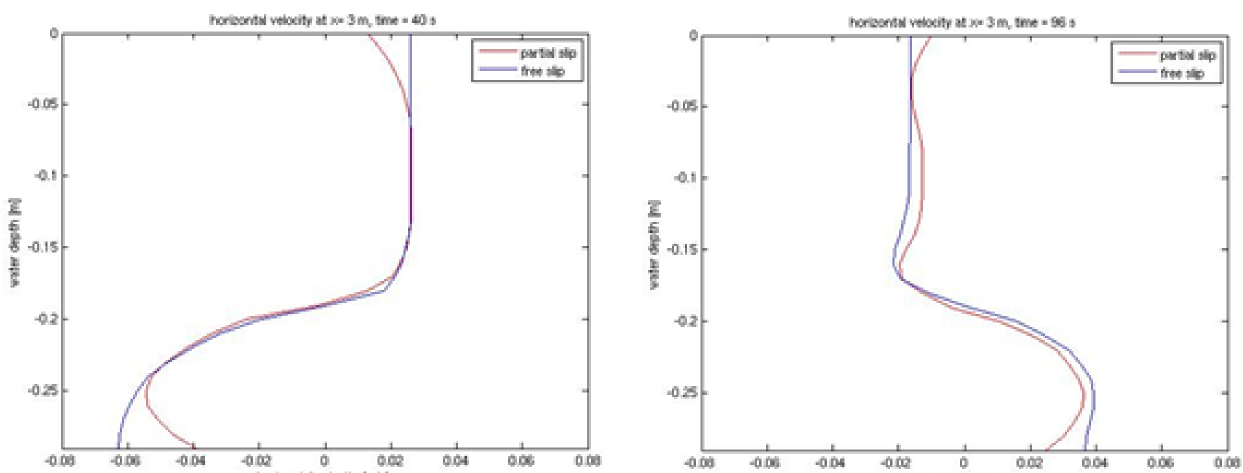

Figure 30. Vertical profiles of horizontal velocities at two different times for a 900x45 grid.

This has consequences for the computed flow in the tank. Figure 31 shows the time series of the interface displacement in the middle of the tank for two simulations with free slip and partial slip boundary condition. The waves with the free slip boundaries have higher amplitudes and slightly higher frequencies.

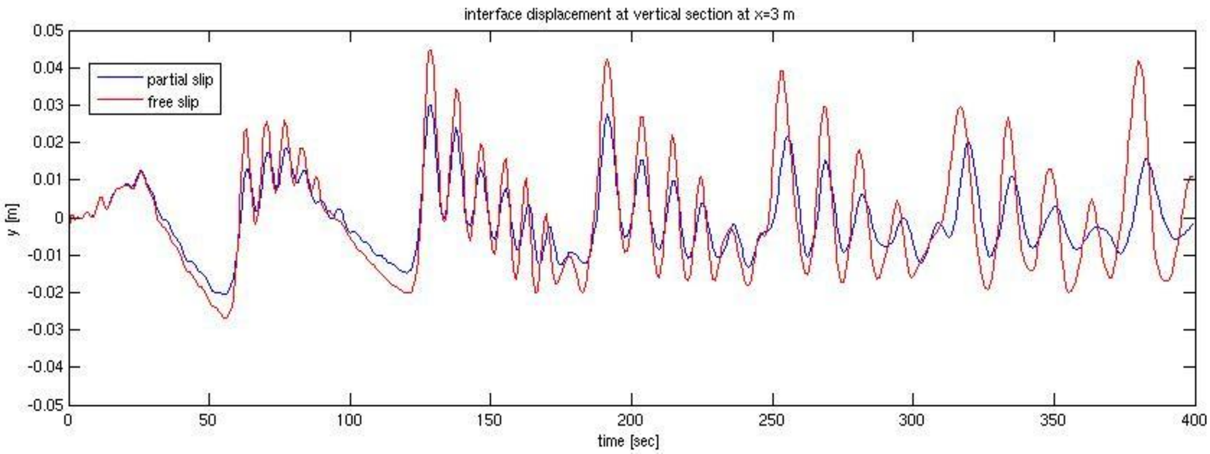

Figure 31. Simulation results for different boundary conditions with a 600x30 grid.

Free slip boundaries are unrealistic from a physical point of view. Although the results for free slip conditions show a smaller time lag, the results with partial slip boundaries show more accurate amplitudes. The time lag improvement with the free slip boundaries is very small, therefore partial slip conditions will be used in future simulations.

- **Turbulence closure model**

Simulations have been run with the K-epsilon model and the LES model (with Smagorinsky constant=0.15). A comparison is shown in Figure 32.

Both model simulations now showed good resemblance to the laboratory results. The peaks of the waves computed with the K-epsilon model are closer to the laboratory values and have a slightly smaller time lag than the LES computed waves. However, with the K-epsilon model, the peak at t = 380 s is higher than the peak at t = 320 s. This is not the case in the laboratory test results and the LES agrees better with the laboratory tests on this point. Finally, it is remarked that the computational time is much higher (20-30%) when using the k-epsilon model. This can be explained by the fact that the K-epsilon model has to solve two extra equations compared to the LES model, which will cost more time.

Overall, the K-epsilon model gives the most accurate results for this test situation and is therefore recommended. However, as the differences between K-epsilon and LES are small LES can be used if it is necessary to reduce the computational time.

(Note: At the time of the model validation the K-epsilon model did not work correctly. All validation tests were therefore performed with the LES model. Later in this project, changes were made in the source code that solved the instabilities and made it possible to use the K-epsilon model.)

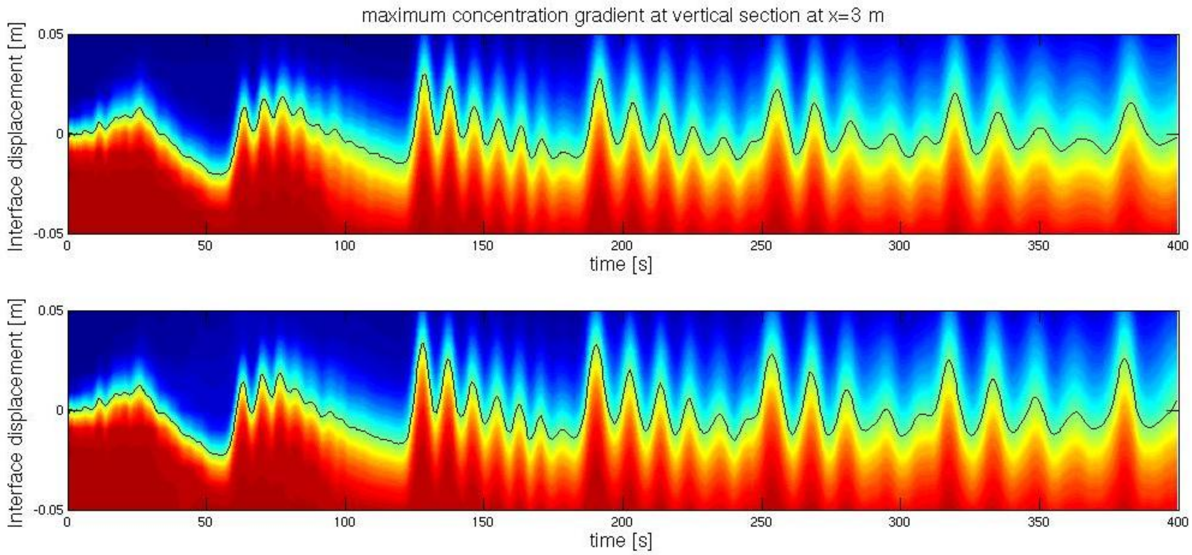

Figure 32. Density distribution in time with Large Eddy Simulation (top) and K-epsilon model (bottom).

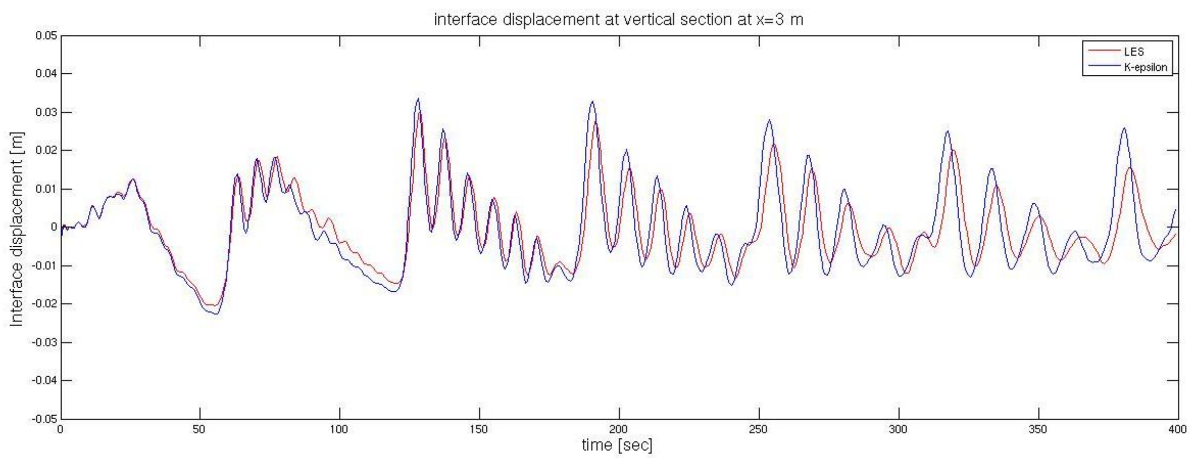

Figure 33. Comparison between numerical results with LES and K-epsilon turbulence model.

- **Nikuradse wall roughness**

The Nikuradse wall roughness determines how much friction the walls will exert on the flow nearby. Figure 34 shows three simulations with different Nikuradse values ranging from 1.10^{-3} m to 1.10^{-5} m. A higher coefficient and therefore a higher wall roughness, leads to waves with lower amplitudes. It has negligible influence on the phase speed of the waves in the tank.

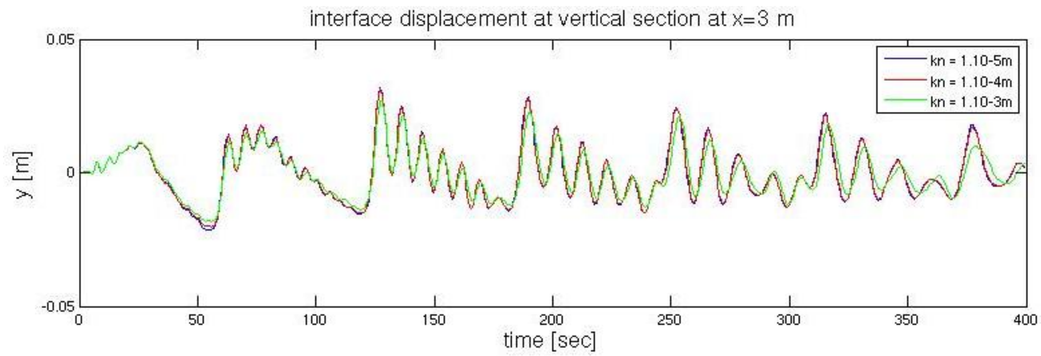

Figure 34. Interface displacement for simulations with different Nikuradse wall roughness coefficients.

It is decided to use a wall roughness of 1.10^{-4} m. This gives the smallest amplitude errors and is a realistic value for a glass wall.

Figure 35 shows the horizontal velocity in the water column for two simulations with different wall roughness. It can be seen that there is only a very small difference in velocity very close to the upper and lower boundaries of the tank.

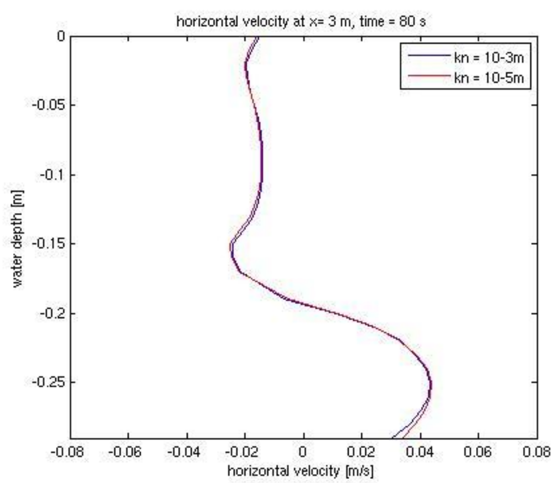

Figure 35. Horizontal velocity profiles for different wall roughness coefficients.

- **Smagorinsky constant**

In the LES model, the Smagorinsky constant is used to find an expression for the mixing length. In literature, values for the Smagorinsky constant vary from 0.05 to 0.2 (Labeur 2009). Figure 36 shows four simulations with different Smagorinsky constants. The differences are quite large. The smaller Smagorinsky values show good wave periods but computed amplitudes are too high. The wave amplitudes and periods are too low for the higher Smagorinsky numbers. This result must be kept in mind because it may have implications for simulations on larger scales. It is therefore recommended to vary the Smagorinksy constant in those larger-scale simulations as well.

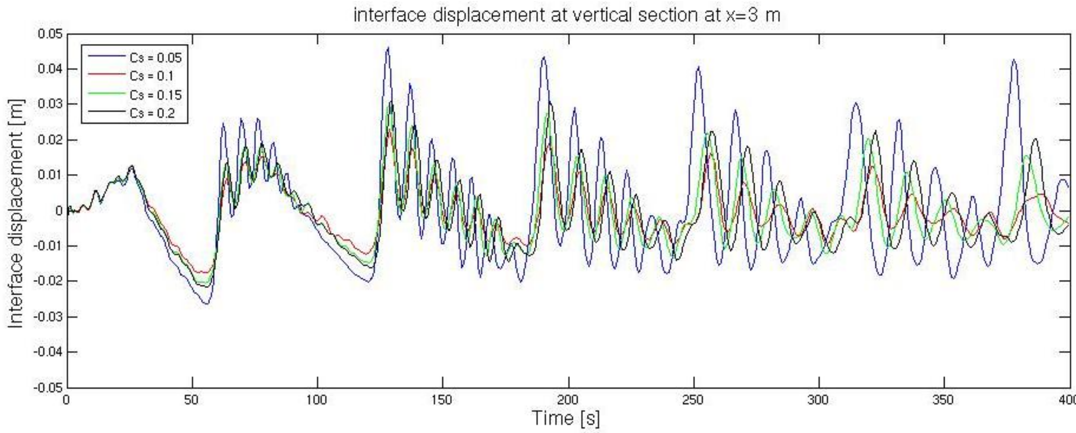

Figure 36. Simulation results with four different Smagorinsky constants.

A Smagorinsky constant of 0.15 will be used in further simulations. It gives the best combination of small time lag and small amplitude errors. Simulating amplitudes accurately is important for the structural design of the water intake risers of the FLNG vessel. For those simulations, it is recommended to take a slightly higher Smagorinsky value. Amplitudes will be more important than time lags and it is better to have an overestimation than an underestimation for design purposes.

5.2.3 Flow behaviour

5.2.3.1 Introduction

The laboratory experiments were carried out to investigate the parameters that define the different degeneration regimes in lakes. The influence of the angle of tilt was looked into to gain a better understanding of the relation between the flow behaviour and generation mechanisms. The sensitivity analysis has resulted in a couple of requirements for accurate internal flow simulations. The laboratory experiments on angle of tilt will be numerically simulated to test if the set up works well. All simulations are therefore run with a mesh that has 35 vertical layers, 100 horizontal elements per wave length and 50 time steps per wave period.

5.2.3.2 Angle of tilt

Figure 37 shows the results for five simulations with different initial angles of tilt (right hand side). They are compared to the laboratory results (left). As the angle of tilt increases, the nonlinearity of the system increases (Horn et al. 2001). It can be observed that the initial wave steepens more quickly and the number and amplitudes of emerging solitons grow larger. In plot (a) and (b), the waves are dampened before they can steepen and no solitons are generated. In (c), (d) and (e), the initial angle of tilt is larger and viscous damping is no longer dominant. The initial wave evolves in a series of solitons that travel up and down the tank.

It can be concluded that the Finlab results show good resemblance to the laboratory results.

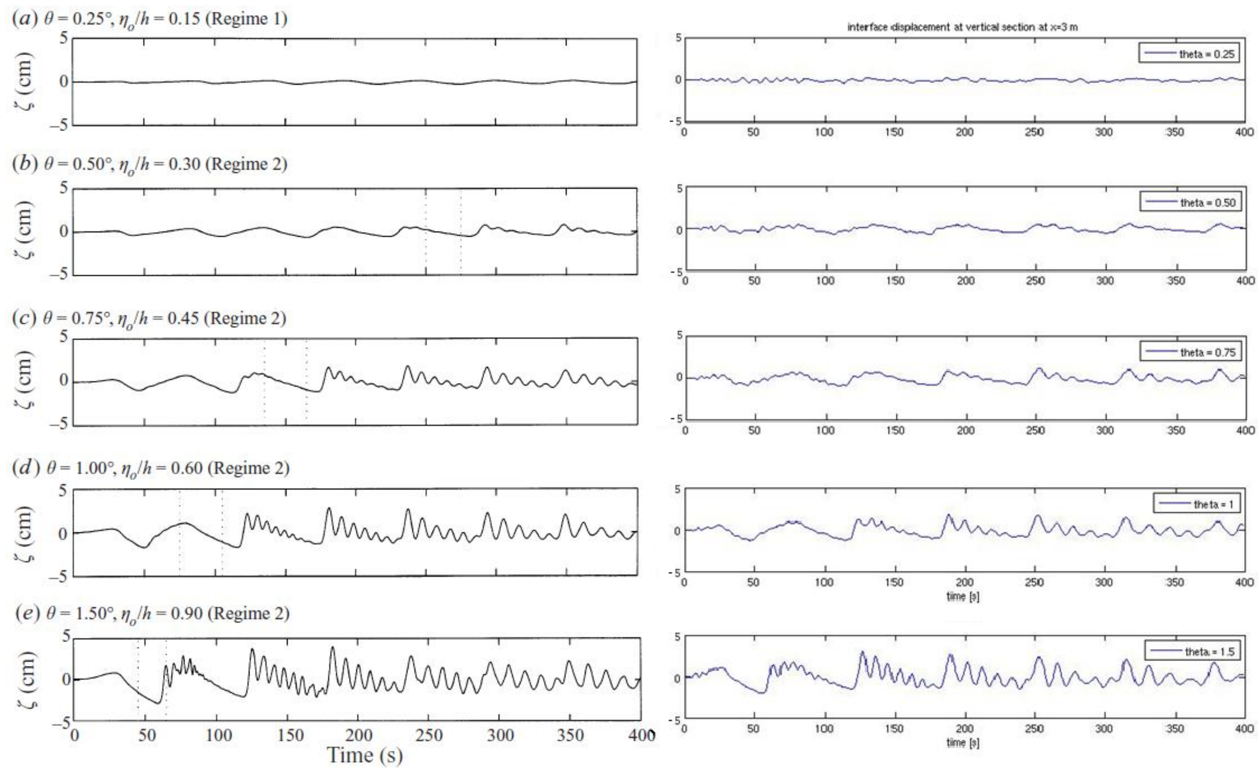

Figure 37. Comparison between laboratory (left) and simulation (right) results for different initial angles of tilt. In this figure, h denotes the thickness of the lower layer.

5.2.3.3 Density differences

Another interesting parameter is the density difference between the two layers in the tank. Figure 38 shows the results for three simulations with different densities. It can be concluded that larger density differences lead to higher wave speeds. This can be explained by looking at (3.36) and (3.38); the square root of the density difference and the phase speed are proportional.

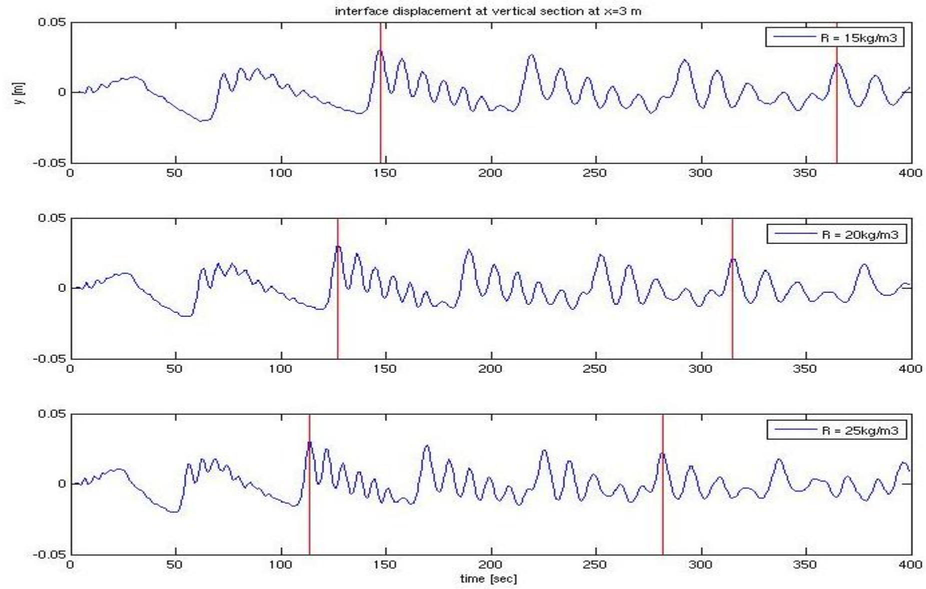

Figure 38. Numerical results for simulations with varying density difference R.

5.2.4 Conclusion

Using small grid elements gives better results because the phase and amplitude accuracy increases for higher grid resolutions. Results with smaller time steps also show better resemblance to laboratory time series. It can be concluded that a minimum of 100 horizontal elements per wave length, 35 vertical layers and 50 time steps per wave period is required for reliable simulation results.

Closed boundaries with partial slip conditions and a representative Nikuradse wall roughness work well in this test.

Some differences between the laboratory and numerical results remain regardless of the input variables:

- The laboratory results show that the 4th peak is larger than the 3rd, the simulation results do not agree with that.
- The last soliton in each wave packet in the laboratory experiments is not computed in the simulation results.
- The diffusion near the interface is larger in the numerical results than in the laboratory results.

5.3 Tilted tank with sloping bottom test case

5.3.1 Introduction

Laboratory experiments were carried out by Boegman, Ivey et al. (2005) (Boegman et al. 2005)(Boegman et al. 2005)(Boegman et al. 2005)(Boegman et al. 2005)(Boegman, Ivey et al. 2005)(Boegman, Ivey et al. 2005)(Boegman, Ivey et al. 2005)(Boegman, Ivey et al. 2005)(Boegman, Ivey et al. 2005)(Boegman, Ivey et al. 2005)(Boegman, Ivey et al. 2005)in a tank similar to the one described in paragraph **Fout! Verwijzingsbron niet gevonden.**. For this series of tests, a uniform slope of 1/10 or 3/20 was inserted that extended the entire height of the tank. Again, the tank was rotated. This resulted in a tilted interface that could be characterized as either downwelling or upwelling. Rotating the tank back to a horizontal position caused the steepening of a nonlinear basin-scale wave and a resulting packet of high frequency solitary internal waves that propagated throughout the basin. The goal of this study was to quantify the energy loss from the breaking of internal solitary wave packets as they shoal near the slope of a closed basin with two-layer stratification.

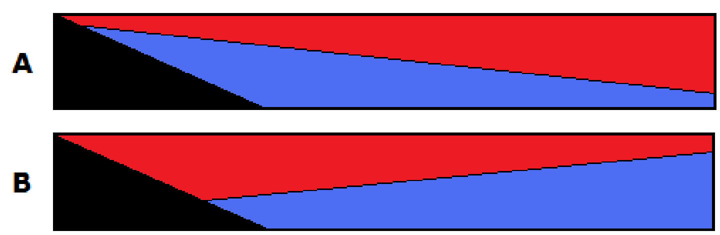

Figure 39. Schematic diagram of experimental set up with initial condition with upwelling (a) or downwelling (b) at the slope.

The solitary waves provide the crucial energy transfer between the large scale motions forced by the initial tilted interface and the small-scale turbulent dissipation and mixing along sloping boundaries. In cases where the characteristic length scale of a particular solitary wave is less than the characteristic slope length, waves will break on the sloping boundaries of the basin.

The breaker type can be expressed in terms of an internal Iribarren number ξ, which is defined as the ratio of the wave slope to the boundary slope.

In the laboratory tests, breaking was observed in the form of spilling, plunging, collapsing and Kelvin-Helmholtz breakers.

Breaking of a single wave resulted in an energy loss of 10-75 % of the incident wave energy. The remaining energy was transferred to a reflecting long wave. The energy was lost to dissipation and mixing. The mixing efficiency depended on the breaker type and ranged from 5-25 %.

5.3.2 Simulation set up

Figure 40 shows an example of a mesh used to simulate the experiments in a tank with sloping bottom.

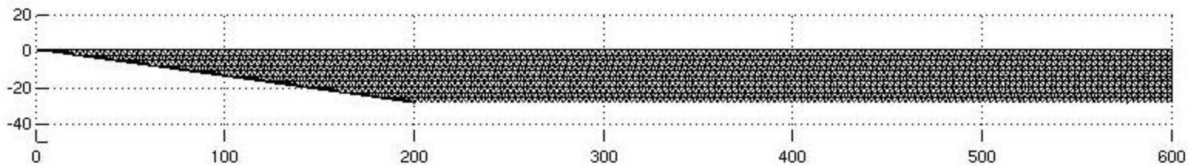

Figure 40. Mesh for tank with sloping bottom.

The numerical set up is partly based on the conclusions of the tests in the tank with a flat bottom. Four partial slip boundary conditions are used with a Nikuradse wall roughness of 1.10^{-4} m. The LES model has been used for all simulations in the tank.

For an accurate representation of the wave breaking on the slope, a grid is used with 40 vertical layers, 120 grid elements per wave length and 100 time steps per wave period.

5.3.3 Validation test

For this validation test, a number of laboratory tests are simulated with Finlab. The results will be visualized in different ways to be able to make a good comparison with the flume experiments.

The figure below shows the wave field evolution for a test case with $h_2/H = 0.29$ and $\eta_0/h_1 = 0.90$. From the initial tilted interface, a surge propagates through the basin and solitary waves are generated. Wave breaking occurs at the slope. The video frames on the left hand side of the figure show the laboratory experiment, the plots on the right hand side show the numerical results. The wave breaking mechanism compares quite well.

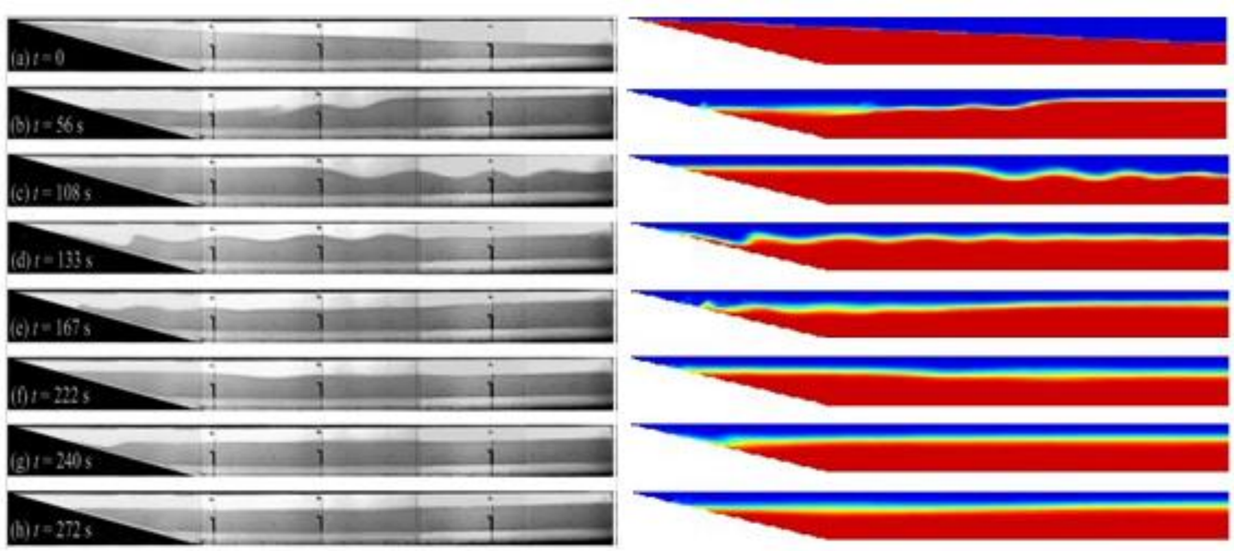

Figure 41. Comparison laboratory experiment (left) and numerical simulation (right) for $h_2/H=0.29$ and $\eta_0/h_1=0.90$. Left figure reproduced from (Aghsaee et al. 2010).

A more accurate comparison between laboratory and numerical results can be made by looking at the time series of the interface displacement. Figure 42 shows that there is a time lag. The waves computed with the model lags behind the laboratory waves. However, the numerical model captures all the significant flow features.

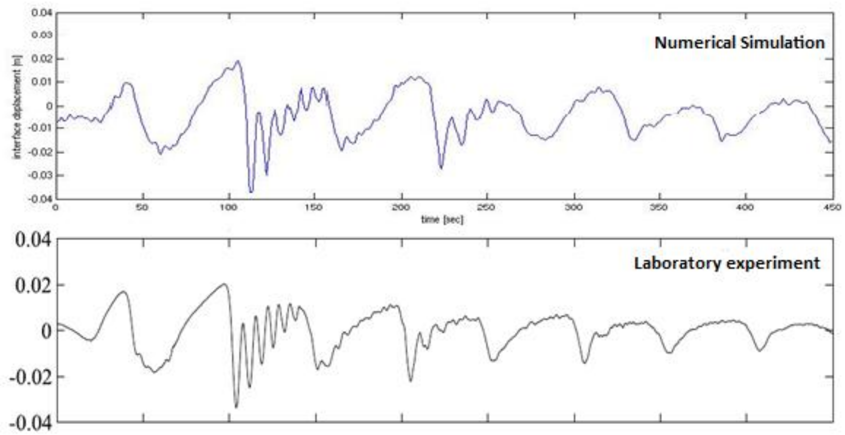

Figure 42. Comparison time series of interface displacement at x= 3.07 m for numerical and laboratory experiment.

As mentioned before, the wave breaking mechanism depends on the slope of the bottom and the slope of the wave. In Figure 43, the wave breaking mechanism is compared for the numerical simulation (left) and the laboratory test (right). The initial conditions (bottom slope = 3/20, $h_1/H = 0.2$ and $\eta_0/h_1 = 0.86$) lead to a plunging breaker.

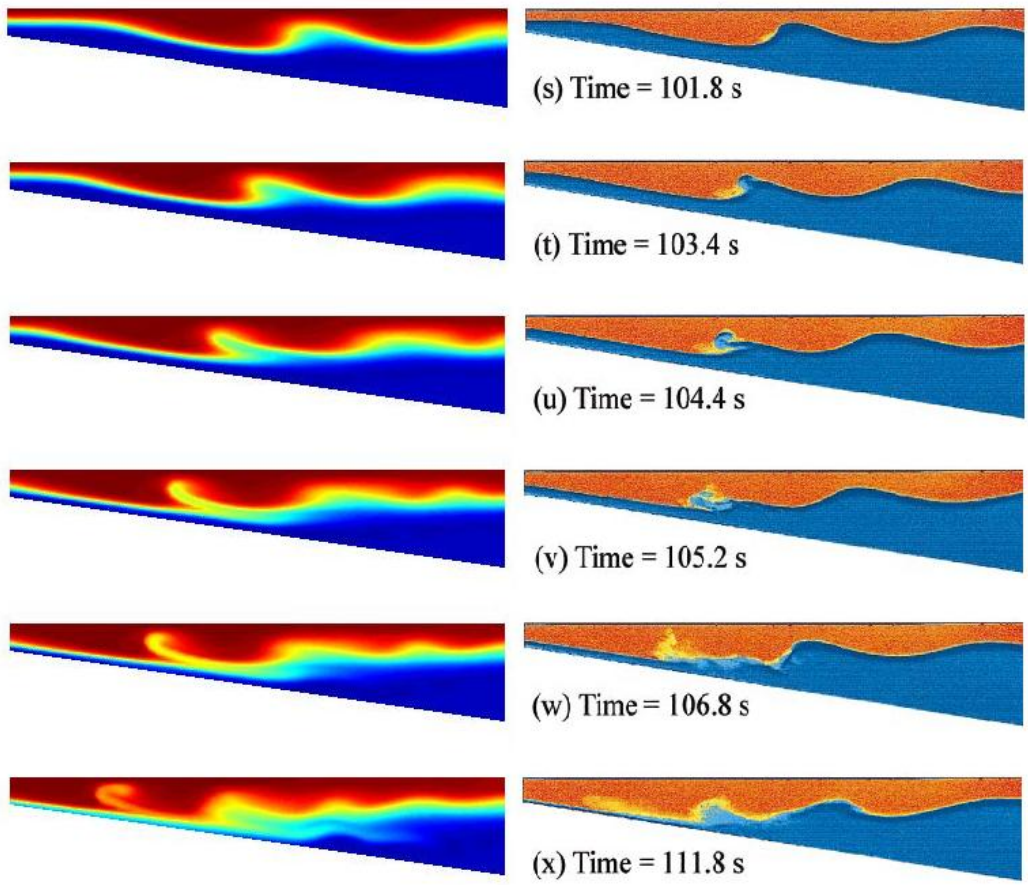

Figure 43. Numerical results (left) and laboratory results (right) for a plunging breaker.

Finally, the mixing rate and the growth of the interface layer thickness are looked into. Figure 44 shows a simulation on a flat bed and on a sloping bed. It can be seen that there are more waves in the tank with the flat bed. This is because waves do not break and therefore there is no loss of energy. This is consistent with the conclusions from the laboratory tests, where 10-75 % of the incident wave energy was lost due to breaking.

It can also be observed that solitary waves in the sloping tank seem to be the same length but the basin scale wave is shorter for the sloping bottom test case. Because of the presence of the slope, the waves are reflected at an earlier time.

Finally, it can be concluded that breaking waves do not generate significantly thicker interface layers than non-breaking waves. According to the laboratory tests, the mixing efficiency ranged from 5-25 %.

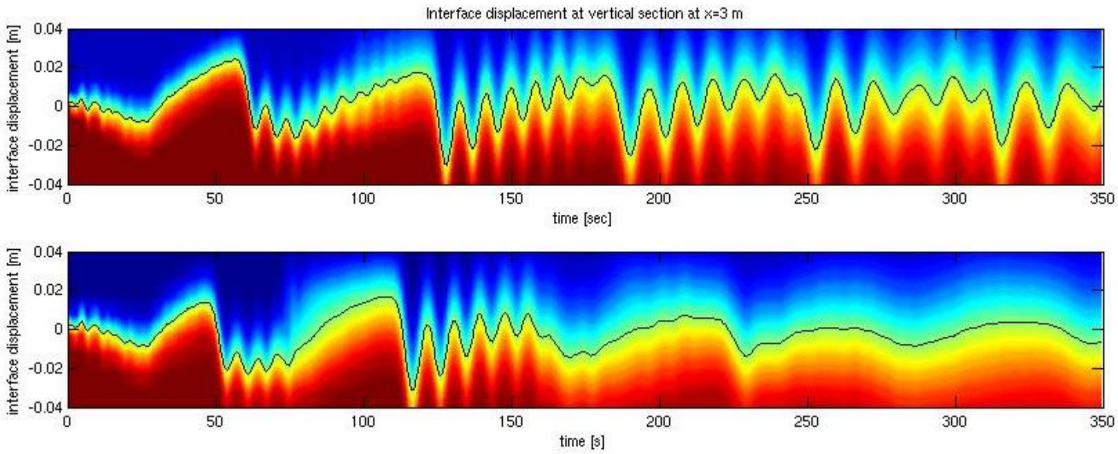

Figure 44. Simulation results for h_2/H=0.29 and η_0/h1=0.90 with a flat bed (upper figure) and with a sloping bed (lower figure).

5.3.4 Conclusion

Finlab is capable of simulating wave breaking. All the major flow features are computed, although with a small time delay compared to the laboratory results. The conclusions on the numerical parameters that were made in paragraph 5.2.4 are valid for this test case.

The manner in which the waves break depends on the internal Iribarren number. Wave breaking leads to damping.

5.4 Lee wave test

5.4.1 Introduction

As mentioned previously, stratified flow over a bottom obstacle is a common way in which solitons are created. The waves downstream of the obstacle are called lee waves. It is well worth investigating this generation mechanism a bit further.

Kranenburg and Pietrzak (1990) describe a mathematical model and laboratory experiments that deal with two-layer flow over small-scale bottom topography in shallow water.

The laboratory experiments were carried out in a flume with a length of 130 m and a width of 1 m. A section of 64 m was adapted for steady two-layer flow. A density difference of 24-25 kg/m^3 was maintained and flow rates ranged from 23 to 26 L/s. Both layers had a height of approximately 0.20 m. A cosine-shaped obstacle with a length of 20 cm and height of 4 cm was installed on the bottom. In the flume experiments, the flow over the obstacle generated a stationary lee wave train at the interface depth.

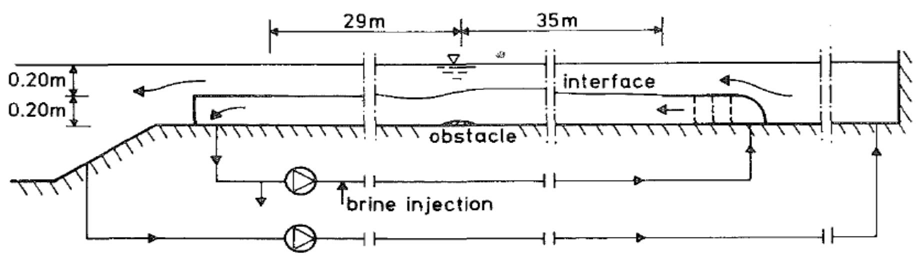

Figure 45. Experimental set up (Kranenburg and Pietrzak 1990).

Tests were performed with Froude number up to 0.90. The flow became unstable for higher Froude numbers. Negligible mixing was observed between the layers and this was explained by the small velocity differences between both layers.

The wave amplitudes were measured and compared to the theoretical lee wave amplitudes calculated with the mathematical model, which is based on the Boussinesq-equations. It takes into account vertical accelerations and damping, and assumes quasi steady flow.

Calculated wavelengths were compared to measured wavelengths. When the real length of the obstacle was used to calculate the wavelengths, amplitudes were 40% too low. In the laboratory tests, flow was seen to separate from the obstacle and reattached a certain distance downstream from it. The effective length of the obstacle was therefore 0.34 m and substituting this value in the equations gave better results.

Another issue was wave damping. In the calculations, bottom, sidewall and interface shear stresses were taken into account assuming quadratic friction laws. The constant friction factors in these expressions were taken from literature. Wave damping was underestimated with the assumed friction coefficients, therefore they were doubled. These calculations agreed better with the laboratory results. This is illustrated in Figure 50.

5.4.2 Model set up

For the numerical simulations, a grid is used that has a length of 64 m and a height of 0.4 m. The obstacle is located at x=29 m, is cosine-shaped and has a height of 4 cm. The following boundary conditions are used:

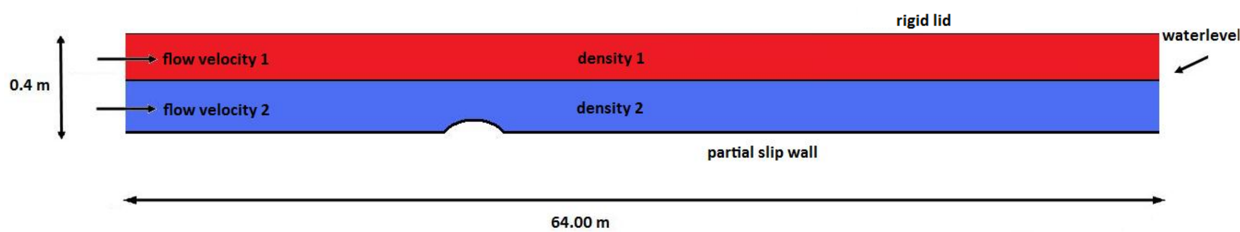

Figure 46. Boundary conditions for lee wave test.

The choice for the boundary conditions is discussed in section 5.4.3.1. The LES turbulence closure model is used with Smagorinsky constant 0.15.

The domain is very long. To keep the CPU time acceptable, a mesh is created that has the highest concentration of grid points near the obstacle, and becomes coarser near the inflow and outflow boundaries.

5.4.3 Sensitivity analysis

5.4.3.1 Boundary conditions

The choice for the boundary conditions is very important for this test. For the water surface, a free surface boundary condition and a rigid lid boundary condition were compared. A first test showed that the free surface condition was not suitable for this test because the inflow boundary (velocity) created an initial surface disturbance that took a long time to die out. For that reason, a rigid-lid boundary condition is chosen with partial slip.

The outflow boundary is defined as a fixed water level. Simulation results show that this boundary has influence on the flow upstream. The longer the simulation time, the further upstream the boundary influence is noticed. Another option is imposing outflow velocities, but this does not work well because the inflow boundary conditions are also velocities.

5.4.3.2 Simulation time

A steady two-layer flow developed in the laboratory experiments. In the numerical model, a balance must be found between the minimum time the waves need to fully develop, and the maximum time that is determined by the upstream-influencing outflow condition.

Figure 47 shows the interface displacement at different times.

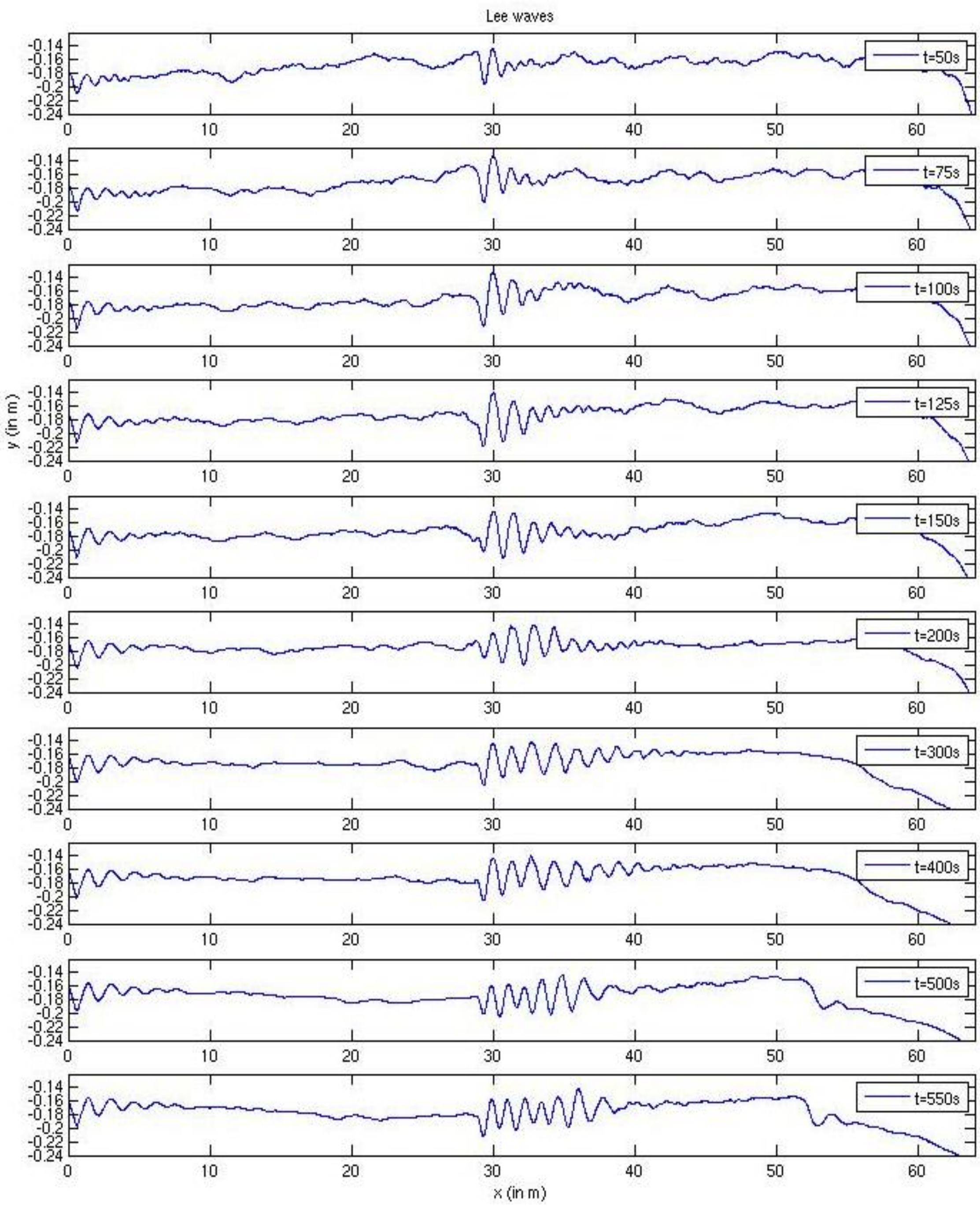

Figure 47. Lee wave formation and outflow boundary influence in time. Obstacle is at x = 29 m.

The figure clearly shows that if the simulation time is too short (50-100 s), the lee waves have not formed, but if the simulation time is too long (500-550 s), the lee waves are influenced by a disturbance caused by the outflow boundary.

This problem can be avoided by moving the outflow boundary further away from the obstacle. A consequence of this is that the flow is not steady in the entire domain, which is the case in the laboratory test. Another solution is to imitate the laboratory experiment and create an additional horizontal wall near the outflow boundary. This is illustrated in Figure 48.

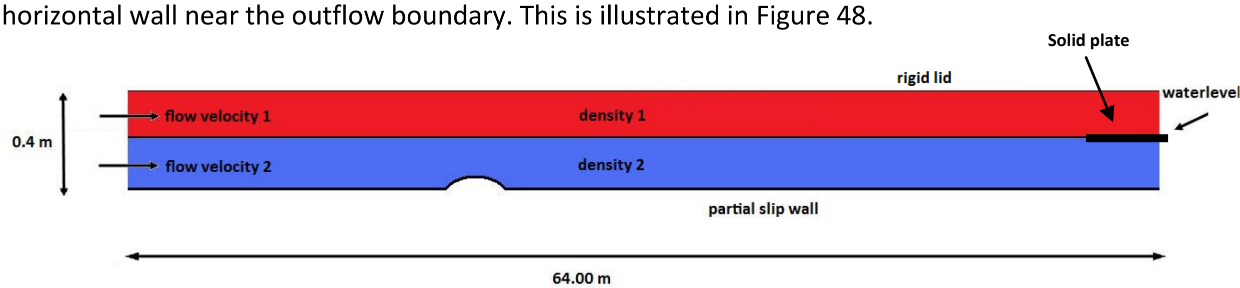

Figure 48. Boundary conditions.

Figure 49 shows the result for this test. There is still an abnormality at the downstream end of the numerical domain, but in contrast to the disturbance mentioned above, this one does not travel upstream.

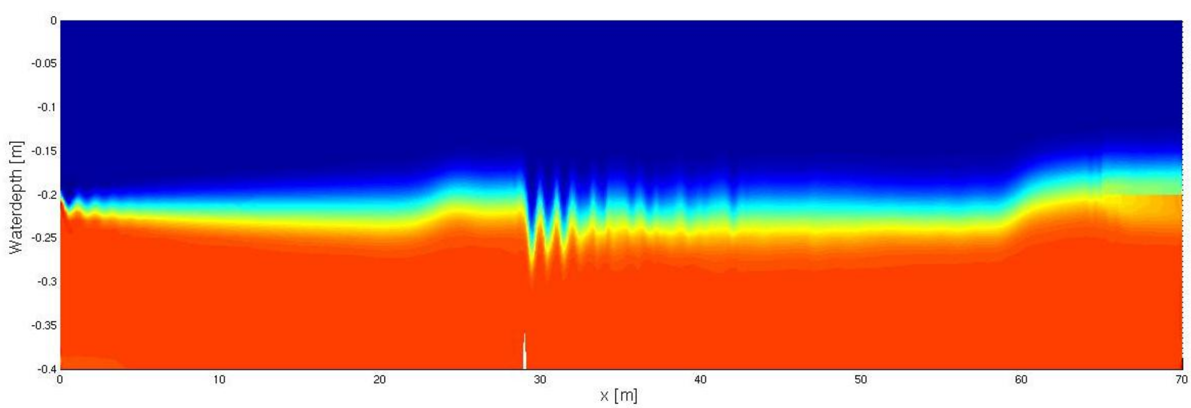

Figure 49. Simulation result for grid with plate at downstream end.

5.4.3.3 Test cases

Three test cases described in the paper are simulated. The input parameters are summarized in the table below.

Test number	U_1 (m/s)	U_2 (m/s)	h_2 (m)	$\Delta\rho$ (kg/m^3)	F (-)
3	0,144	0,09583	0,24	25	0.83
2	0,150	0,1	0,24	25	0.86
1	0,153	0,102	0,24	25	0.88

Table 2. Input parameters lee wave test.

The figure below shows the interface displacement for all three tests computed with the numerical model (right) and the solution described in the paper (left). In the figures on the right hand side, the crosses denote laboratory observations, the solid curve the analytical solution with friction factors for gradually varying flow and the dashed curves the analytical solution with double friction factors.

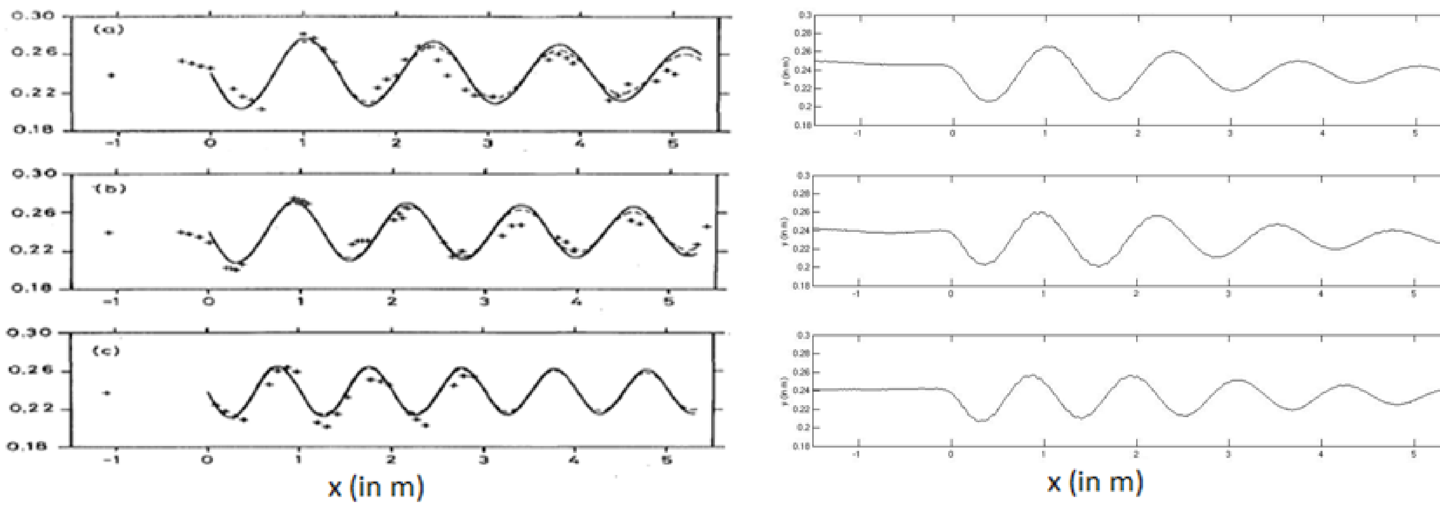

Figure 50. Comparison analytical solution (left) and numerical results (right). Upper figures: test 3, middle figures: test 2, lower figures, test 1.

The computed waves are longer than the theoretical waves. The numerical results also show much more damping then the analytical solution predicts. Numerical damping is also larger than the observed damping in the laboratory tests, although the differences here are smaller than compared with the analytical damping.

5.4.4 Flow behaviour analysis

5.4.4.1 Obstacle length

A series of tests is performed to see the influence of the obstacle length on the wave formation. It can be concluded that the lee waves are longer and higher for longer obstacles. The expression for the wave amplitude in (3.12) confirms this conclusion.

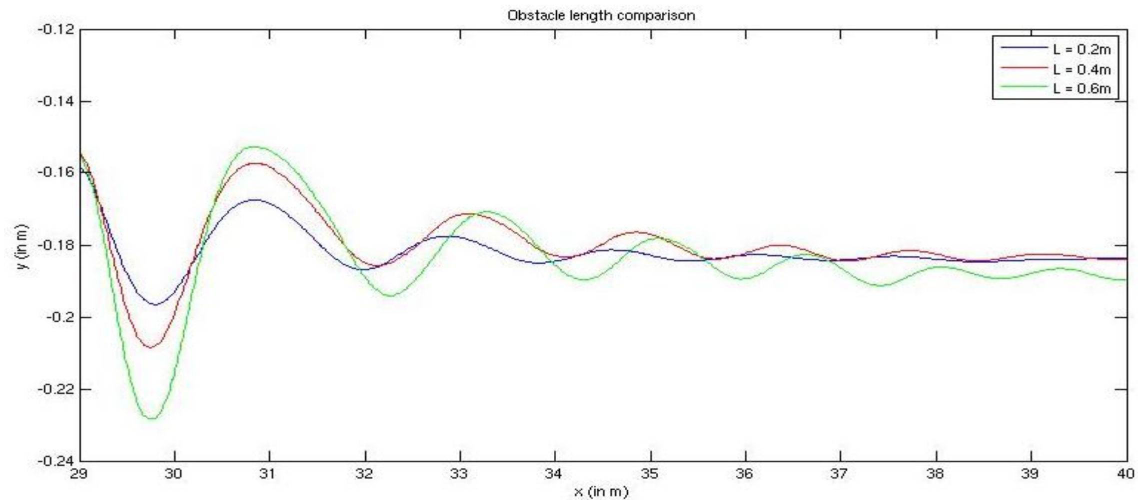

Figure 51. Interface displacement for three simulations with different obstacle length.

5.4.4.2 Obstacle height

Similar to the obstacle length, the influence of the obstacle height on the lee waves is studied. As follows directly from (3.12), if the obstacle height h_b is increased, the wave amplitude η should increase. Figure 52 shows the numerical results for three simulations with different obstacle heights. From the simulations it follows that higher obstacles do indeed generate higher lee waves.

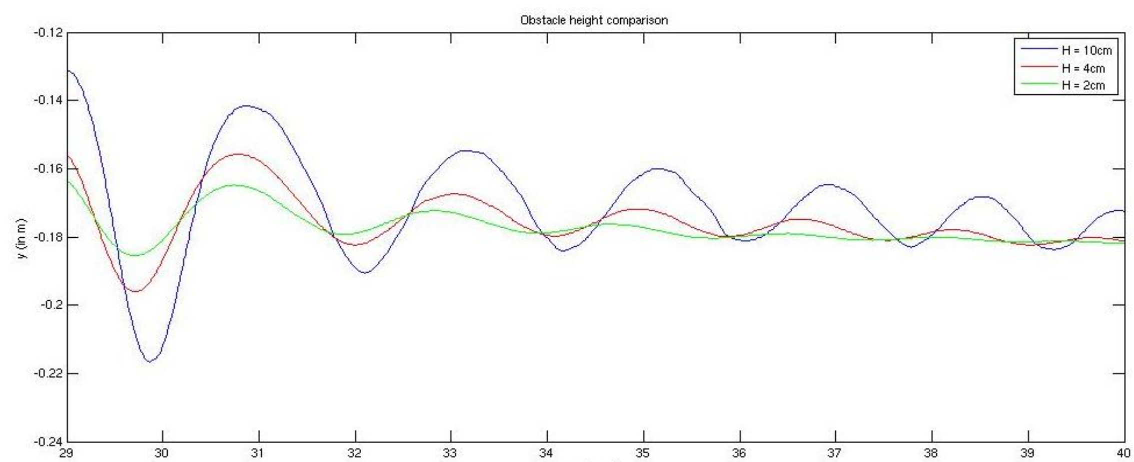

Figure 52. Numerical results for simulation with obstacle height H=10 cm, H=4 cm and H=2 cm.

5.4.4.3 Background flow velocity

Two tests are performed with different background flow velocities (but equal in both layers). From Figure 53a it can be deduced that the wavelength of a stationary lee wave increases as the background flow velocity, U_0, increases.

Another interesting point is the effect of the flow velocity on the downstream boundary condition influence. This reduces significantly for higher flow velocities (Figure 53b). It is assumed that the higher velocities make it harder for the downstream disturbance to travel upstream.

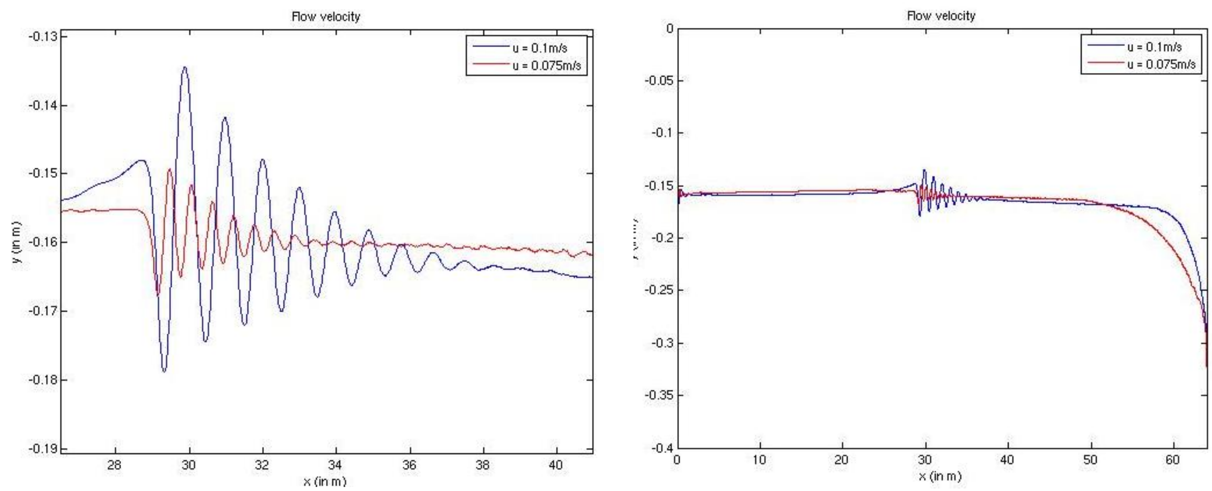

Figure 53. Simulation results for different flow velocities. a) Close-up lee waves. b) Boundary condition influence.

5.4.4.4 Bottom roughness

Three simulations are performed with varying Nikuradse coefficients. As was the case for the tilted tank simulations, larger friction coefficients lead to lower waves that are damped faster.

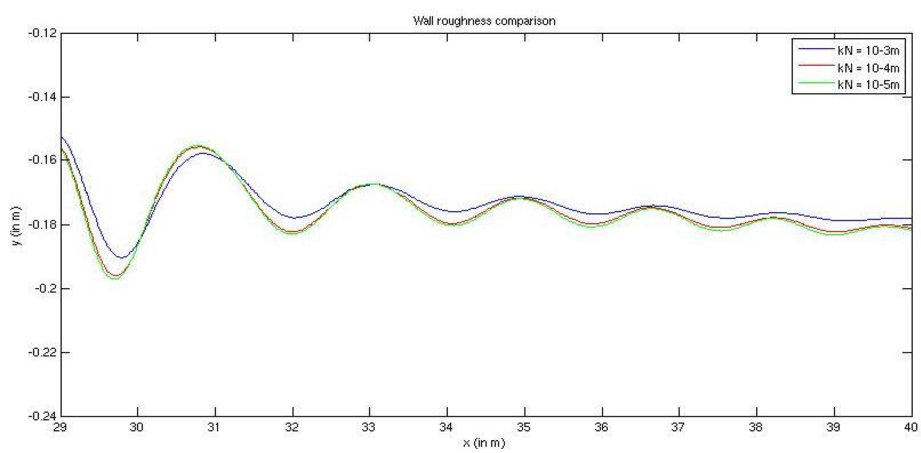

Figure 54. Simulation results for different bottom roughness.

5.4.4.5 Density

Three simulations are performed with different density differences between the two layers. The results are shown in Figure 55.

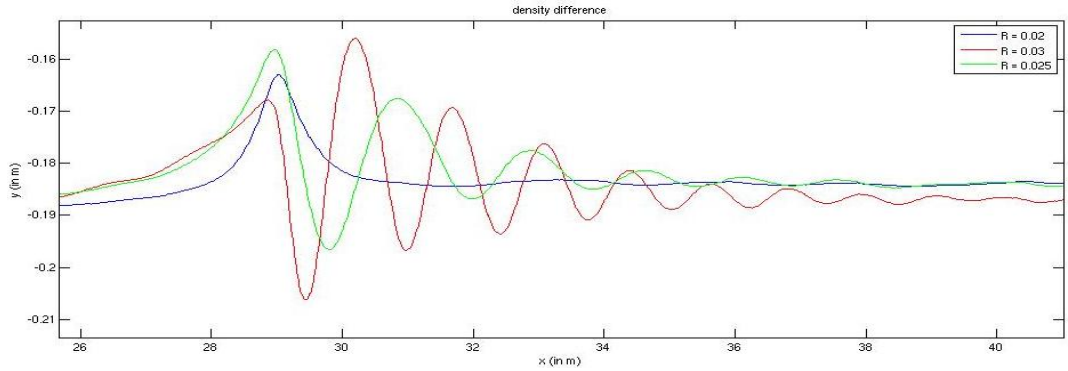

Figure 55. Results for simulations with different density differences R.

Larger density differences lead to higher waves with smaller frequencies. This result is in accordance with the result from the tilted tank experiment.

5.4.5 Conclusion

The following conclusions can be made regarding the numerical simulations of internal lee waves.

A fixed water level boundary is used at the water surface to reduce spin up time. The outflow boundary has upstream influence. The longer the simulation time, the further upstream this disturbance travels. The problem can be delayed by elongating the grid at the downstream end.

Because the computational domain is very long, the grid element size varies over the length of the domain, with the highest density of grid points in the vicinity of the obstacle.

The simulation time of the simulation is long enough for fully evolved lee waves and short enough to prevent the boundary condition at the outflow side of the model influencing the lee wave generation upstream.

The flow behaviour in the numerical simulations is in accordance with the behaviour predicted in the analytical solution.

5.5 Conclusion

The goal of the model validation was to test the capabilities and limitations of the numerical model FINLAB for internal wave situations. The conclusions are summarized below and will provide a useful tool for future simulations in this project.

- **Capabilities**

In general, it can be concluded that FINLAB works well for internal wave tests. The results are consistent with each other, with laboratory tests and with analytical solutions. This makes the model reliable.

By choosing the correct numerical parameters, all the important flow features are captured and errors are reduced to an acceptable limit. A minimum of 100 horizontal elements per wave length, 35 vertical layers and 40 time steps per wave period are recommended for accurate results. A complete list of recommended input parameters can be found in Appendix I.

- **Limitations**

A number of limitations must be taken into account for further simulations.

The number of vertical grid layers is limited to a maximum of 100. This limitation is imposed by the mesh generator. However, simulations with 60-80 vertical layers cause problems with FINLAB. The first few time steps work fine but eventually all calculated values become NaN (not a number).

There are small remaining phase and amplitude errors. This is due to the finite size of the grid elements (the model will always be a representation of the real world).

Small-scale flow features are not always captured. For example the smallest solitary waves at the rear end of a wave packet or the small-scale Kevin-Helmholtz instabilities riding on top of a breaking wave are not represented in the numerical results.

The CPU time has not been a limitation so far. An average simulation took 6-10 hours. However, the next simulations will be on larger grids and longer time scales. Therefore CPU time might become a limiting factor in the next phase of this project.

Chapter 6 – Field data analysis

6.1 Introduction

This chapter provides quantitative information on the occurrence and characteristics of solitons in the Browse Basin. The source of this information is the metocean survey in F-Block commissioned by Shell Development Australia. Measurements were conducted from September 2007 to October 2010 and large solitary internal wave events were observed on several occasions.

This chapter is organized as follows. Section 6.2 gives a description of the measurement strategy. The amplitudes and periods of the observed internal waves are described in section 6.3. In section 6.4 the current speeds are discussed. The vertical structure of current speeds of the waves is described in section 6.5 and the influence of the stratification in the area on the wave activity in section 6.6. In section 6.7, the propagation direction of the waves is treated and section 6.8 describes the correlation between internal wave events and the tidal cycle. The soliton generation mechanisms are discussed in section 6.9 and conclusions are presented in section 6.10.

6.2 Measurement strategy

Three moorings were deployed for the survey: a meteorological buoy, a wave buoy and a current mooring. They were situated at almost the same location approximately 40 km northwest of Browse Island in 250 m water depth. The instruments on the moorings measured current speed and direction, temperature, salinity, sea surface elevation and wind.

- **Meteorological buoy**

The meteorological buoy was equipped with two self contained stations. Each station consisted of sensors measuring wind, barometric pressure, buoy heading, air temperature, water temperature and relative humidity. The stations transmitted hourly one minute mean data via a satellite system.

- **Current meter mooring**

The current meter mooring was a single point mooring with current meters throughout the water column at depths of +1.7 m., +3 m, +30 m, +70 m, +110 m, +150 m, +190 m and +230 m above seabed. The meters also measured sea water temperature. The current meters determined north-south and east-west components of the velocity using orientation information from an internal compass. The velocity was sampled twice per second and averaged over 1-minute intervals. The current mooring further contained five conductivity and temperature (CT) recorders throughout the water column at depths of +60 m, +90 m, +130 m, +170 m and +225 m and a water level recorder located at 1.25 m above seabed. The water level recorder undertook tide measurements by counting the number of oscillations during a fixed period of time and converting them to pressure. Water pressure was sampled at 10-minute intervals. Temperature was sampled at 1-minute intervals.

- **Wave buoy**

The wave buoy was a Directional Waverider Buoy that followed the movement of the water surface and measured its accelerations in three planes: vertical, horizontal north-south and horizontal east-west. By double integration of the accelerations it computed its relative position with respect to the planes. This information was band-averaged in a directional spectrum. The wave buoy derived parameters at a 30-minute interval.

Based on the instrument specifications from the manufacturers (in the Final data report) all current data are considered to have an accuracy of 0.02 ms^{-1} in speed and 5^o in direction. Temperature measurements are considered accurate to within 0.1^oC and tide measurements to within 4 cm.

6.3 Soliton observations

The data showed a number of large, simultaneous sudden changes in current speed and temperature throughout the water column. These observed spike-like features can been identified as solitons. The largest temperature variations occurred in the layer 75 to 200 m above the sea bed. Isotherm displacements up to 50 m were observed. Solitons were observed throughout the year and on average 12-15 large events per year were found in the dataset.

The solitons have various structures and will be categorized in three types. The first type is a 'classic' first order internal wave of depression, see Eq. 3.40. These waves were observed mostly in January, February and June. The waves of depression had maximum amplitudes of 35-50 m near the 22^oC isotherm and wave periods of 20-30 min.

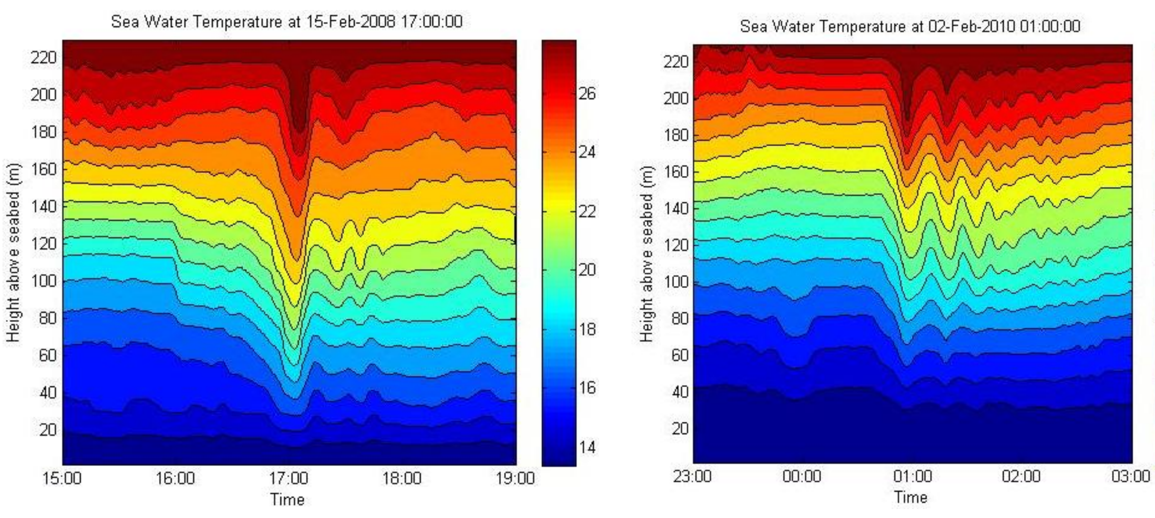

Figure 56. Examples of depression waves.

The depression waves usually arrived in groups (Figure 56). The wave packets were characterized by a steep front, followed by two or three solitons. After the passage of the front and the solitons, the temperature contour lines slowly returned to their initial water depth. This looks very similar to an internal bore.

The second type of waves was observed throughout the year and was a second baroclinic mode soliton. These waves had average amplitudes of 20-40 m and wave periods of 10-20 min. The second mode waves usually had minimum isotherm displacement in the layer 110-130 m above seabed and large displacements above and below that layer. An example is shown in Figure 59.

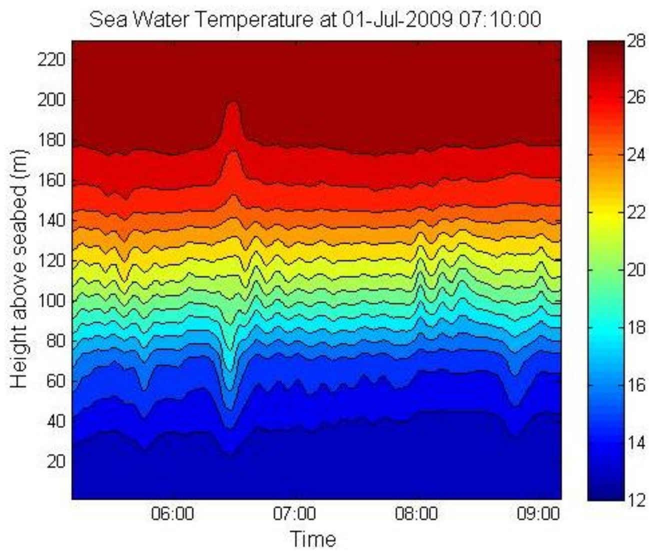

Figure 57. Example of a second mode wave.

The third type of observed waves was an internal elevation wave (Figure 58). Only a small number of this type of wave was observed, mainly in June and December.

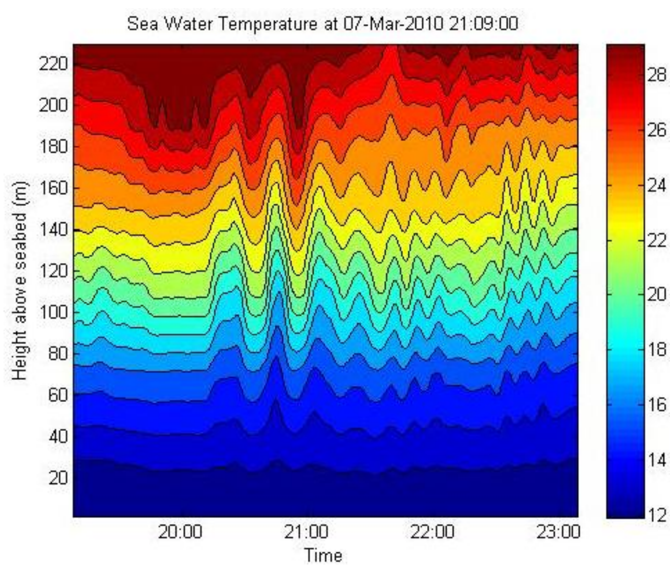

Figure 58. Example of elevation waves.

Most type 1, 2, and 3 waves travelled in groups with the largest wave leading and 2-5 smaller waves trailing behind. More examples of solitons can be found in Appendix II.

Apart from the isolated, large events, some other internal activity was observed. For example, many low amplitude, short period disturbances of both mode 1 and mode 2 were observed throughout the year (Figure 59). Although the isotherm displacements were small, in the order of 10 m, the accompanying current speeds reached 0.55 m/s on several occasions and could last one or two hours. On other occasions, a sudden thickening of the thermocline was observed (Figure 60).

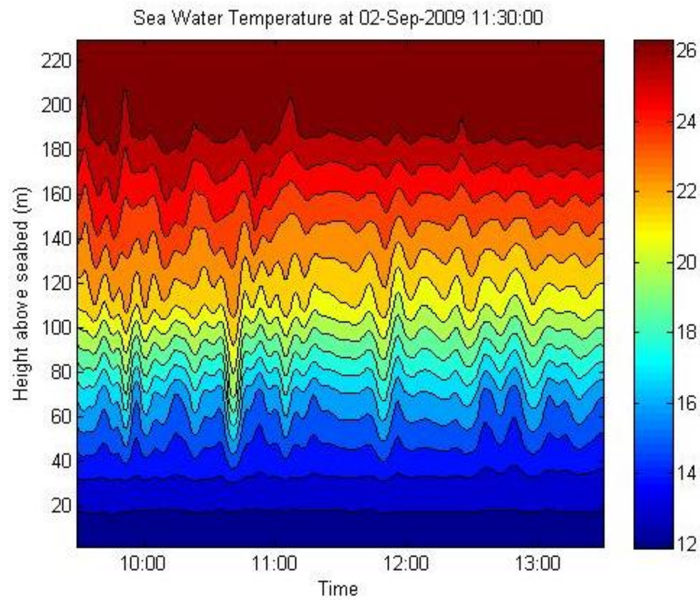

Figure 59. Examples of small internal disturbances.

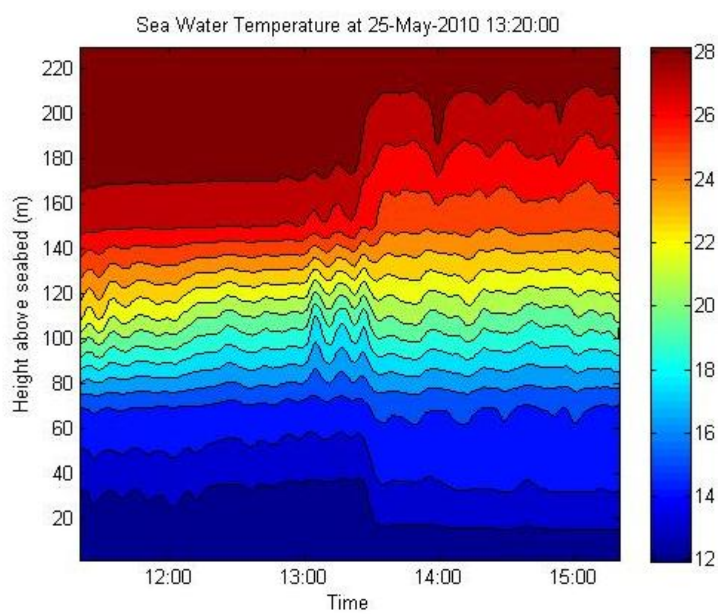

Figure 60. Abrupt thickening of the thermocline.

6.4 Current speeds

The passage of a soliton was characterized by a rapid increase of the current speeds. Higher speeds could persist for 20-30 min. The table below shows the maximum measured current speed at each observation depth.

Water depth (in m)	maximum measured current speed (in m/s)
27	1.107
67	0.943
107	0.866
147	0.868
187	0.806
227	0.902
254	0.782
255.3	0.71

Table 3. Maximum measured current speeds.

Elevation waves push water upwards and depression waves push it down. This results in increased current speeds near the water surface and the sea bed respectively. This is demonstrated for a depression wave. Figure 61 shows the current speed before, during and after the passage of the depression wave. It can be observed that the largest current speed changes occur near the sea bed. The mode 2 waves often showed current speed increases in the thermocline, but they were also observed near the bed and the water surface on many occasions.

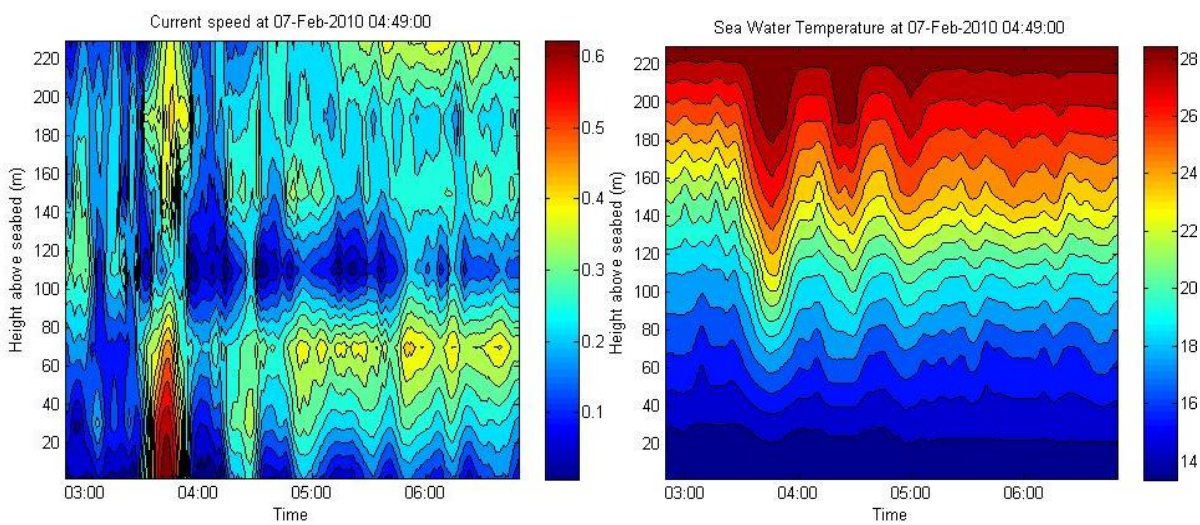

Figure 61. Current speed increase near the sea bed caused by a depression wave.

An elevation wave group passing the mooring on 09 June 2008 consisted of two separate packets of elevation waves travelling 30 min apart. The amplitudes of the first group reached 30-40 m and the current velocity reached 0.7 m/s at 20 m above the sea bed. The northbound and eastbound current velocities are shown in Figure 62. The current velocity near the sea bed is already very high (0.5 m/s) in the hour before the first wave arrives. This is probably because the thermocline is thin but located quite deep in the water column. The flow near the bottom is directed southeast before and in between the soliton passages and reverses during the wave passages. The flow near the water surface is directed northwest and becomes southeast during the passage of the waves. In one hour, the flow reverses five times.

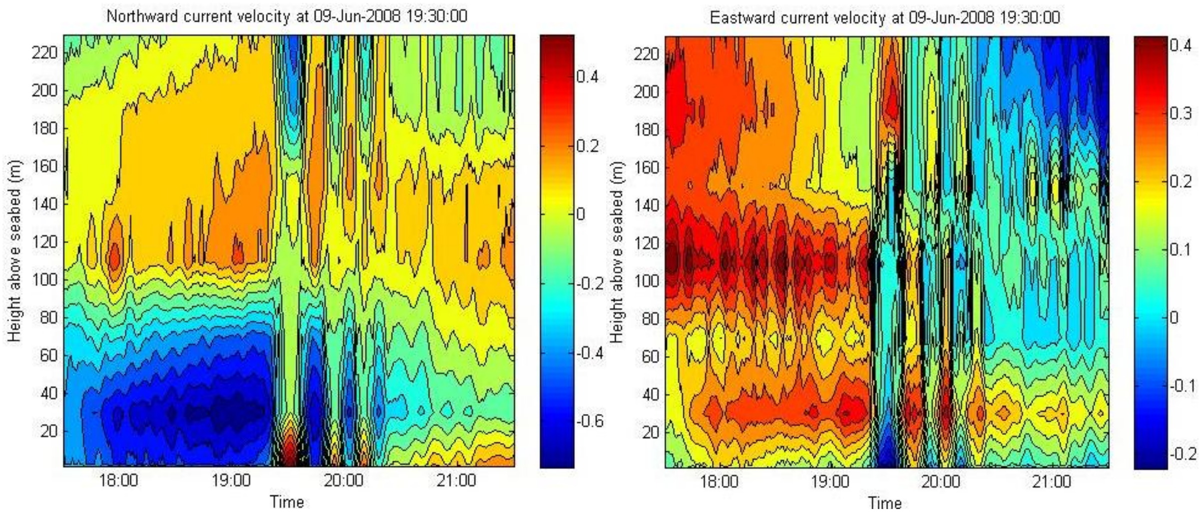

Figure 62. Color contour plots of northward and eastward velocity.

The short, small amplitude waves often showed high current speeds in the upper 100 m of water (Figure 63). An explanation for this combination of high current speeds in the upper layer and small internal wave amplitudes could be wind forcing. Internal wave generation as a result of wind forcing is common in lakes (Boegman et al. 2003). However, the analyzed data show that wind speeds during the passage of this type of internal wave events were not higher than usual. Lagged wind speeds have not been looked into but could be the cause of the high current velocities. In lakes, wind forcing can generate waves with time lags of tens of hours.

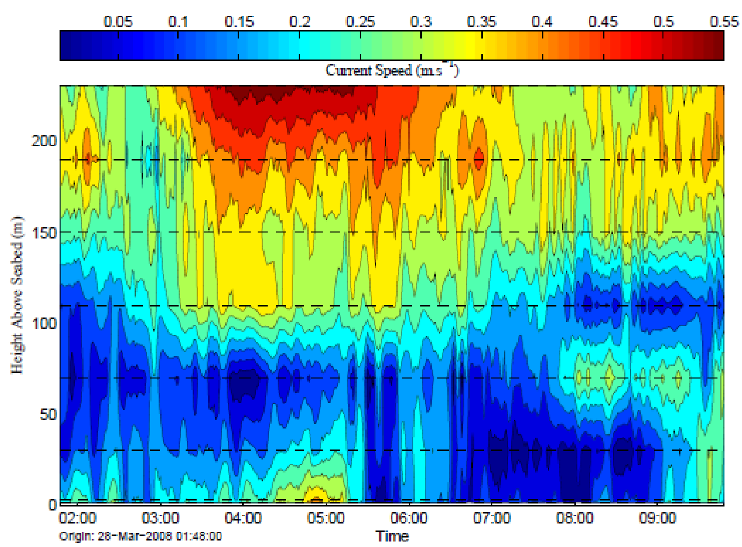

Figure 63. Colour contour plot of current speed for small irregular internal waves.

6.5 Vertical structure

The differences between mode 1 and mode 2 waves are now further studied by taking a closer look at the vertical structure of the horizontal current speeds. Theory (section 3.5.2) suggests first mode waves have one flow reversal in the vertical and second mode waves have two reversals.

Figure 64 shows the horizontal current velocities in northward and eastward direction during the passage of the internal depression wave on 15 February 2008 and two hours earlier. One flow reversal in the northbound direction is observed and two in the eastbound direction.

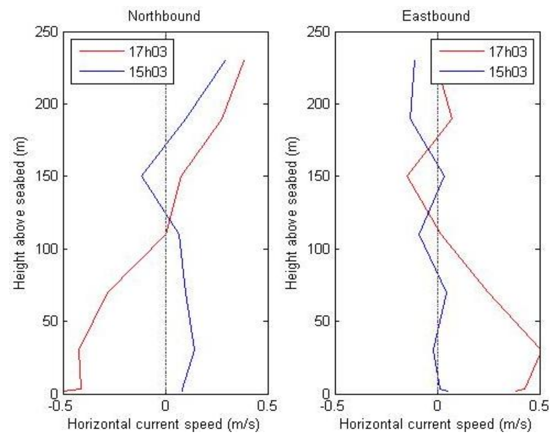

Figure 64. Horizontal current velocities in North and East direction during (red line) and before (blue line) the passage of a depression wave on 15 February 2008.

Figure 65 shows the magnitude and direction of the horizontal current speeds at eight water depths. The depression wave has a pronounced strong current direction (in the lower layers) towards the southeast.

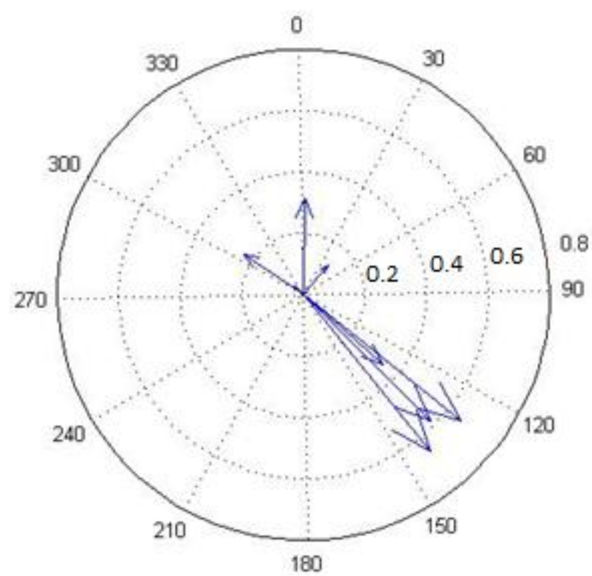

Figure 65. Current velocity direction in 8 water depths during soliton passage on 15 February 2008.

The second mode waves have a different vertical structure. They have two flow reversals in the northward direction. The north-south component of the current speed has a structure that is equal for a majority of the observed second mode waves: in the upper layer the flow direction is south, in the middle layer the flow direction is north and in the lowest layer the flow is once more directed south. However, the east-west component of the mode 2 waves varies. Some waves have a very large component to the west in the upper layer (Figure 66a) while other waves have a large component going towards the east (Figure 66b).

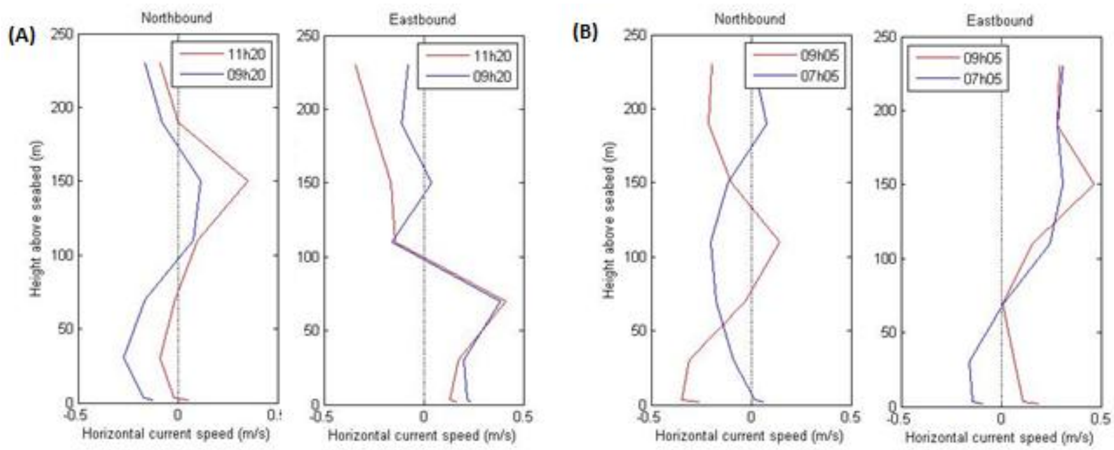

Figure 66. Horizontal northward and eastward current velocities for two different second mode wave events.

Looking at the direction and magnitude at different water depths, it is observed that the mode 2 wave has a far more complex directional structure than the depression wave. That wave had one large component to the southeast. This second mode wave has several large current speeds in three different directions (east, west and north-north-west).

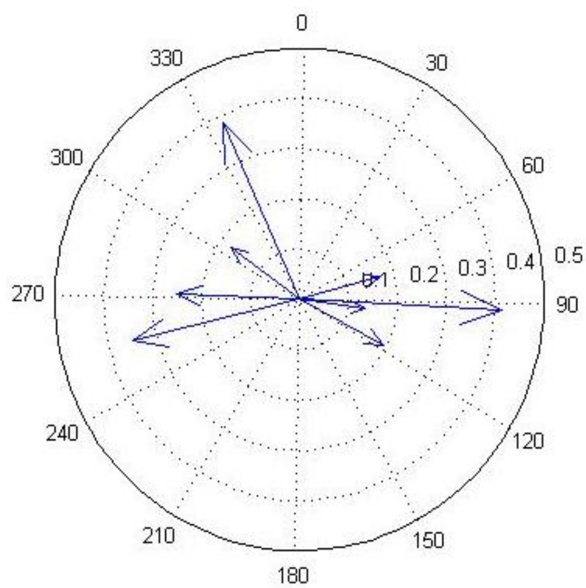

Figure 67. Current velocity direction in 8 water depth during soliton passage on 30 June 2009.

6.6 Stratification

Previous research on the Australian North West Shelf area (Baines 1981; Van Gastel et al. 2009) has shown that large depression waves are dominant during the strongly stratified summer months (December to February) and weaker elevation waves are dominant during the weaker stratified winter months.

This seems only partly the case for the solitary internal waves observed in this survey. Although the large depression waves were mainly observed in December and January, they were also found in June, when stratification is weaker. Elevation waves were also found in both strongly stratified December and the weakly stratified June. The second mode waves were found throughout the whole year. Therefore no strong correlation with the strength of the stratification for this type of waves has been found.

Figure 68 and Figure 69 show examples of strong and weak stratification respectively. The temperature difference between the upper and lower water layer are much larger in January than in June.

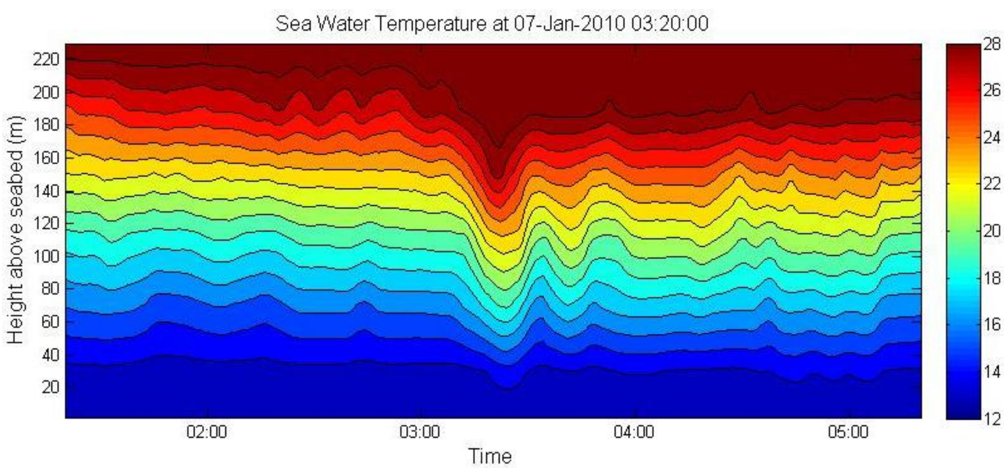

Figure 68. Depression wave in strongly stratified water.

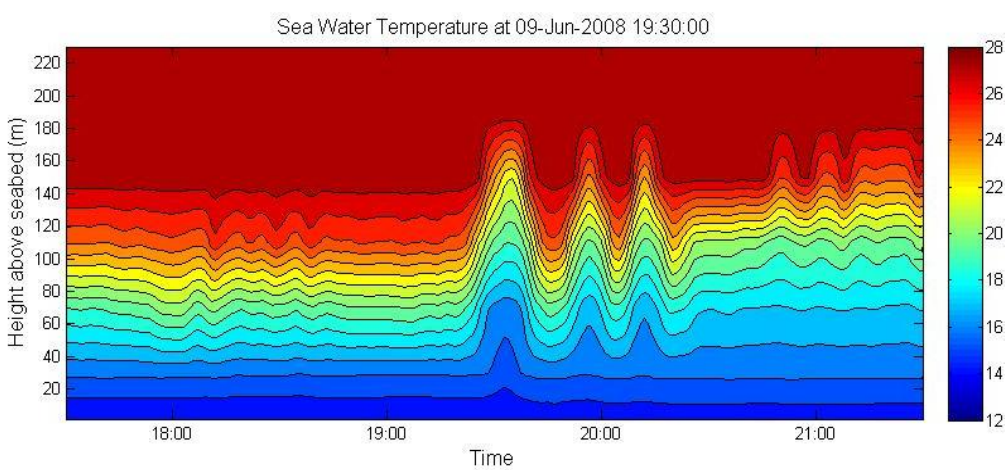

Figure 69. Elevation wave in weakly stratified water.

The occurrence of a soliton not only depends on the strength of the stratification, but also on the thickness and depth of the thermocline. As mentioned in chapter 3, two-layer theory predicts depression waves if the lower water layer is thicker than the upper layer and elevation waves if this is the other way around. Figure 68 and Figure 69 demonstrate that this is also valid in the continuously stratified waters of the Browse Basin. The thermocline in Figure 69 is located much deeper than the thermocline in Figure 68. This can explain the difference between the elevation wave and the depression wave. Figure 69 shows a thick, completely mixed upper layer and a continuously stratified lower layer. However, in Figure 68 the mixed upper layer is much thinner. Mode 2 waves can theoretically only occur in continuously stratified waters. Figure 59 shows that, in accordance with the wave theory, the mode 2 wave is strictly confined to the thermocline.

6.7 Wave direction

As expected (see section 6.4), the depression waves all show a large increase in the current speed in the lower layers and a smaller increase in the current speed in the upper water layers. The direction of the current speed in the lower layers is south-eastward and in the upper layers it is north-westward. The direction of the current near the surface gives an indication of the wave direction (Hyder et al. 2005). Depression waves therefore seem to travel towards the north-west. The second mode waves appear to be travelling south-east, so towards the coast.

6.8 Tidal cycle

Many researchers have studied the relation between tidal amplitude and soliton occurrence. Results are different in different areas. Solitons occurred only on spring tide in the Andaman Sea (Hyder et al. 2005) and the Bay of Biscay (New and Da Silva 2002). On the other hand (Yang et al. 2004) found depression waves in the northern South China Sea occurring mainly at neap tide. A field study near the North Rankin platform on the Australian North West Shelf (Bluteau et al. 2010) showed that sudden isotherm displacements generally occurred just before high tide during the spring tides. However, strong currents were found during the neap tides as well as the spring tides.

The tidal elevations before and after the occurrence of 10 depression waves (Figure 70) and 10 second mode waves (Figure 71) are compared. Apart from three exceptions (in this selection, there might be more in the entire data set) all waves arrive in the 7 days after spring tide. More than half occur around neap tide or in the two days before. No difference is found between first mode and second mode waves regarding this aspect. These results differ from the previous observations near North Rankin by (Bluteau et al. 2010).

It can also be observed that almost all depression waves occur during high tide. Second mode waves were observed at both high tide and low tide, as well as in between when the sea surface elevation is minimal. The amplitudes of spring tides preceding the solitons are calculated for 10 depression waves and 10 second mode waves. The amplitudes of the spring tides preceding the occurrence of depression waves range from 3.8 m to 5 m. There is more variation in the range of spring tidal amplitudes preceding second mode waves: 3.3 m to 5.2 m.

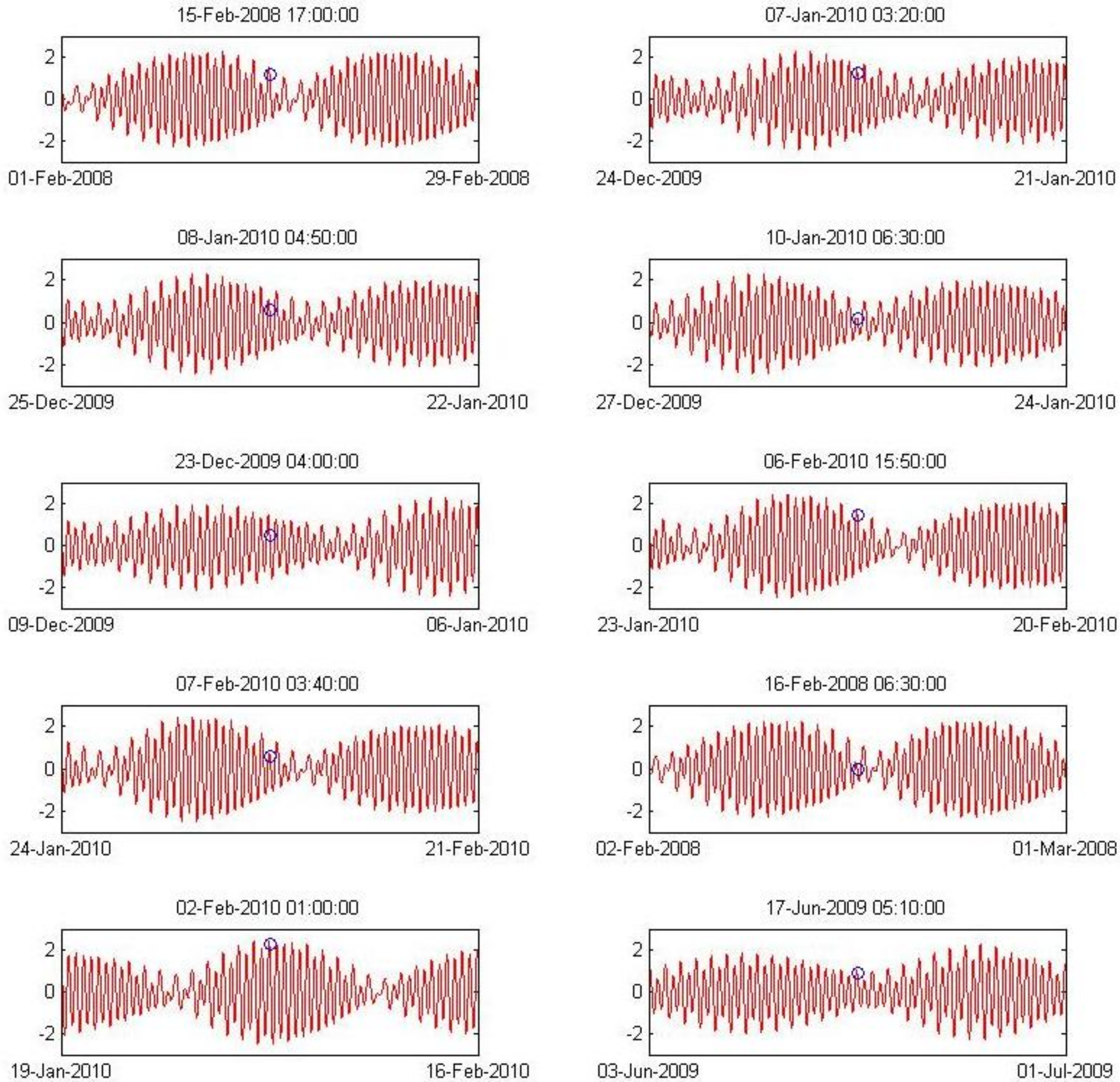

Figure 70. Sea surface elevation (red line) and wave of depression (blue circle).

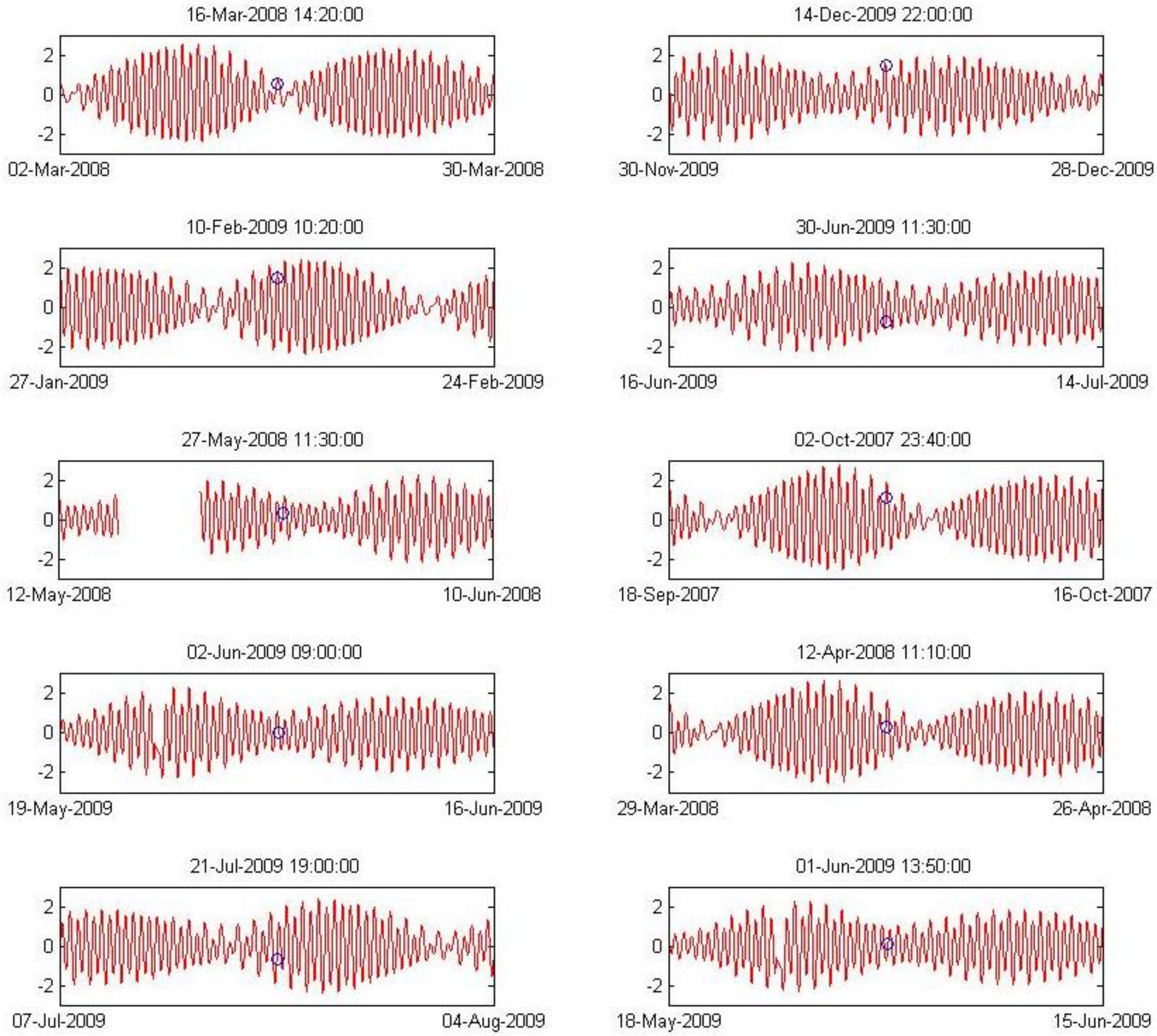

Figure 71. Sea surface elevation (red line) and second mode waves (blue circles).

6.9 Discussion on generation mechanism

In order to numerically simulate the internal waves in the Browse Basin, it is important to understand how the waves are generated because this will influence the initial conditions in the model simulations. Although it is not possible to make conclusions, the likelihood of the lee wave or the tide-topography generation mechanisms being the relevant process is considered.

In section 6.3 it was mentioned that a number of waves show characteristics of an internal bore. The analysis of the Browse Basin sea floor topography in chapter 2 further showed that there are no isolated sills or narrow inlets in the Browse Basin. However, there are several reefs about 150 km west of the future FLNG location that rise steeply from the deep ocean.

Section 6.5 showed the complex directional structure of the waves. It is not the same for every wave and this suggests that three-dimensional effects play an important role. These can only be introduced by the irregular and complex sea floor topography in the Browse Basin.

The solitons showed a broad range of shapes, modes and tidal cycle connections and had a three-dimensional character. It is assumed that tide-topography interaction generates the solitons in the Browse Basin but that there are several generation areas and many influencing factors apart from tidal forcing.

6.10 Conclusions

Some 12 to 15 large internal solitary waves were observed at the mooring per year. They have amplitudes of 25-40 m, wave periods of 15-30 min and current speeds reached 0.7 m/s. Smaller waves occurred more often. The solitons were most often second modes waves, depression waves were also found and elevation waves were only observed on a few occasions. The depression waves generally arrived at high tide, the second mode waves did not have a clear correlation with the tidal cycle. The dominant wave direction seems to be south-east (for the mode two waves) and the generation mechanism is assumed to be the interaction between the shelf break and the tidal motions.

Chapter 7 – Numerical simulations of the Browse Basin

7.1 Introduction

The validation tests in chapter 5 have shown that Finlab is capable of simulating internal waves. Modelling criteria were presented for reliable results with acceptable accuracy. The data analysis described in chapter 6 has given better insight into the characteristics of the observed solitons in the Browse Basin. However, these chapters also raised a number of questions. While Finlab performed very well in the comparison with the laboratory tests, high resolution grids and small times steps are required to resolve solitons. Here an investigation is carried out into whether or not such high resolution can be obtained for Browse Basin-scale simulations without becoming too computationally expensive. The exact generation location of the solitons in the Browse Basin is unknown and it is therefore not known beforehand what size domain or bathymetry is required in order to simulate the solitons.

As a first step, a simple closed-boundary test is performed to find appropriate grid resolution and time steps for the Browse Basin simulations. This test is also used to verify that the continuous stratification from the field data can support the generation and propagation of short internal waves in the numerical simulations. Initial conditions based on the tilting tank experiment in Section 5.2 are used as this is a proven means to generate internal solitary-like waves. When the right combination of stratification and numerical settings is found, longer domains are modelled and open boundary conditions are introduced in the numerical set up. This is done as a step towards introducing tides into the model and to gain a better understanding of how tidal forcing can be simulated with Finlab.

The goal of this section is to find the appropriate numerical settings (resolution, time step, length of numerical domain, boundary conditions) in order to simulate internal solitary waves in Browse Basin using Finlab. In this chapter more realistic bathymetry, stratification and tidal forcing conditions are used.

In Section 7.2 the stratification, time steps and grid resolution for basin scale simulations are considered. In Section 7.3 more realistic simulations are then carried out. In Section 7.3.2 the numerical set up for the shelf simulations is established. In section 7.3.3 the results of the numerical tests are shown, first for simulations with M2 tidal boundary conditions, then for other tidal components and finally the results of simulations with different tidal velocities are presented. In section 7.4.5 the results are analyzed and conclusions are presented in section 7.3.5. Scott Reef and surroundings are studied next. In section 7.4.2 previous studies of internal wave dynamics near the Reef are summarized and results of simulations with Finlab are shown in section 7.4.4 and analyzed in 7.4.5. General conclusions are presented in section 7.5.

7.2 From laboratory scale to Browse Basin scale

7.2.1 Introduction

As mentioned in the previous section, a transition must be made from laboratory scale domains (tens of meters) to Browse Basin scale domains (hundreds of kilometres).

In this section, this transition is made by combining the findings from chapters 5 and 6 into suitable input conditions for Finlab in a first attempt to model internal waves in the Browse Basin. More complex and realistic three-dimensional tests can be done at a later stage, based on the results from this first series of tests.

7.2.2 Numerical set up

The distance from the flat sea bed in the deep ocean to the Prelude location is over 500 km. Due to the limitations imposed by the mesh generator (limited number of nodes) and the expected long computational time for running simulations on such a large grid with the required high grid resolution, it is decided to take three short sections of 5200 m of the shelf and experiment with initial conditions. Figure 72 shows the three sections of the shelf that are modelled. Section 1 has a slope of 0.2%, section 2 has a slope of 1.2% and section 3 has a slope of 2.0%. Water depths range from 250 m to 1200 m.

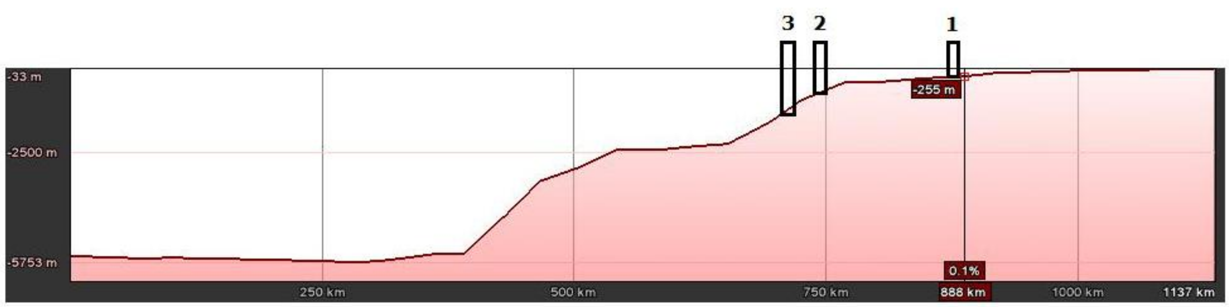

Figure 72. Shelf break sections.

To capture solitons with acceptable accuracy, 100 horizontal grid elements, 35 vertical layers and 50 time steps per wave period are necessary (see chapter 5). The observed solitons in the Browse Basin have wave periods of 20-25 min (see chapter 6). Wave speeds are unknown, but values of 0.5 to 1 m/s are not uncommon (Apel 2002). The solitons in the Browse Basin can then be assumed to have wavelengths of 1200-3000 m. From this it follows that a horizontal grid element size of 12-30 m and a time step of 25-30 s are required.

In chapter 5 it was demonstrated that the angle of tilt of the interface determines the magnitude of the waves. It is yet unknown what angle of slope must be used to generate waves with magnitudes in the order of the observed waves, therefore a grid resolution is chosen to ensure that generated short waves will be captured. In the simulations, a horizontal grid element size of 10 m and a time step of 10 s are chosen. 75 vertical layers will be used for the next set of simulations. This higher number is chosen because the ratio of wave amplitude over water depth is smaller in the Browse Basin than in the tilted tank experiments. The simulation time is 4 hours.

Instead of the two-layer fluid, a continuously stratified fluid will now be used as the initial condition. The density profile is based on the field data profiles. The stratification is chosen that was measured on 15 February 2008, two hours before the occurrence of a large soliton (Figure 73). As stratification was measured at only 8 points in the water column, a best fit approximation (tangent hyperbolic function) is used to find a continuous mathematical function that can be used in Finlab. There is no information available on the stratification in the ocean further offshore and therefore it is assumed that the thermocline profile measured in 250 m water depth is the same as in deeper water. This is probably not the case in reality.

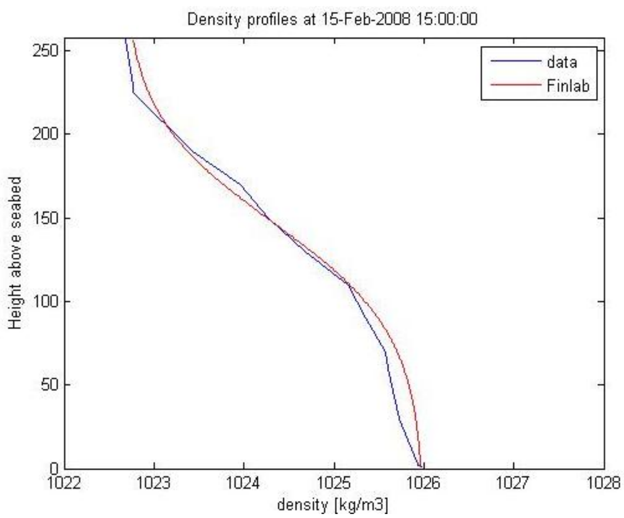

$$c = \tanh\left(-0.015 \cdot (water\ depth + 110)\right)$$

With a relative density transport variable R=0.001642.

Figure 73. Fitting of tanh-profile (red line) to measured density profile (blue line connects the 8 data points).

Four closed boundaries (partial slip, k_N=1.10^{-4} m) will be used and an initial tilting thermocline is posed on the computational domain to generate the internal waves. Various angles of tilt are tested to find one that generates internal waves with amplitudes 20-50 m.

The set of numerical parameters that worked well for the tilted tank simulations will be used for these simulations as well (except the parameters discussed in this section). See Appendix I for a complete list.

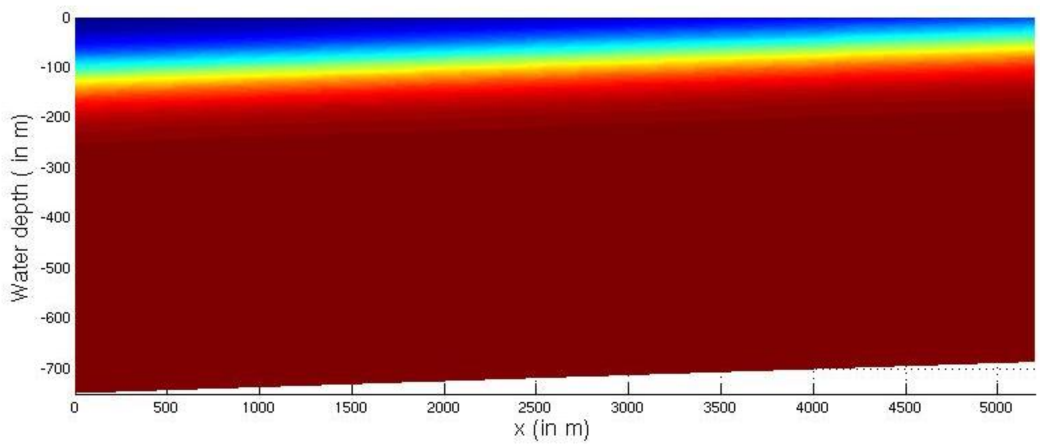

Figure 74. Numerical set up for shelf section 2.

7.2.3 Results

The results of the numerical simulations show the generation of internal solitary waves. The waves are compared to the measured soliton on 15 February 2008. Figure 75 shows the result for shelf break grid 2. Only the upper 230 m of water are shown as this is the layer where waves occur. Both plots have a time slot of 4 hours. The results of the simulations on the other cross-sections, simulations with different angles of tilt and different stratification can be found in appendix III.

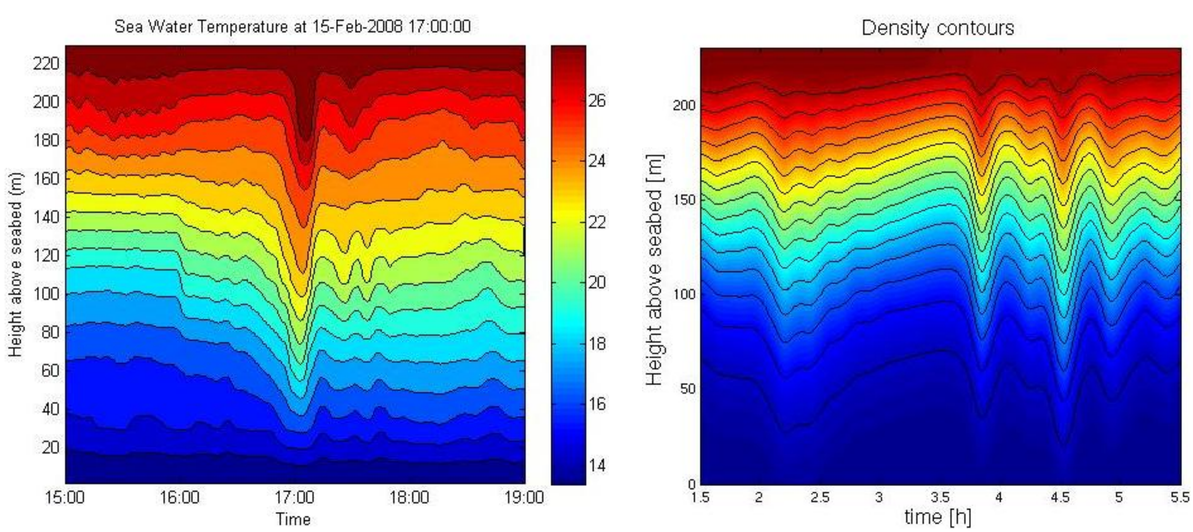

Figure 75. Comparison between soliton observed in field data and computed soliton.

7.2.4 Analysis

In Figure 75, the computed solitons have amplitudes in the order of 30 m and wave periods of 20 min. Similar values are observed in the field data. Variations of the water depth and the sea floor slope have a large influence on the magnitude of the generated waves (see appendix III). The results show that Finlab can simulate the solitons in a more realistic large-scale test case. It also shows that the current forcing conditions provide enough energy to the system to generate more realistic results. However, as expected there are substantial differences between the measured and modelled soliton. The field data shows temperature contours that are displaced downwards in the half hour before the soliton arrives. In contrast, the density contours of the computed soliton are displaced upwards before the wave arrives. This is caused by the reflection of the basin-scale wave at the closed boundary. The solitons are generated only after the initial long wave has reflected at the wall. This is not a realistic mechanism in the Browse Basin and therefore simulations are presented in the next section with more realistic open boundary conditions. These simulations are carried out in order to explore the role of tidal forcing in the generation of solitons in the Browse Basin.

7.2.5 Conclusions

The numerical tests with closed boundaries have shown that the resolution and time step work well and that the stratification supports the generation and propagation of solitary internal waves. The results further demonstrate the significant influence of water depth and sea floor slope. Simulations using longer domains and with open boundaries (tidal conditions) are now set up based on these conclusions.

7.3 Shelf break simulations

7.3.1 Introduction

Based on the findings from the previous tests, a more realistic test is now set up. Longer domains are modelled and open boundaries with tidal forcing will be tested as it was shown in chapter 5 that tidal currents play a large role in the generation of internal waves.

7.3.2 Numerical set up

Figure 76 shows a transect through the Browse Basin. This section will be modelled. The bathymetry is found in Google Earth and based on data from GEBCO (General Bathymetric Chart of the Ocean). This is a bathymetric grid at 30 arc-second intervals (approximately 1 km).

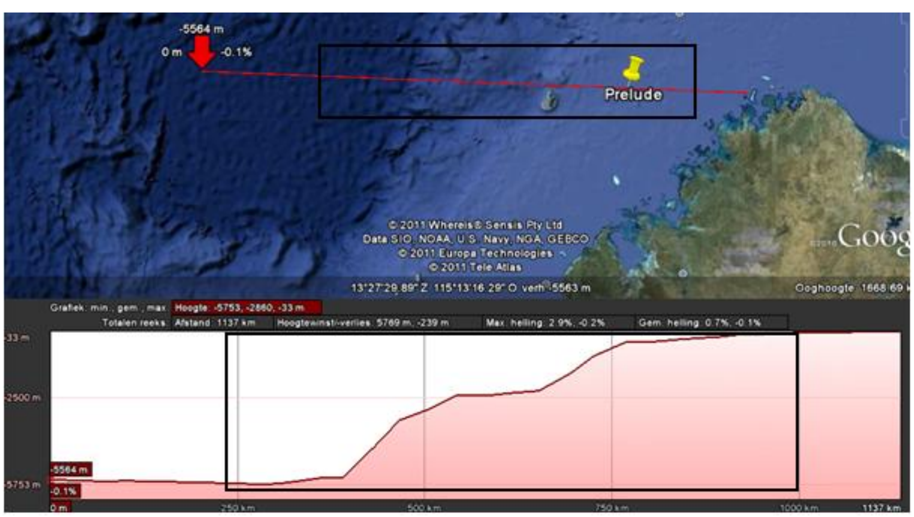

Figure 76. Cross-section of shelf with numerical domain (black rectangle). (Source: Google Earth)

The goal is to model the whole shelf. This results in a numerical domain of 700 km with water depths ranging from 5800 m to 100 m. The same grid generator as before, Sepran, is used to make the grid. A vertical resolution is chosen of 15 m in the upper 300 m of water and 50-350 m in the deeper layers. A horizontal resolution is chosen of 2000 m in the deep ocean and 67 m around the inner shelf break. The resolution in each part of the grid is shown in Figure 76. A higher resolution is impossible with this grid generator because Sepran has a limit of 70,000 grid points. The resolution is coarser than stated necessary for accurate results in the previous section but might be just fine enough to roughly capture the generation of solitary waves. The limitation of the grid generator is also the reason that the eastern boundary lies at 100 m water depth and not further shoreward.

Figure 77 shows the resolution in each part of the mesh of the shelf. With the mesh generator Sepran, a mesh can be subdivided into surfaces of different size and shape. On each side of each surface, a number of grid points can be imposed. Figure 77 shows the subdivision of the shelf mesh into smaller surfaces and the resolution on each line segment. The numbers in the figure indicate the distance between two grid points (horizontal distance for horizontal lines and vertical distance for vertical lines).

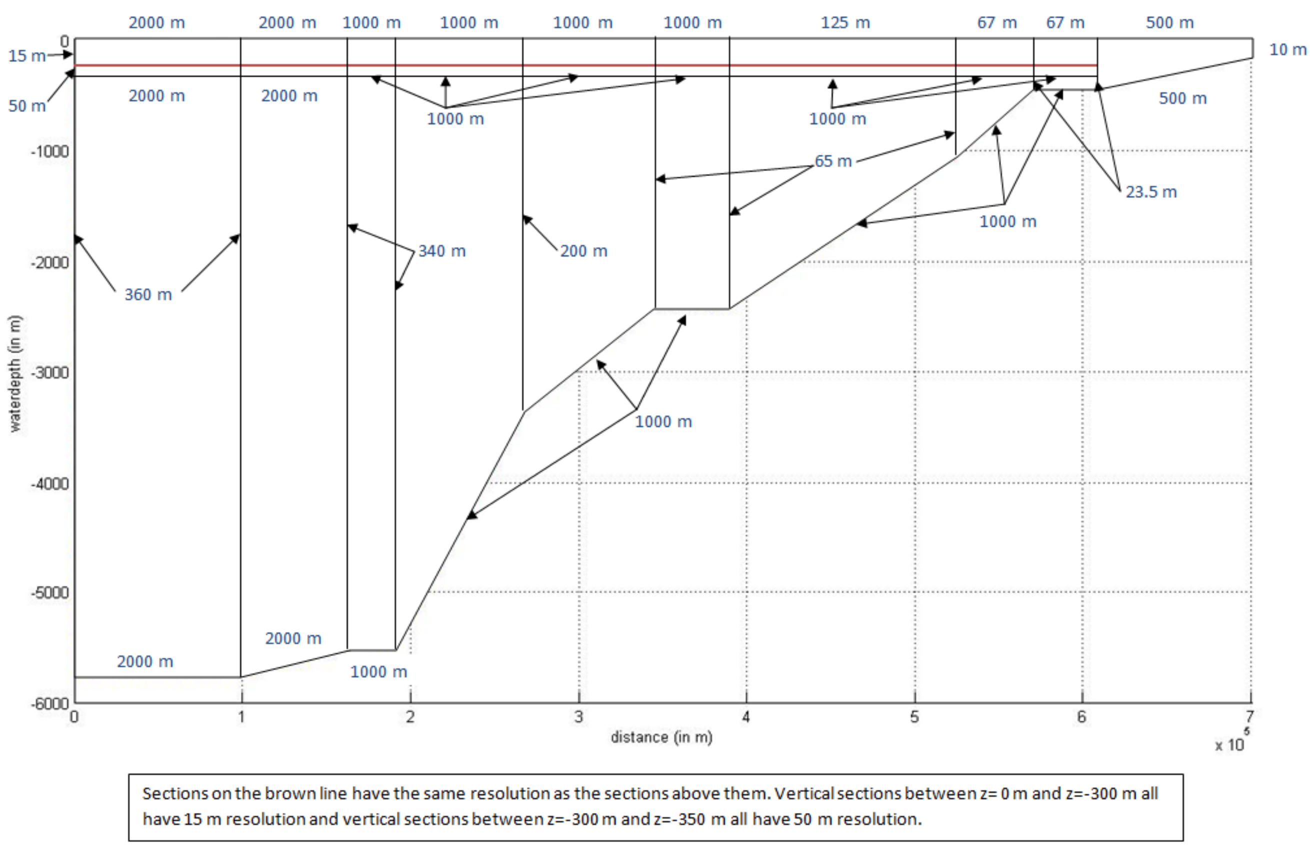

Figure 77. Mesh resolution.

On the western boundary, a fluctuating velocity condition is posed, as well as a fluctuating water level. The M2 tidal component is dominant in the Browse Basin, but the S2, K1 and O1 tidal components were also measured (Holloway 1994). Each component will be simulated in a different run. The tidal components, their periods and the run numbers are summarized in Table 4. The velocity and the water level boundary conditions with the M2 tidal frequency are illustrated in Figure 78. Sea surface elevation measurements from the field data showed that the spring tidal amplitude of the water surface fluctuation is 4 m. This is taken as a first guess for boundary conditions. The velocity condition (for the M2 tidal component) is:

$$u = a\sqrt{\frac{g}{d}} \cdot \sin\left(\frac{2\pi t}{12h25\,\mathrm{m}}\right)$$

In this equation, *u* is the horizontal tidal velocity, *a* is the amplitude of the sea surface, *g* is the gravitational acceleration, *d* is the water depth and 12h25min is the M_2 tidal period. Measured current speeds in the hours before the passage of a soliton in the field data often showed values of 0.1 to 0.4 m/s at the measurement location in 250 m water depth. Therefore a value of 0.25 m/s is taken as a first guess. An iterative process can be used to find out what boundary conditions must be set to get the correct tidal conditions in 250 m water depth. The influence of the Coriolis force is neglected. This assumption will be discussed in chapter 8.

Run	Tidal component	Description	Period
1	M2	Principal lunar	12.25
2	S2	Principal solar	12.00
3	K1	Luni-solar diurnal	23.93
4	O1	Principal lunar diurnal	25.82

Table 4. Tidal components.

The ocean bottom is represented by a closed wall boundary with a Nikuradse wall roughness of 10^{-1} m. There is a free moving water surface. Although unrealistic, the eastern boundary is closed. A Riemann boundary was not possible because it does not absorb internal waves. A fixed water level made the simulations crash, it is assumed that a fluctuating water level on one side and a fixed water level on the other side of the numerical domain is not a good combination. A more natural boundary would be to extend the simulation to the coast, which would eventually end in a very shallow area and a closed boundary would be justified. However, due to the mesh generator limit it was not possible to make this grid extension. Another option is to use a flow relaxation scheme but this was not possible within the time frame of this project. The eastern boundary is therefore closed and it must be assumed that reflecting waves will negatively influence the results.

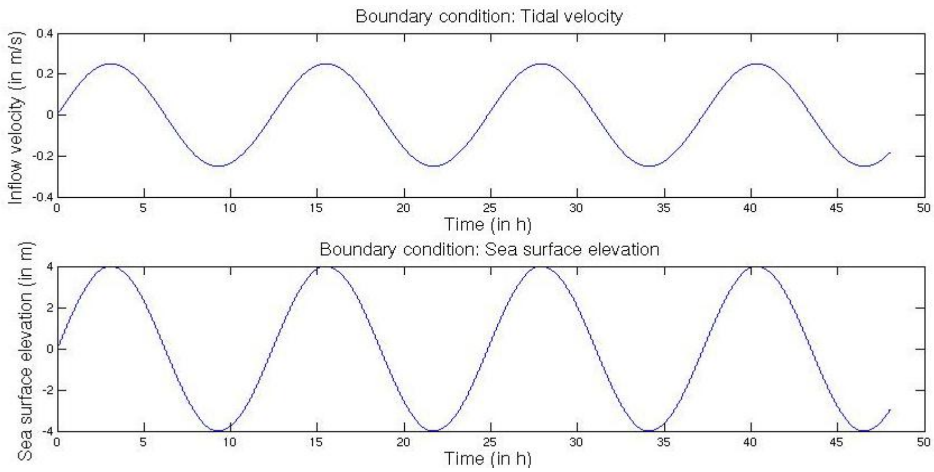

Figure 78. Boundary conditions at left boundary.

A time step of 100 s will be used. This is more than 25 s, as was calculated in the previous section. However, chapter 5 showed that the time step has much less influence than the grid resolution and this time step will shorten the computational time enormously. This is considered more important at this stage of the simulations especially since the resolution is too coarse for accurate results anyway.

The stratification in the domain is continuous and the density profile is again based on the measurements on 15 February 2008 (profile extracted from Shell Field Data, see Figure 79). As there is no information on the stratification in the deeper water depth, the water layers below 250 m water depth are considered non-stratified. This assumption will be discussed in chapter 8.

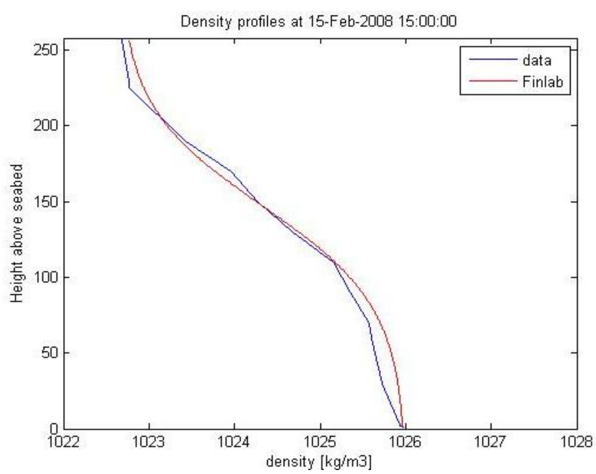

Figure 79. Density profile as initial condition for Finlab.

Figure 80 shows the bathymetry and the initial stratification for the simulation.

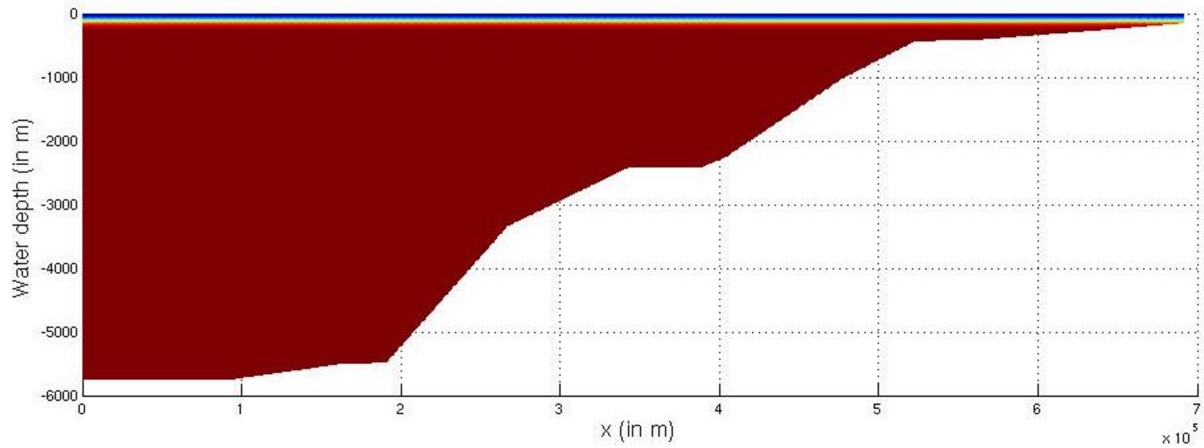

Figure 80. Simulation of entire shelf area at t=0 s.

7.3.3 Results

The modelled time is 72 hours, the CPU time approximately 72 hours. The numerical results show the generation of an internal tide (Figure 81 and Figure 82). The internal tide is very weak in the deep water area but becomes more pronounced in shallower water. It can also be observed that the internal tide decreases in amplitude in the shallow water after the shelf break. It reaches amplitudes of 20 m just left of the shelf break at x = 520 km. The shelf break influences the flow. Water seems to partly reflect and travel back in the opposite direction, and partly continue onwards up the slope. As expected, the closed boundary at the eastern side of the domain reflects incoming tidal waves. No solitons are observed.

Figure 82 also shows deepening of the thermocline. It is assumed that this is caused by numerical diffusion because the grid is very coarse in that area (2000 m horizontal interval and 15 m vertical interval).

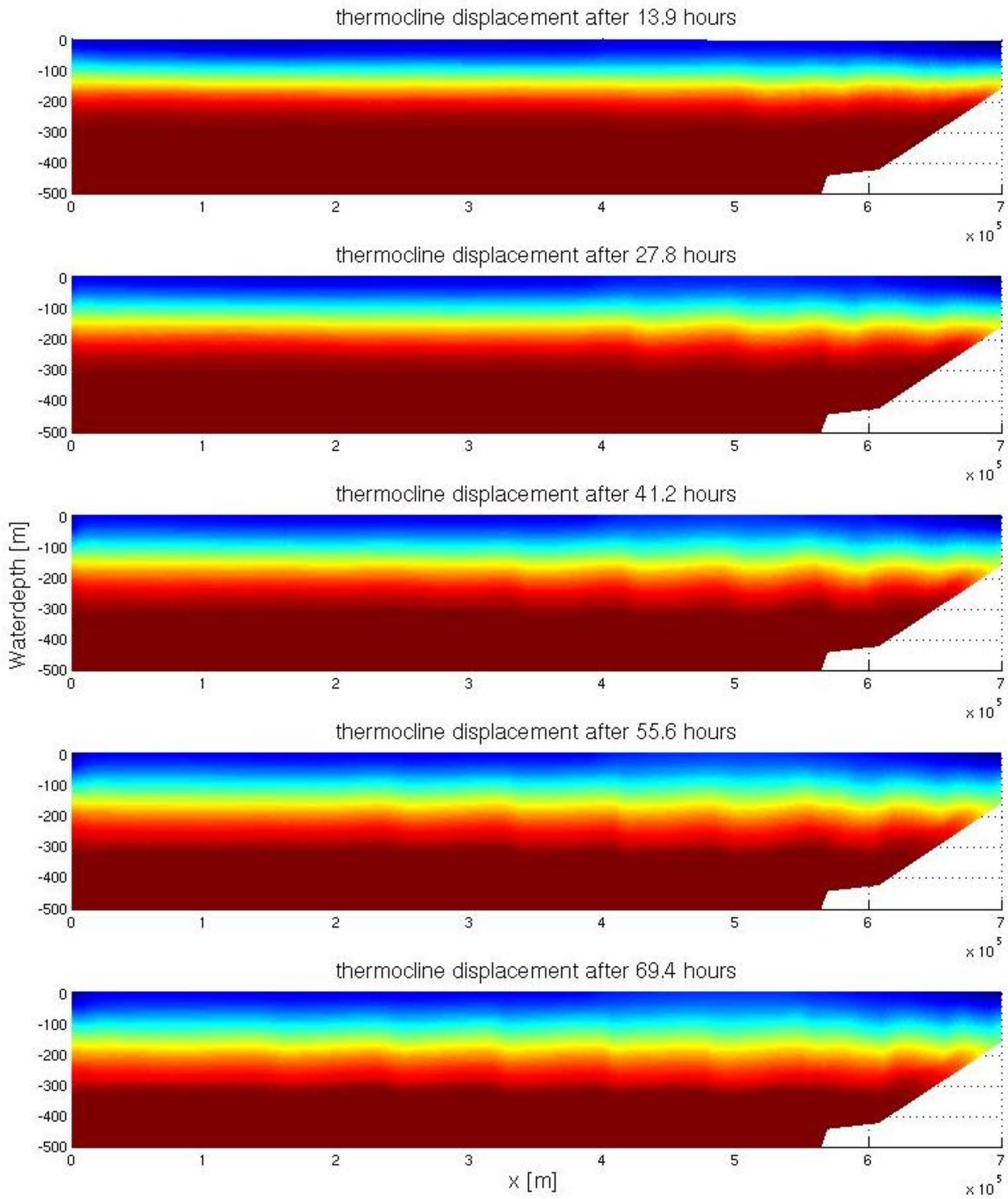

Figure 81. Thermocline displacement on the shelf at different times.

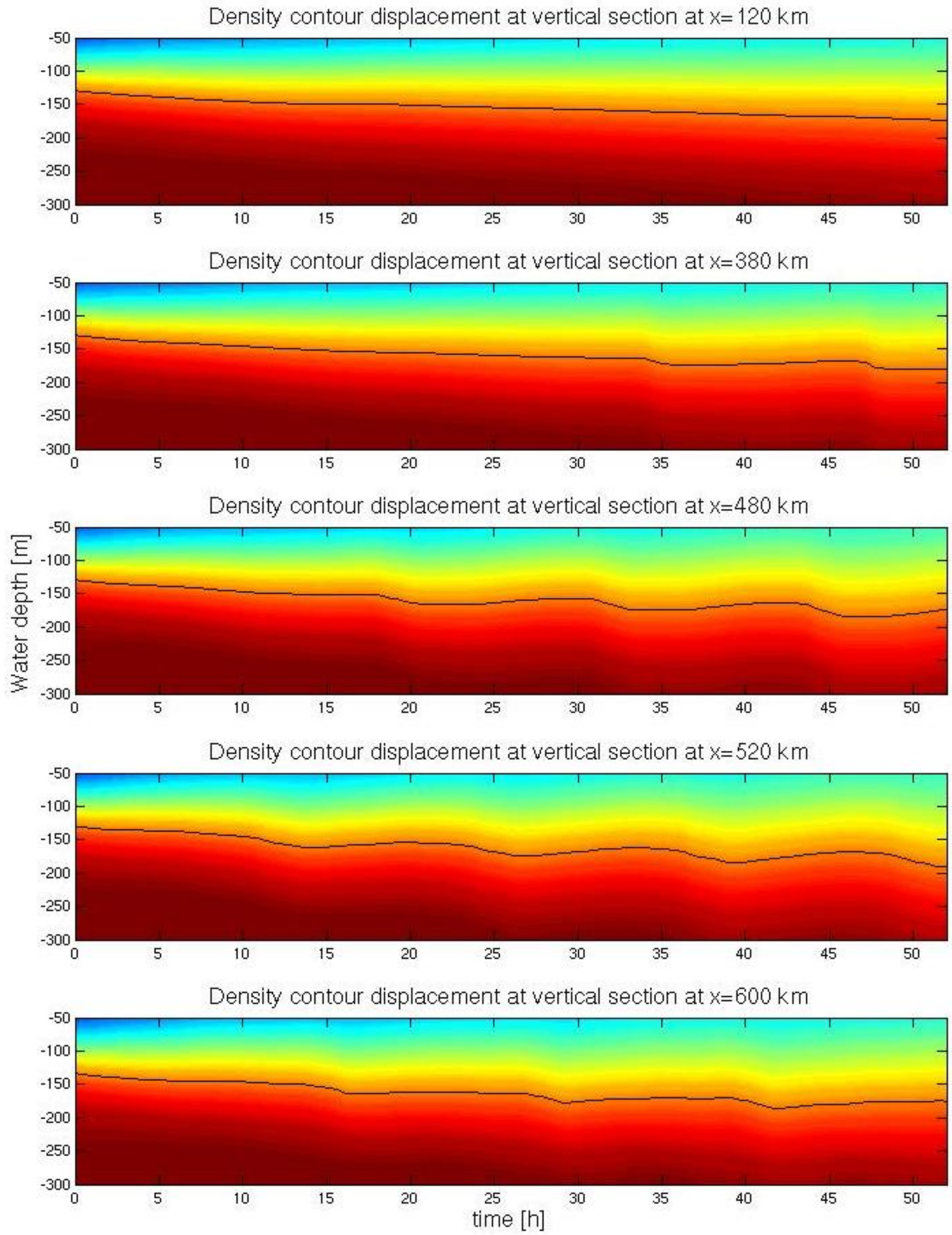

Figure 82. Displacement of the pycnocline for a vertical cross-section at 5 different locations on the shelf.

Varying the tidal component shows internal tides with different periods in the simulation results. This is in accordance with theory. The results for run 2 and run 4 are shown in Figure 83 and Figure 84.

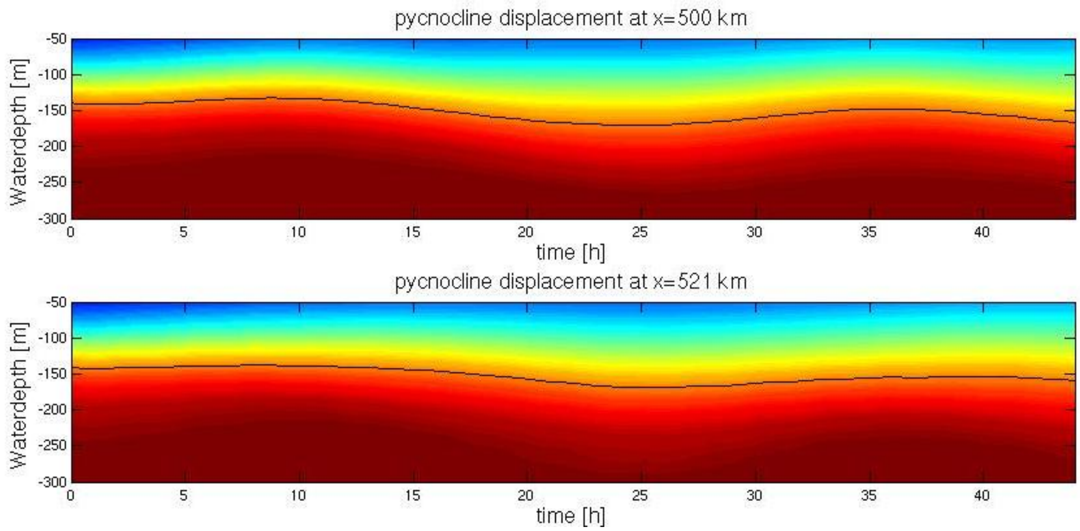

Figure 83. Results for simulation with tidal component O1 (run 4).

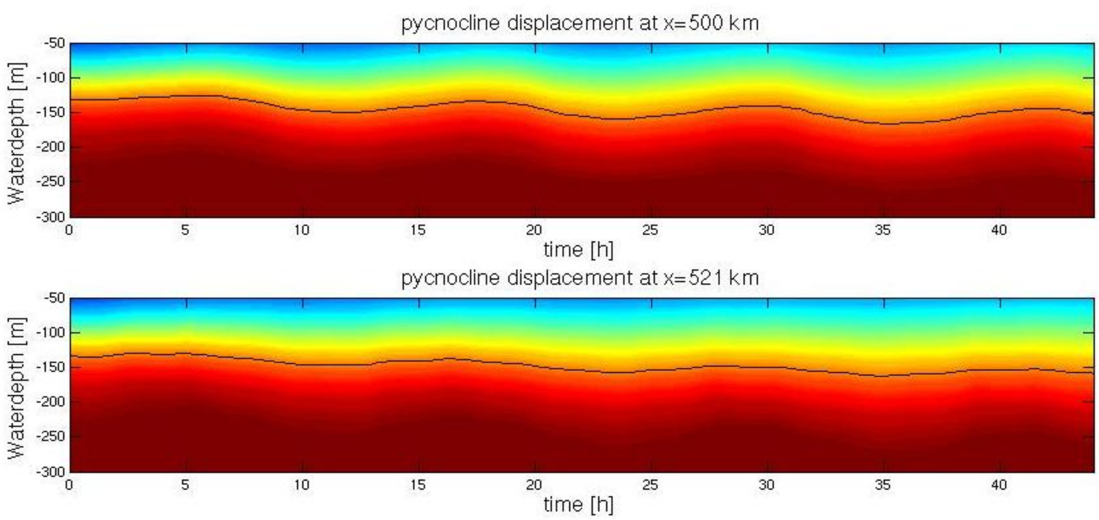

Figure 84. Results for simulation with tidal component S2 (run 2).

As mentioned in the section 7.3.1, current velocities depend on the water depth and will change when flow travels from deep to shallow water. Velocities at the shelf break are important for correct results and therefore simulations with different inflow velocities are set up. The chosen boundary conditions and the resulting maximum horizontal velocities on the shelf are summarized in Table 5.

Velocity at inflow boundary	Velocity at x = 360 km	Velocity at x = 520 km
0.1 m/s	0.15 m/s	0.4 m/s
0.25 m/s	0.35 m/s	0.9 m/s
0.3 m/s	0.4 m/s	1 m/s
0.5 m/s	0.6 m/s	1.8 m/s

Table 5. Maximum inflow velocities and resulting maximum velocities on the shelf.

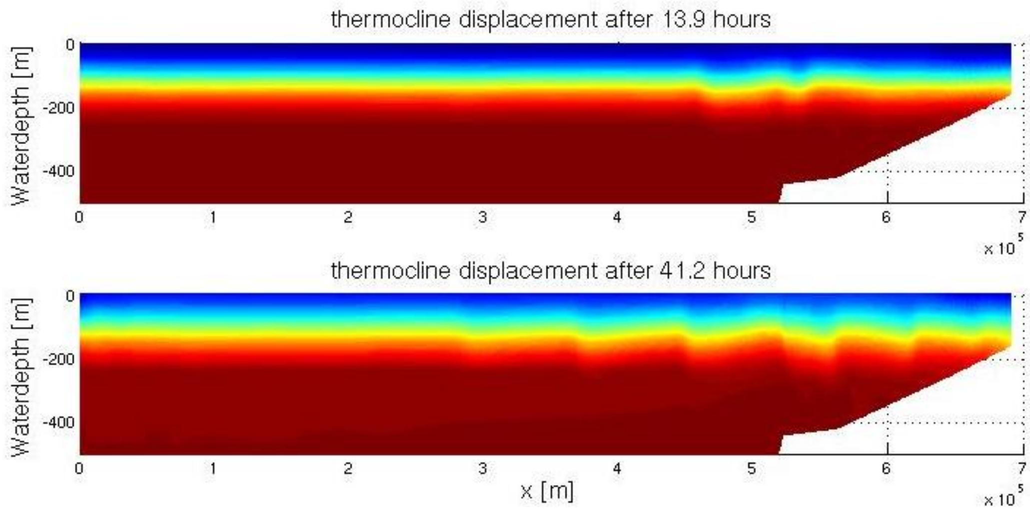

Figure 85. Thermocline displacement on the shelf at different times for inflow velocity = 0.25 m/s for M2 tidal frequency.

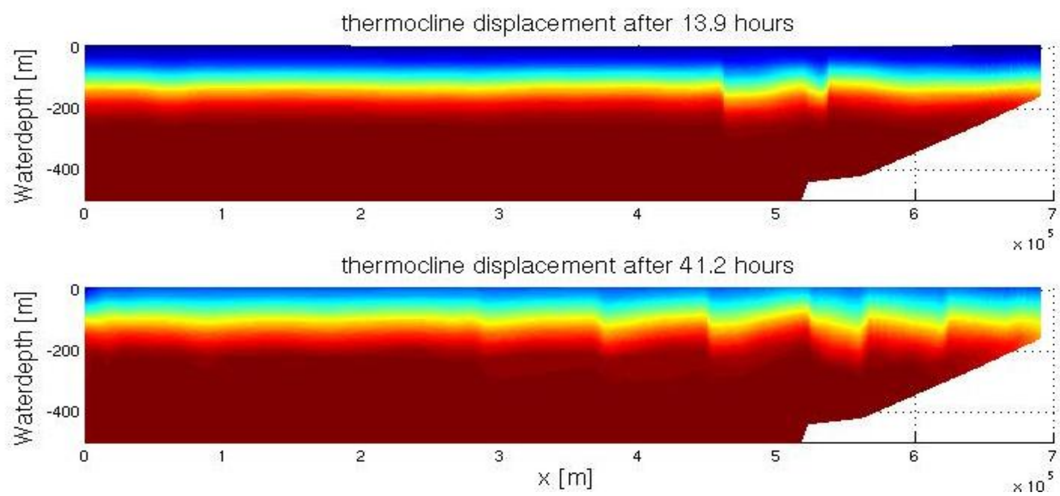

Figure 86. Thermocline displacement on the shelf at different times for inflow velocity = 0.5 m/s for M2 tidal frequency.

The results show that the internal tides have higher amplitudes for simulations with higher velocities. No differences in the tidal period and no solitons are observed.

A smaller time step of 30 s did not give different results.

7.3.4 Analysis

The simulation results show the generation of an internal tide and the steepening of this tide as it propagates towards the shore. However, solitons are not generated. Tests with a smaller time step and different tidal velocities do not show solitons either. Time step and velocity are therefore ruled out as possible problems at this point. It is most likely that the grid resolution is too coarse to show solitons in the simulation results. However, due to the limitation in the number of grid elements imposed by the mesh generator, it is not possible to verify this with Finlab.

7.3.5 Conclusion and recommendations

Before summing up the conclusions, it must be mentioned that the last simulations were a challenge for a number of reasons. The mesh generator was a critical limiting factor and became a problem. This must be solved for any further simulations of the shelf. The computational time was also very long: computations took up to 72 hours. Finally, there was not much information available about detailed bathymetry or the stratification, tidal currents and sea surface elevation in the deeper ocean and the soliton generation site.

Keeping this in mind, it can be concluded that the simulations show internal tides but no solitons. This is most likely due to the coarse resolution of the grid. The following recommendations are made to improve the grid:

- Use another mesh generator that has no limit on the number of grid elements.
- Extend the grid on the shallow water side. Alternatively use a flow relaxation scheme on the eastern boundary. The closed boundary causes reflecting waves that influence the flow in deeper water. The FLNG facility is located in 250 m water depth and with the current grid, the boundary is too close to this location and reflecting waves give unrealistic results.
- As it is not possible within the timeframe of this project to switch to another grid generator, it is decided to focus instead on simulations on smaller domains. That way, higher grid resolutions can be used. In the next section, these simulations are described and discussed.

7.4 Scott Reef simulations

7.4.1 Introduction

Some 150 km west of Prelude are Scott and Seringapatam Reefs. They are located on the edge of the continental shelf and rise very steeply from the sea floor on the western side.

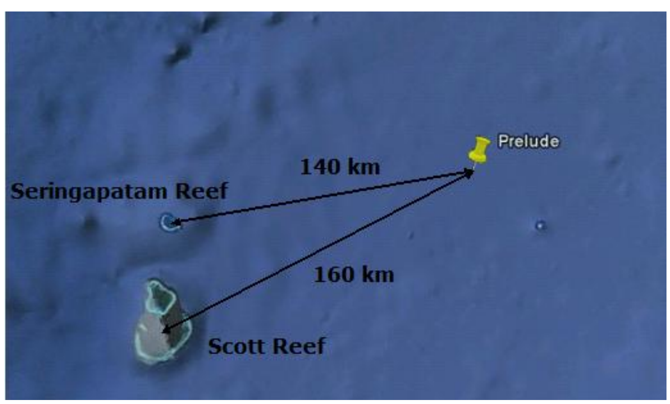

Figure 87. Scott and Seringapatam Reefs near Prelude.

Scott Reef comprises three formations: North Reef, South Reef and Sandy Hook Inlet. North and South Reef are separated by a channel of 2-4 km width and a depth of 500 m. The reefs only emerge at low tide. Seringapatam Reef is located approximately 23 km north of North Scott Reef.

Similar to the surrounding area, semi-diurnal tides are dominant near Scott Reef with a spring tide of 4 m and a neap tide of 1 m.

Figure 88. Location of Scott Reef.

Scott Reef has been the subject of a few field and numerical studies (Wolanski and Deleersnijder 1998; Rayson 2006; Costin 2010) and has been identified as a potential generation site for internal waves. The aims and results from those studies will be summarized in the next section.

Scott Reef is located at a short distance from the Prelude location and has slopes that are much steeper than the shelf break that was modelled previously. It is therefore a good area to model and simulate with Finlab. However, it must be kept in mind that the reefs are very three-dimensional and that simulating them in two dimensions will exclude many important three-dimensional effects.

After discussing the results and issues of the previous studies and the numerical simulations of Scott Reef with Finlab in the next sections, the results of Finlab and the previous studies will be related to each other in chapter 8.

7.4.2 Previous Scott Reef studies

A field study around Scott Reef by Wolanski and Deleersnijder (1998) has revealed the presence of internal waves with amplitudes of 60 m, mainly at semi-diurnal frequencies. Their current and temperature time series also showed large fluctuations at higher, non-tidal frequencies. Internal waves of semi-diurnal frequency were often out-of-phase on opposite sides of the reef.

Wolanski and Deleersnijder further used a two-dimensional, non-linear model to investigate the propagation of internal waves around the reef. They used idealized bathymetry so that the reef was modelled as a cone rising from the ocean floor. The radius of the numerical domain was 120 km. The stratification was modelled as a two-layer system with a constant density in each layer. The model was forced by the surface tide along the circular boundary of the model domain, with appropriate spatial lags in order to simulate the tidal ellipses in the open ocean.

The numerical study has suggested that the waves are generated locally by internal tide/topography interaction and rotate counter-clockwise around the emerging reef. Free internal waves at higher frequencies were found to propagate freely away from the reef.

The aim of Rayson's study in 2006 was to present a three-dimensional hydrodynamic model of Scott Reef and its surroundings that can replicate the dominant oceanographic processes in the region. The model used in Rayson's study is the Regional Ocean Modelling System (ROMS model). It is a three-dimensional, primitive equation, hydrostatic model. The horizontal grid of the model is defined by orthogonal curvilinear coordinates as opposed to the finite-element triangular coordinates used with Finlab. The vertical coordinates are defined by a sigma-coordinate system. ROMS had a free surface boundary layer that allowed inclusion of the effects of tides. The pressure gradient was solved using the hydrostatic approximation. This means that non-hydrostatic processes could not be solved with ROMS.

The vertical sigma-coordinate system caused pressure gradient issues and in combination with the steep slopes of the Reef, ROMS became unstable. The steep bathymetry required significant smoothing to stabilise the model solution. The introduction of tides and boundary conditions into the three-dimensional domain also caused problems. The interaction between bottom topography and tidal flow introduced wave steepening. The amplitude of the waves was further increased due to numerical round-off errors. As a result, the simulation results became unbounded and the model crashed.

The aim of Costin's study (2010) was to gain a better understanding of the physical processes occurring at Scott Reef. He analyzed field data in detail, using various time series and statistical oceanographic data analysis methods, for example digital filtering, spectral analysis and cross-correlation. The focus of the study was on the physical properties of the water column, circulation within South Scott Lagoon and the dynamics of the exchange with external waters.

Large temperature fluctuations were observed and propagated from the South Scott Channel towards the lagoon itself in the form of an internal bore. The amplitude of the temperature fluctuations varied with the spring/neap tidal cycle, as well as with seasonal changes in the water column. The deep waters around Scott Reef had a mixed upper layer of 50 m and strong stratification in the remainder of the column in March. The thickness of the mixed layer increased to 80 m in June. Within the (shallow) lagoon itself, the water column was stratified in March and became mixed down to half the water depth in June. A mixed layer thickness of 100 m was observed in August. Internal waves occurred at the Western Channel of South Scott Lagoon, but not the eastern. Spectral results showed that the internal waves are generated by barotropic tides. Internal wave energy of mode one and two was observed in March and June.

7.4.3 Numerical set up

The bathymetry near Scott Reef is idealized (based again on the GEBCO data set) and this results in numerical domains of 350-500 km with a steep slope on the west side of the reef and water depths ranging from almost 2000 m to 100 m. Around Scott Reef, a vertical resolution of 10 m and a horizontal resolution of 50 m is used. The resolution of the other parts is 100 m in the vertical and 1000 m in the horizontal direction. This is the finest resolution that can be achieved with the Sepran mesh generator.

The initial conditions, boundary conditions and density distribution are the same as for the shelf break simulations (section 7.3.1). This means that there is a vertical density gradient in the layer 50-200 m below sea surface and the water column below is assumed to be non-stratified. There is no horizontal density gradient. Wolanski and Deleersnijder (1998) state that the upper 300 m of water around Scott Reef are temperature-controlled. They found that horizontal gradients were negligible near Scott Reef but large at the continental shelf edge.

In this situation, the thermocline is intersected by Scott Reef. It is expected that this bathymetry will block the flow and force it around the reef. This has been studied by Wolanski and Deleersnijder (1998). This three-dimensional effect cannot be simulated in a two-dimensional simulation. It is therefore important to find a bathymetry that permits tidal flow moving over the Reef. This bathymetry is found in a cross-section of the outer edge of the Scott Reef. The top of the reef there is located 300 m under the water surface and no longer intersects with the thermocline. Two other cross-sections are used that are located north and south of Seringapatam Reef. The locations of the cross-sections are shown in Figure 89. All four situations are tested for the same set of initial and boundary conditions.

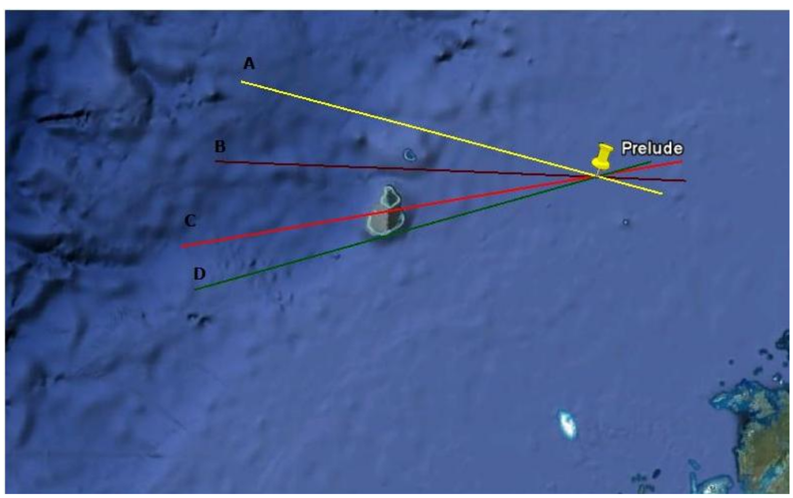

Figure 89. Cross-sections near Scott Reef. (Source: Google Maps)

Figure 92, Figure 90, Figure 91 and Figure 93 show the bathymetries and stratification cross-sections A, B, C and D. The resolution of the cross-section A grid is shown in Figure 94. The other three grids have a similar resolution.

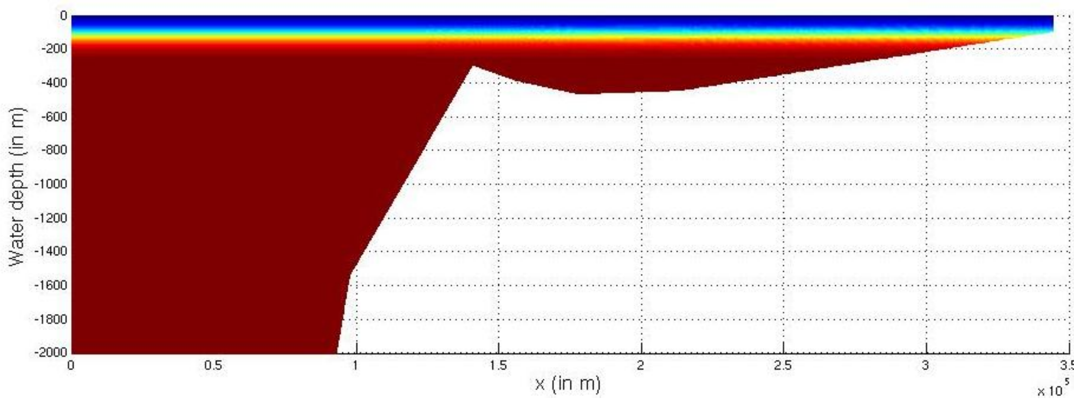

Figure 90. Cross-section A.

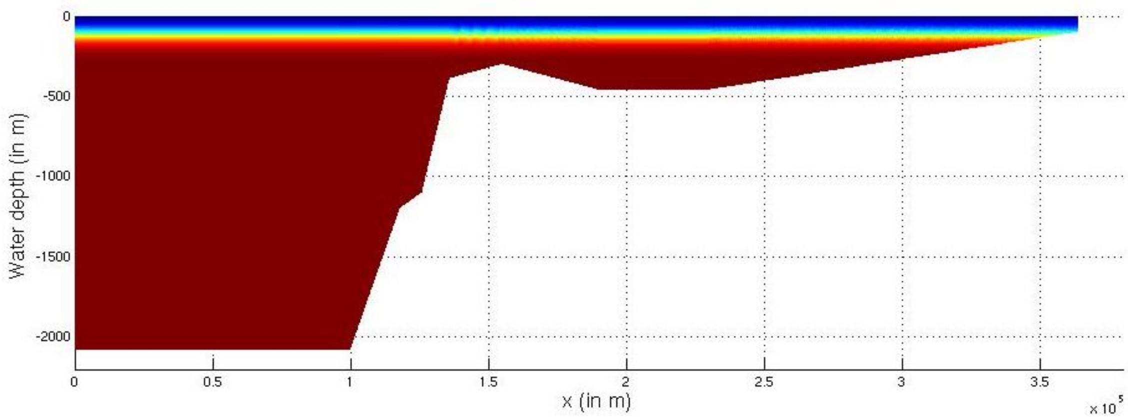

Figure 91. Cross-section B.

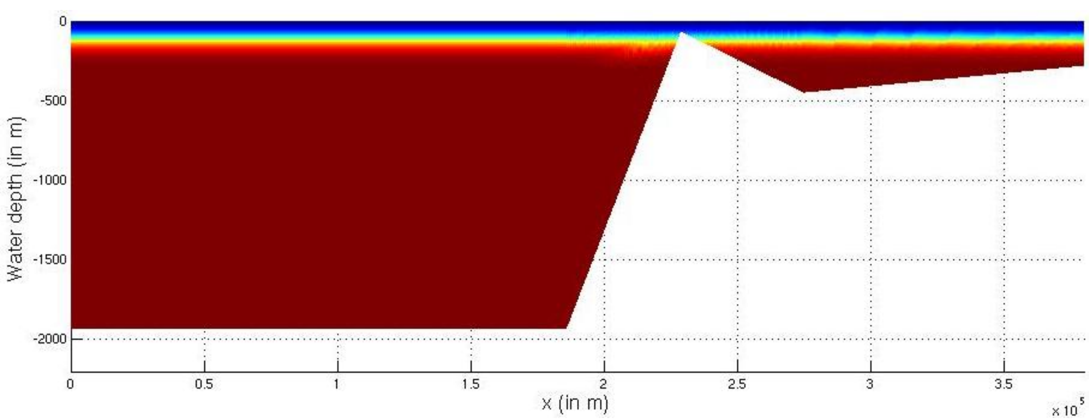

Figure 92. Cross-section of Scott Reef (cross-section C).

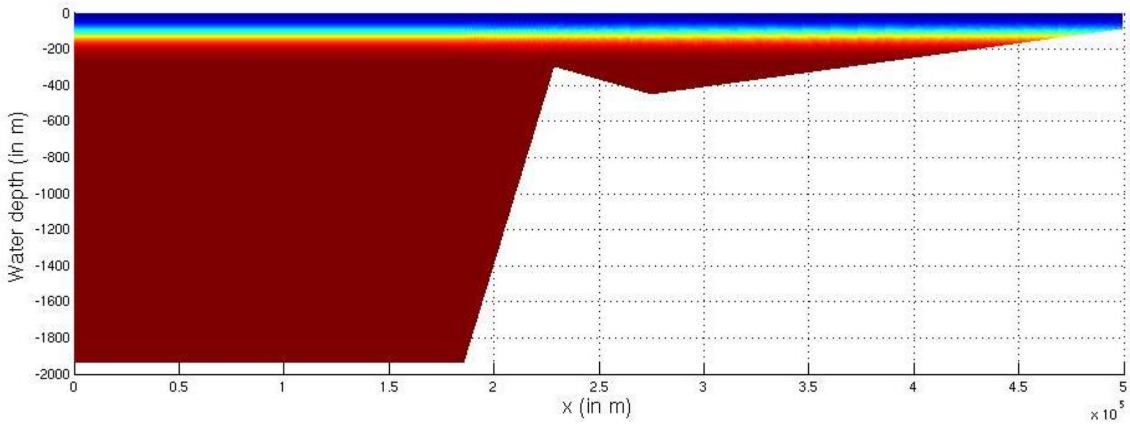

Figure 93. Cross-section D.

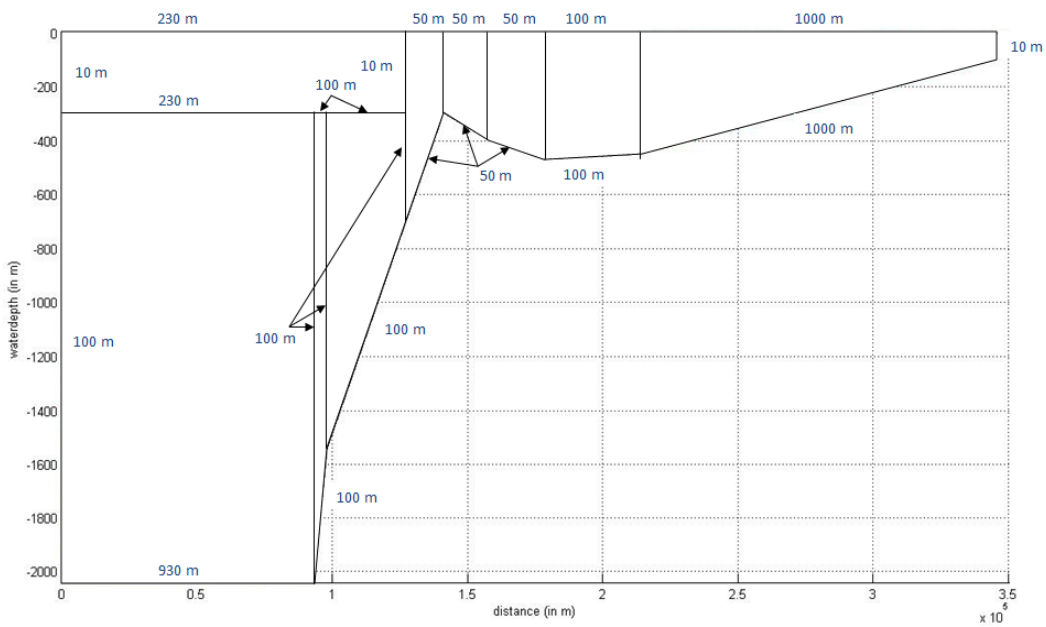

Figure 94. Resolution for grid A.

7.4.4 Results

Figure 95 shows the results for the simulation of the cross-section of Scott Reef (for cross-section shown in Figure 92). As predicted, the reef blocks the flow: there is limited flow over the obstacle into shallower water. However, the water that hits the reef is reflected and a group of solitons is generated and travels towards deep water. A second packet of solitons propagating towards the left can also be observed at x = 150 km.

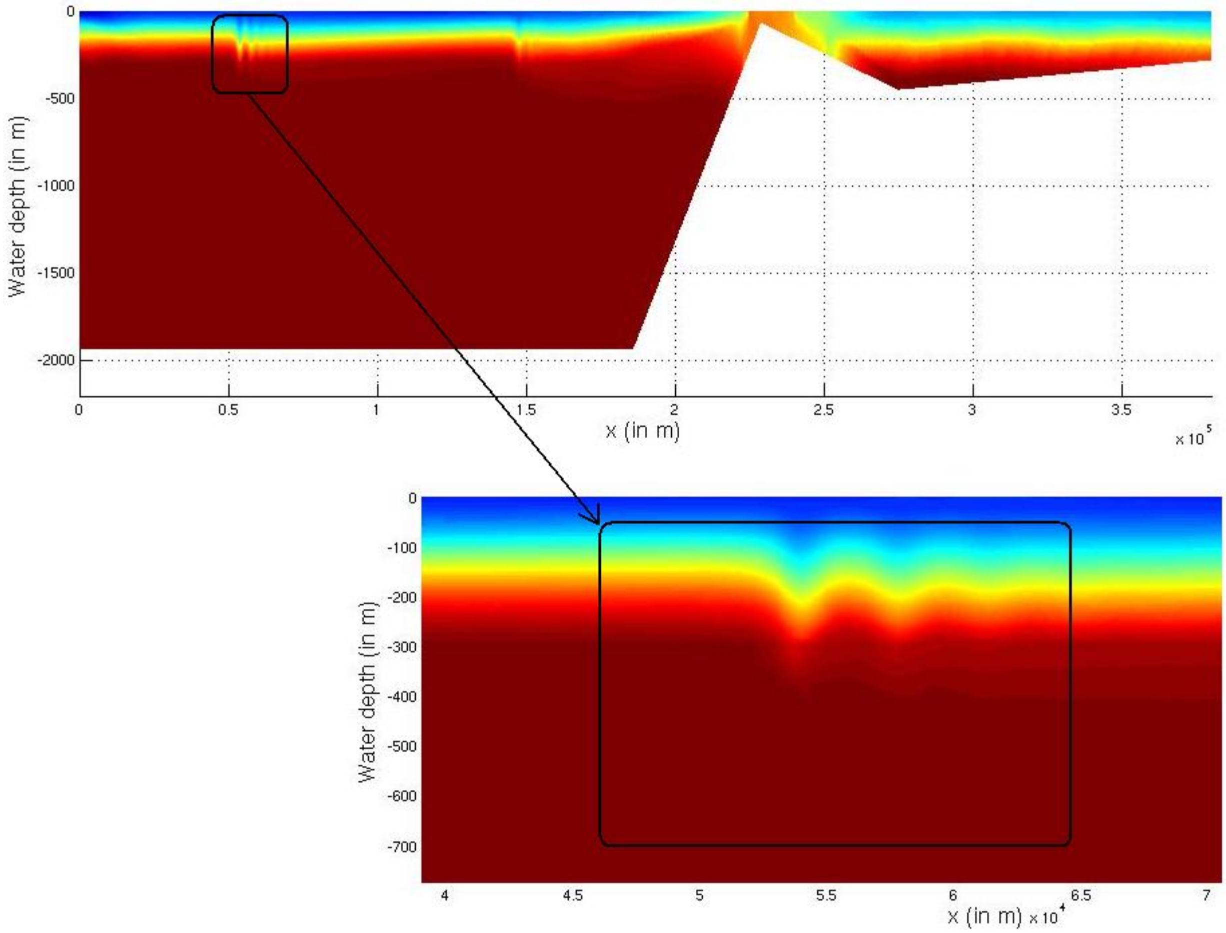

Figure 95. Soliton propagation on a section near the Scott Reef.

The situation where the top of the reef is located under the thermocline (for example cross-section A) does allow flow to propagate over the obstacle and into shallower water. Solitons packets now evolve on both sides of the reef and travel in opposite directions.

First, tidal flow forces water to propagate towards the reef. As the flow weakens, a soliton packet is formed on the west (left in figure) side of the reef and propagates offshore towards deeper water. Then the tidal flow reverses and water is forced towards the reef again. A packet of solitons is now generated on the eastern (right) side of the reef and propagates onshore. As the flow weakens once more, a new soliton packet is generated on the western side of the reef and propagates offshore. This is illustrated in Figure 96.

Figure 97 shows close-ups of two soliton packets. The wave packets on the offshore side (left) of the reef travel towards the western (left) boundary and the wave packet on the onshore (right) side of the reef travels towards the eastern (right) boundary of the domain. The latter disappears in the shallower water after x = 225 km. This is due to the coarse resolution in that part of the grid (1000 m).

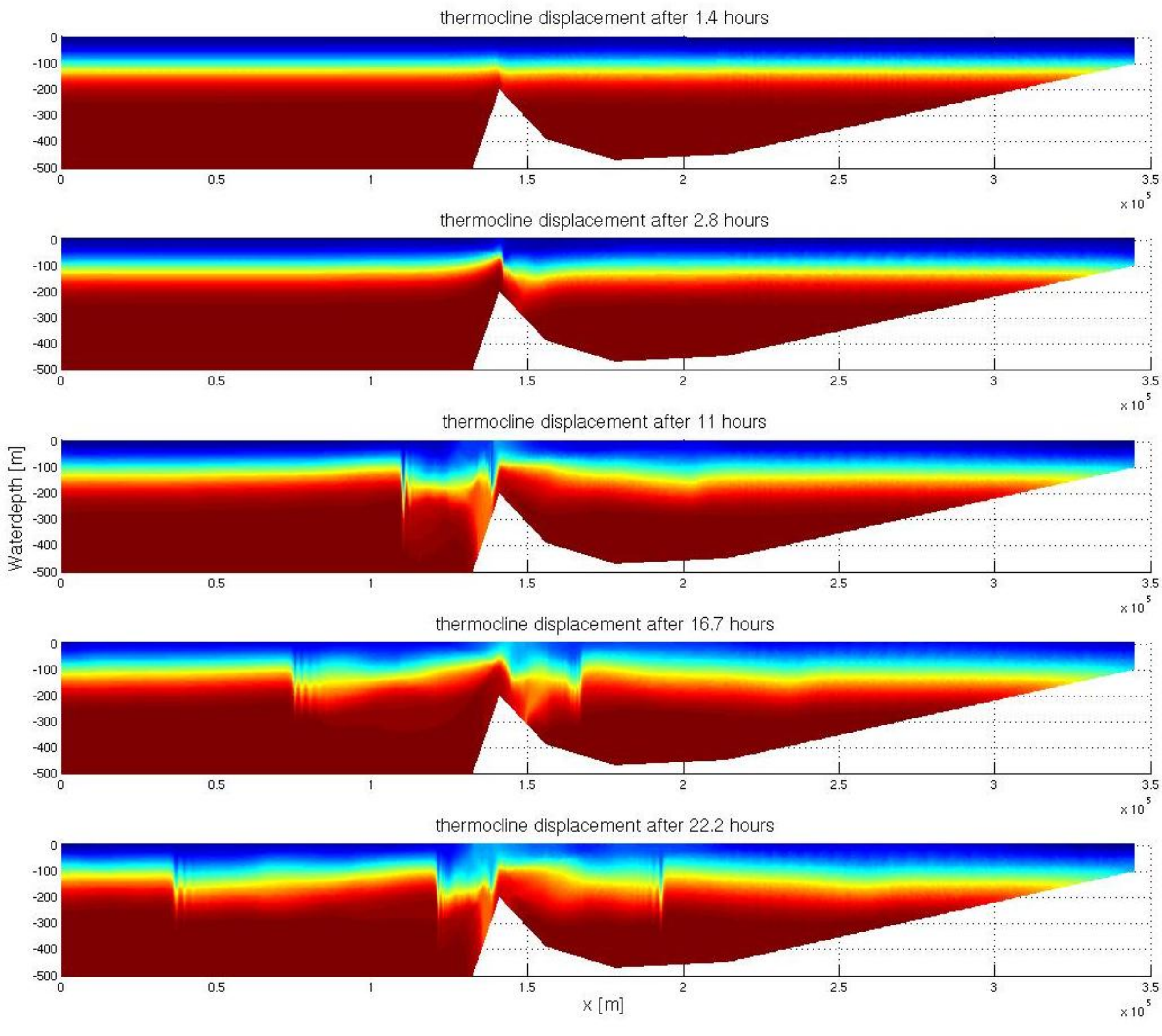

Figure 96. Thermocline displacement near the reef at different times for cross-section A.

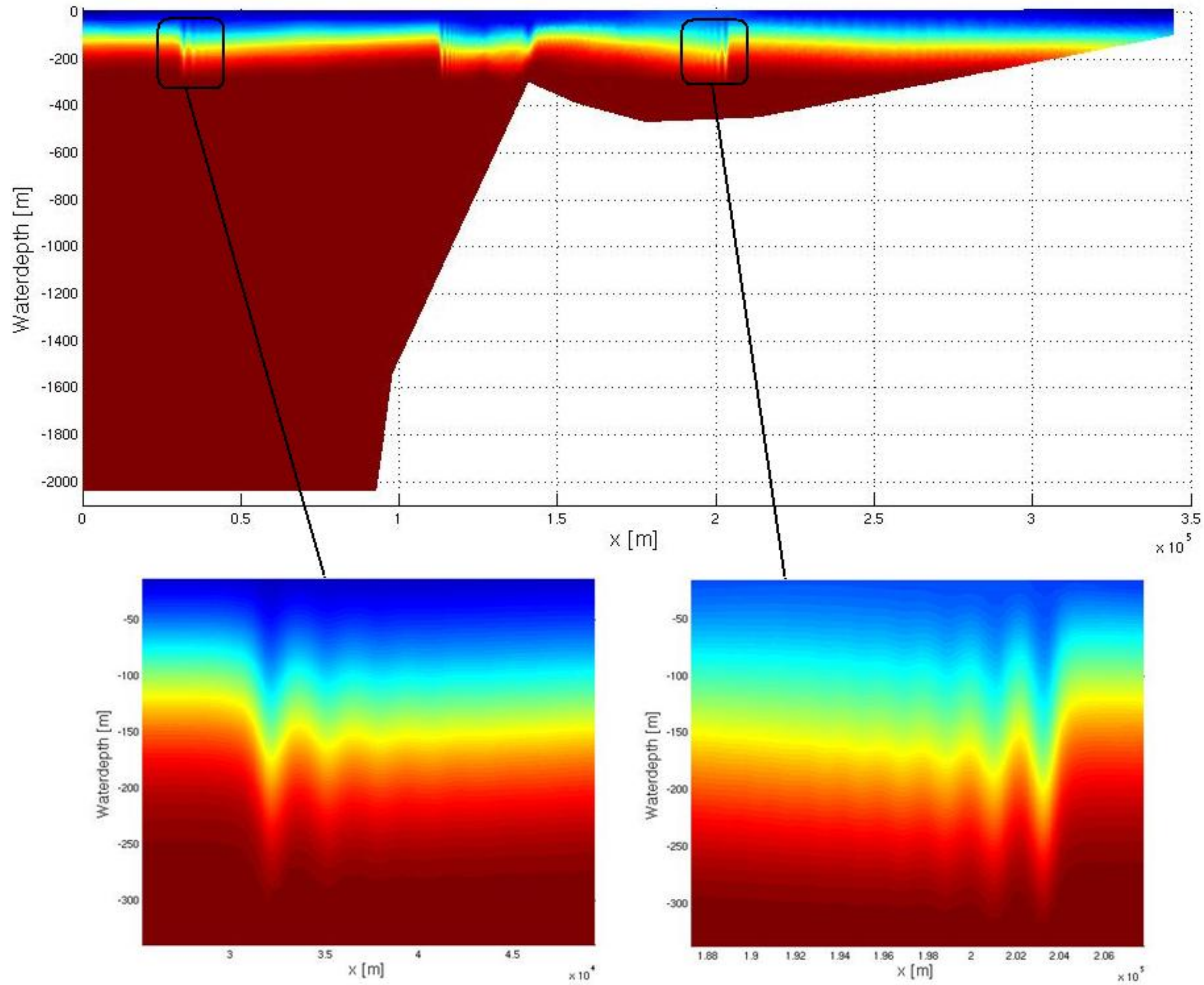

Figure 97. Soliton generation with mesh A.

7.4.5 Analysis

The simulations show that wave packets of three or four waves are formed. The largest waves lead the group and have lengths of 2000-2250 m. The waves have periods of 25 to 35 min and amplitudes of approximately 30 m. Figure 98 shows time series of the interface displacement at two locations in cross-section A. The solitary wave packet is clearly visible and it can be observed that at the deep water location (upper figure), wave packets pass after approximately 12 hours, 24 hours and 36 hours. This shows a clear correlation with the semi-diurnal tide. This was not the case in the sampled data.

A wave packet can also be observed at t = 42 hours. This is a packet that was generated near the top of the reef, propagated towards the deeper water, reflected at the inflow boundary and travelled back towards the reef.

The lower figure shows the interface displacement at a location behind the reef. Here, wave packets are also observed at 12 hour-intervals, although the first packet only appears after 18 hours.

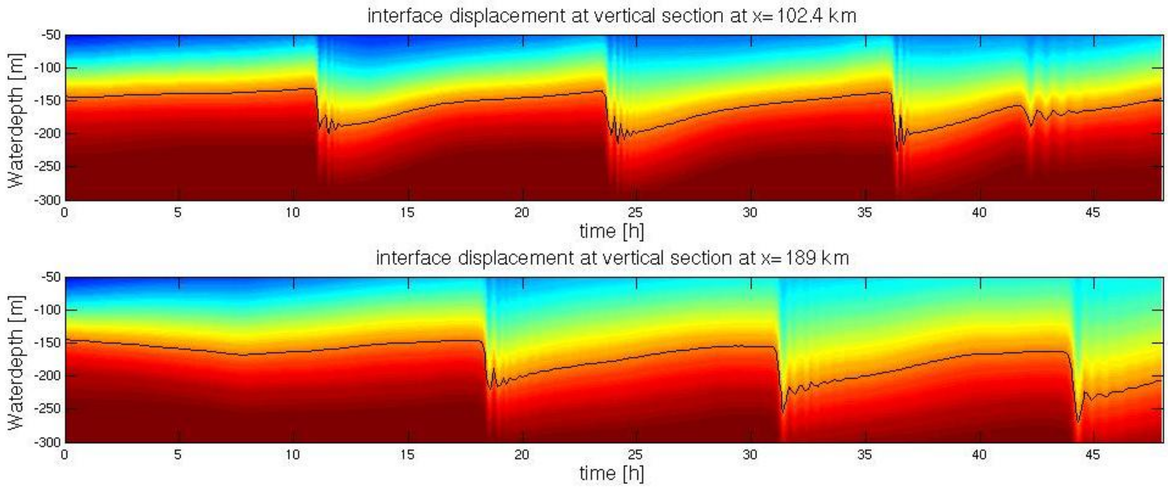

Figure 98. Soliton packets in time at two locations. Upper = lower = say where they are located

Figure 99 shows the horizontal velocities in the water column at x =104.4 km. The tidal variation can be observed, as well as the strong change in velocity during the passage of the wave packets. Velocities of 0.6 m/s are computed at these times. It can also be observed that the horizontal velocity is constant over the water depth in the first few hours. This is no longer the case later on. Not only during the passage of the solitons, but already hours before there is a shear flow. This is in accordance with the current speed data, which always showed a shear flow hours before the occurrence of a soliton.

Horizontal velocities of 1 m/s were computed in the water column above the top of the reef (at x = 141 km) for a simulation with an inflow velocity with amplitude 0.25 m/s.

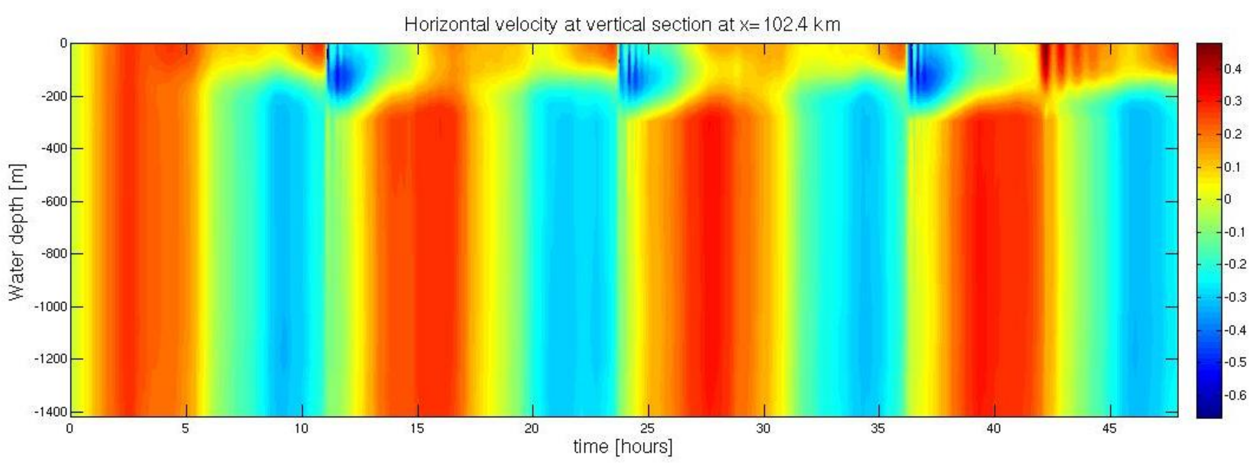

Figure 99. Horizontal velocities at x=102.4 km.

The two other cross-sections also showed solitons packets generating at both sides of the reef and propagating away in different directions. It can therefore be assumed that solitons in the Browse Basin can be generated at several locations and propagate in different directions. This is in accordance with the findings from chapter 6; the waves were found travelling in different directions and had different shapes.

7.4.6 Conclusion

The meshes used for the simulations in the Scott Reef area showed the generation and propagation of solitons. The grid resolution is fine enough in the generation area to capture solitary waves but too coarse near the eastern boundary to capture the propagation of the wave packets in that direction. The resolution near the western boundary on the other hand was fine enough to show the propagation of the generated solitary wave packets. It can therefore be concluded that a horizontal resolution of 50 m is required in the generation area and 230 m in the propagation areas. A resolution of 1000 m is too coarse. These values suggest that the resolution of the shelf grid is too low to accurately resolve internal solitary waves. The combination of bathymetry, stratification and tidal flow works well and forms a good starting point for further research.

For the idealised two dimensional flow simulations presented here, the tidally forced flow of highly stratified waters over the steep bathymetry of Scott Reef is sufficient to generate solitons. This is likely to be true for idealised Seringapatam Reef simulations too. Both Scott Reef and Seringapatam Reef should be explored further as possible soliton generation areas in the Browse Basin. However, the three-dimensional effects that are not captured in the two-dimensional simulations will have big influence and it is therefore not possible to draw conclusions on the generation at the reefs. This will be discussed in more detail in chapter 9. The computed solitons had amplitudes and periods that strongly resembled the measurements. They travelled in groups that were generated approximately every 12 hours. This is not the case in reality; solitons were not observed on a regular basis. Therefore further research is recommended to study other influences. This will be discussed in section 7.5.

7.5 Conclusions and recommendations

The analysis of the simulation results of the shelf and the reef in the sections above leads to a number of conclusions.

- Finlab can be applied to large computational domains of 300-500 km while at the same time having a fine enough resolution in some parts of the computational domain to capture soliton generation. A horizontal resolution of 50 m in the generation area and 230 m in the propagation areas in combination with a vertical resolution of 10 m and a time step of 100 s works well.
- Scott and Seringapatam Reefs are likely soliton generation areas, but 3D simulations are necessary to verify this.
- The mesh generator allows a maximum of 70,000 grid points in a numerical domain. This number is too small for simulations on domains covering the whole shelf from the deep ocean to the coast (>500 km). It is therefore not possible to have a fine enough resolution and as a result it is not possible to study solitons generation and propagation on the shelf.

The following suggestions for further research are given:

- Another grid generator should be used to make a mesh of the shelf with the same resolution that worked for the reef meshes. A simulation on this grid with the same boundary and initial conditions as mentioned before will show if resolution caused the absence of solitons.
- If solitons are not observed on the shelf with higher resolution, a number of different cross-sections of the shelf should be modelled to test if solitons can be generated with the shelf bathymetry.
- More detailed bathymetry should be used. The importance of bathymetric features has been demonstrated in this chapter and it is therefore recommended to use less-idealized bottom topography.
- Different tidal components (not only M2 as was used in these simulations) should be superimposed and the spring/neap tidal cycle simulated to gain better understanding of the correlation between the tidal motions and the occurrence of solitons. The numerical results can be validated with the data.
- The closed right hand side boundary of the reef meshes was in water depths of 100-200 m. This was done because extending the grid further would mean that the resolution elsewhere had to be coarser. However, with another grid generator the domain can be extended to prevent unrealistic flow situations due to reflecting waves at the boundary.
- 3D-simulations of Scott Reef should be set up to gain better understanding of three-dimensional effects of the reef. Domains of 50 x 50 km are recommended as that will encompass the whole Reef and allow enough space between the Reef itself and the open boundary conditions.

Chapter 8 – Discussion

Solitary internal waves are a common feature in the world's oceans. Their influence on ocean mixing and the potential threat they can pose to offshore structures has been the reason for many field and numerical studies.

Solitons are small-scale waves evolving from larger-scale flow features and can be generated through different mechanisms. The combination of the scale-difference and complicated generation mechanisms, in addition to their non-linearity, make solitons challenging features to numerically simulate.

After extensively testing Finlab for different generation mechanisms using laboratory tests and showing that the Finlab model is very suitable for modelling solitons, the focus of this thesis shifted to modelling solitons near Scott Reef on a more realistic scale. As mentioned in section 7.4, Scott Reef has previously been studied by Wolanski and Deleersnijder (1998), Rayson (2006) and Costin (2010). The results of their field data studies and numerical research show that Scott Reef adds a number of challenges to the already complicated subject of numerically modelling solitons.

For example, Wolanski and Deleersnijder (1998) showed with their numerical model that the baroclinic tidal waves will go partially around the reef. This weakens the flow over the reef (Munroe and Lamb 2005). Also, wave amplitudes decrease with distance from the reef because of radial spreading. Finlab takes neither effect into account in the 2D-simulations. Some bathymetries are uniform enough in the cross-shelf direction that a two-dimensional simulation will give reasonably realistic results. Scott Reef however will have significant three-dimensional effects that cannot be neglected. It is important to keep the 3D-effects in mind.

Scott Reef rises very steeply from the sea floor. The ROMS model (Regional Ocean Modelling System) that Rayson (2006) used had its vertical coordinates defined by a sigma-coordinate system. This system caused pressure gradient errors and in combination with the steep slopes of Scott Reef, ROMS became unstable. The steep bathymetry required significant smoothing to stabilise the model solution. The simulations in this thesis have shown that Finlab does not became unstable for steep slopes, nor does it have severe restrictions on the resolution or time step in terms of the Courant number, as did the ROMS model.

Another issue is the lack of information on the stratification in the Scott Reef area. Wolanski and Deleersnijder (1998) found negligible horizontal density gradients near Scott Reef. In the Finlab simulations, no horizontal gradients were posed. Wolanski and Deleersnijder (1998) did observe large horizontal density gradients at the continental shelf edge. This shows that the assumption that there are no horizontal gradients is not automatically valid. This must be kept in mind when simulating other parts of the North West Australian Shelf. In the Finlab simulations, the continuous vertical stratification was based on a density profile observed at one location in the Browse Basin in 250 m water depth. Below 250 m water depth, the water column was assumed to be non-stratified. Deep water stratification can be important for internal wave generation. However, it is remarked that the resolution in deep water was so coarse (>100 m) that deep water stratification effects would most likely not have been captured anyway.

Once there is more information available on the stratification, horizontal density gradients and deep water stratification can easily be incorporated in the Finlab simulations via the initial conditions. For an accurate simulation of the deep water stratification effects, a higher vertical resolution should be used.

Finlab can handle a continuous stratification, whereas the numerical model used by Wolanski and Deleersnijder was a two-layer model. Finlab can therefore be used to investigate the mode one and two internal wave energy found by Costin (2010).

Based on the above it can be concluded that, making use of the advantages of Finlab, future simulations with Finlab can provide a valuable tool in increasing the knowledge about Scott Reef that is currently based on field data studies and other existing numerical models. However, a number of issues were also raised in chapter 7 that must be dealt with before solitons near Scott Reef can be modelled successfully with Finlab.

The coarse grids had very negative effects on the results. For example, the resolution on the shelf grid could not be refined enough to capture the generation of solitary waves. Also, the numerical domain could not be extended all the way to the coast, which resulted in a closed boundary in 100 m water depth and the introduction of standing barotropic waves in the domain, negatively influencing the flow near the shelf break. The coarse grid in the deep water part introduced an unrealistic amount of diffusion that will have consequences for the wave generation in shallower water. Solitary waves that were generated on the Scott Reef grids disappeared when they propagated towards shallower water as the resolution became very coarse again. The standing waves can be avoided by extending the numerical domain to the coast or by using a flow relaxation scheme that will damp all the incoming waves and prevent reflections. This solution will also have a shorter computational time because the numerical domain will be shorter. Diffusion can be reduced with finer resolution grids.

For still more accurate results of the Scott Reef simulations, the Coriolis effect should be taken into account in future numerical simulations. Although the Coriolis effect could be neglected on the small-scale, short simulations, the transition to simulations on domains with length of hundreds of kilometres and simulation times of several days no longer justifies this simplification.

Tidal forcing in the Browse Basin is dominated by the M_2 tide, although other tidal components are present. The simulation results have shown that the model responds to different tidal boundary conditions. However, only the tidal conditions in 250 m water depth in the Browse Basin are known from the field data analysis. They will be very different from tidal conditions hundreds of kilometres away in the deep ocean. Therefore, observations or a baroclinic tidal model should be used to find realistic characteristics of the tide further offshore in the Browse Basin area. Different tidal components should be superimposed and the spring/neap cycle introduced as the data analysis showed a relation between soliton occurrence and neap tide.

Chapter 9 – Conclusions and recommendations

9.1 Introduction

The objectives of this study were to investigate if the numerical model Finlab can be used for the numerical simulation of solitary internal waves in the Browse Basin and to gain a better understanding of the internal wave dynamics in the Browse Basin through data analysis and numerical simulations. In this chapter, conclusions concerning these objectives are presented and recommendations for further research are proposed.

9.2 Conclusions

Regarding the capabilities and limitations of Finlab, the following conclusions can be made:

- The overall results of the validation tests show good resemblance to the laboratory results. They are consistent and by choosing the correct numerical parameters, all the important flow features are captured and errors are reduced to an acceptable limit.
- High resolution grids are required for accurate results. As a consequence, the CPU time is long (72 hours for Scott Reef simulations). Making good use of the advantages of unstructured grids helps to reduce the computational time.
- Outflow boundary conditions cause a problem. They create a disturbance that slowly travels upstream. This effect can be delayed by extending the grid.
- Simulations with input conditions based on the Browse Basin bathymetry and stratification show realistic results when compared to the field data.

Based on all the above sub-conclusions, it can be concluded that Finlab is capable of accurately simulating internal solitary waves in the Browse Basin.

Regarding the internal wave dynamics in the Browse Basin, the following conclusions can be made:

- Twelve to fifteen large solitary internal waves are observed in the Browse Basin per year and smaller disturbances occur almost daily.
- The solitons have different shapes: depression waves, elevation waves and second mode waves. The depression waves occur throughout the year but mainly from December to February. The second mode waves are also found throughout the year, but mainly in January, February and June.
- The depression waves occur at high tide, the other waves occur both at high tide and at low tide. More than half of all the waves arrive five to seven days after spring tide.

- The generation area is still unknown. Idealized numerical tests have shown that Scott and Seringapatam Reefs, located some 150 km west of Prelude, are capable of generating internal solitary wave packets but more realistic simulations are required to verify this.

9.3 Recommendations

The following recommendations are made to reach the long-term goal set by Shell to set up a model that can predict the frequency of occurrence and intensity of solitons in the Browse Basin:

- Gather information on the generation areas of the solitons and their direction of propagation through a field survey at several locations in the Browse Basin or by acquiring SAR images in that region.
- A detailed field data study of the correlation of the solitons with stratification and the tidal cycle would help to understand under what conditions first and second waves are generated.
- The study on these correlations should be supported by numerical simulations as they can include the influence of bathymetry.
- Another grid generator should be used that does not impose limits on the number of grid points that can be used in a grid.
- Extend the numerical simulations of Scott Reef to three dimensions to study the 3D effects of the irregular bathymetry.

References

Aghsaee, P., Boegman, L. and Lamb, K. G. (2010). "Breaking of shoaling internal solitary waves." Journal of Fluid Mechanics **659**: 289-317.

Apel, J. R. (2002). An Atlas of oceanic internal solitary waves, Global Ocean Associates - Office of Naval Research.

Baines, P. G. (1981). "Satellite Observations of Internal Waves on the Australian North-west Shelf." Australian Journal of Marine and Freshwater Research(32): 457-463.

Bluteau, C. E., Jones, N. L., Ivey, G. N. and Pattiaratchi, C. B. (2010). Bottom boundary layer dynamics in an internal wave generation zone. 17th Australasian Fluid Mechanics Conference. Auckland, New Zealand.

Boegman, L., Imberger, J., Ivey, G. N. and Antenucci, J. P. (2003). "High-frequency internal waves in large stratified lakes." Limnology and Oceanography **48**(2): 895-919.

Boegman, L., Ivey, G. N. and Imberger, J. (2005). "The degeneration of internal waves in lakes with sloping topography." Limnology and Oceanography **50**(5): 1620-1637.

Condie, S. A. and Andrewartha, J. R. (2008). "Circulation and connectivity on the Australian North West Shelf." Continental Shelf Research **28**.

Costin, J. (2010). Circulation in the Lagoon of South Scott Reef, Bachelor thesis, University of Western Australia.

Davidson, L. (2011). An Introduction to Turbulence Models. Department of Thermo and Fluid Dynamics. Goteborg, Chalmers University of Technology.

Flynn, J. (2010). Metocean Reference Document F-block Australia, Shell Exploration and Production.

Gerkema, T. and Zimmerman, J. T. F. (2008). An introduction to internal waves. Texel, Royal NIOZ.

Goff, M., Jeans, G., Harrington-Missin, L. and Baschenis, C. (2010). Soliton early warning system for offshore applications. Oceanology International Conference.

Hanif, K. (2004). Accelerated flows of viscoelastic fluids with no-slip and partial slip conditions, PhD thesis. Department of Mathematics. Islamabad, Quaid-i-Azam University.

Holloway, P. E. (1994). "Observations of internal tide propagation on the Australian North West Shelf." Journal of Physical Oceanography **24**(8): 1706-1716.

Holloway, P. E. (1996). "A Numerical Model of Internal Tides with Application to the Australian North West Shelf." Journal of Physical Oceanography **26**.

Holloway, P. E. and Chatwin, P. G. (2000). "Internal Tide Observations from the Australian North West Shelf in Summer 1995." Journal of Physical Oceanography **31**.

Horn, D., Imberger, J. and Ivey, G. (1998). "The degeneration of basin-scale internal waves in lakes." Proceedings of the 1998 Thirteenth Australasian Fluid Mechanics Conference, Melbourne, Australia, 13-18 December 1998 (Volume 2): 863-866.

Hyder, P., Jeans, D. R. G., Cauquil, E. and Nerzic, R. (2005). "Observations and predictability of internal solitons in the northern Andaman Sea." Applied Ocean Research **27**(1): 1-11.

Jeans, D. R. G. and Sherwin, T. J. (2001). "The variability of strongly non-linear solitary internal waves observed during an upwelling season on the Portuguese shelf." Continental Shelf Research **21**(16-17): 1855-1878.

King, B., Zhang, H. P. and Swinney, H. L. (2009). "Tidal flow over three-dimensional topography in a stratified fluid." Physics of Fluids **21**(116601).

Kranenburg, C. and Pietrzak, J. D. (1990). "Internal lee waves in turbulent two-layer flow." Journal of Hydraulic Engineering **115**(10): 1352-1370.

Labeur, R. and Pietrzak, J. (2004). Computation of non-hydrostatic internal waves over undular topography. Shallow Flows, Taylor & Francis**:** 187-194.

Labeur, R. J. (2009). Finite element modelling of transport and non-hydrostatic flow in environmental fluid mechanics, PhD thesis. Department of Environmental Fluid Mechanics, Technische Universiteit Delft.

Lamb, K. G. (1994). "Numerical experiments of internal wave generation by strong tidal flow across a finite amplitude bank edge." Journal of Geophysical Research **99**(C1): 843-864.

Lamb, K. G. (1998). "Are Solitary Internal Waves Solitons?" Studies in Applied Mathematics **101**: 289-308.

Lewis, R. W., Nithiarasu, P. and Seetharamu, K. N. (2004). Fundamentals of the Finite Element Method for Heat and Fluid Flow. Chichester, John Wiley & Sons Ltd. .

Marine and Biodiversity Division (2008). North-west Marine Bioregional Plan Bioregional Profile. Kingston, Australian Government Department of the Environment, Water, Heritage and the Arts.

Maxworthy, T. (1979). "A note on the internal solitary waves produced by tidal flow over a three-dimensional ridge." Journal of Geophysical Research **84**: 338-346.

Mellor, G. L. (1996). Introduction to Physical Oceanography. Woodbury, American Institute of Physics Press.

New, A. L. and Da Silva, J. C. B. (2002). "Remote-sensing evidence for the local generation of internal soliton packets in the central Bay of Biscay." Deep-Sea Research **I**(49): 915-934.

Pietrzak, J. D., Kranenburg, C., Abraham, G., Kranenborg, B. and van der Wekken, A. (1991). "Internal wave activity in Rotterdam waterway." Journal of Hydraulic Engineering **117**(6): 738-757.

Rayson, M. D. (2006). A Three Dimensional Hydrodynamic Model of Scott Reef, Western Australia, BSc thesis, University of Western Australia, School of Environmental Systems Engineering.

Rayson, M. D., Ivey, G. N., Jones, N. L., Meuleners, M. J. and Wake, G. W. (2011). "Internal tide dynamics in a topographically complex region: Browse Basin, Australian North West Shelf." Journal of Geophysical Research C: Oceans **116**(1).

Uijttewaal, W. (2010). Lecture Notes Turbulence in hydraulics. Environmental Fluid Mechanics section, University of Technology Delft.

Van Gastel, P., Ivey, G. N., Meuleners, M. J., Antenucci, J. P. and Fringer, O. (2009). "The variability of the large-amplitude internal wave field on the Australian North West Shelf." Continental Shelf Research **29**(11-12): 1373-1383.

Vlasenko, V., Stashchuk, N. and Hutter, K. (2005). Baroclinic tides. New York, Cambride University Press.

Vlasenko, V. I. and Hutter, K. (2001). "Generation of second mode solitary waves by the interaction of a first mode soliton with a sill." Nonlinear Processes in Geophysics(8): 223-239.

Wolanski, E. and Deleersnijder, E. (1998). "Island-generated internal waves at Scott Reef, Western Australia." Continental Shelf Research **18**.

Yang, Y.-J., Tang, T.-Y., Chang, M. H., Liu, A. K., Hsu, M.-K. and Ramp, S. R. (2004). "Solitons Northeast of Tung-Sha Island During the ASIAEX Pilot Studies." IEEE Journal of Oceanic Engineering **29**(4).

List of figures

Appendix I – Numerical parameters

****

* START INPUT FIELD *

****

Physical constants:

Grav = 9.81	gravitational acceleration	[m/s2]
U0 = 1	velocity scale	[m/s]
L0 = 1	length scale	[m]
R0 = 0.02	relative density transport variable	[-]

Time stepping parameters:

Dt = 0.1	time step	[s]
Theta = 0.5	implicitness momentum equation	[-]
Zeta = 0.5	implicitness continuity equation	[-]
Method = 1	time discretization: 1=Crank-N 2=Fract.Step	[-]
Move = 1	move surface (1) or rigid lid (0)	[-]
Tdamp = 0	damping time	[s]
Tstart = 0	initial time	[s]

In-/output settings:

Neind = 4000	number of time steps	[-]
Nwrit = 8	write result each nwrit timesteps	[-]
Mwrit = 600	maximum output steps before rewind	[-]

Turbulence modeling:

Turb = 3	turbulence model: 0=const 1=Lmix 2=k-eps 3=LES	[-]
Visc0 = 1.E-6	(minimum) kinematic viscosity	[m2/s]
Lmix = 0	(turbulent) mixing length	[m]
kN0 = 1.E-4	default Nikuradse wall roughness	[m]
Cf0 = 0	default wall friction factor	[-]
Cs = 0.15	Smagorinsky constant	[-]
Fluc = 0	relative random velocity fluctuation	[-]

Advection-diffusion scheme:

Gamma = 0.5	advective flux switch [0;1] advective-conservative	[-]
Upw = 1	upwind parameter advection [0;1]	[-]
Eta = -1	diffusive flux switch [-1;1] skew symmetric-symmetric	[-]
Limu = 9	polynomial order advection scheme: 0, 1, 9=adaptive	[-]
Limc = 9	polynomial order transport scheme: 0, 1, 9=adaptive	[-]

Transport parameters :

Nconc = 1	number of concentration species	[-]
Mu = 0	leap-frog factor density [0;1]	[-]
Nsource = 0	number of source terms (max 10)	[-]
Sigma = 1	Prandtl-Schmidt number	[-]

Boundary coding: 1=wall 2=surface 3=level 4=velocity 5=Riemann 6=wave 9=symm 0=internal:

For Tilted tank experiment:

group(1)	1
group(2)	1
group(3)	1
group(4)	1
group(5)	0

For Lee wave experiment:

group(1)	1
group(2)	3
group(3)	9
group(4)	4
group(5)	4
Group(6)	0

****

* END INPUT FIELD *

****

Appendix II – Field data

In this appendix, a selection is shown of the solitons that were identified in the field data commissioned by Shell Development Australia.

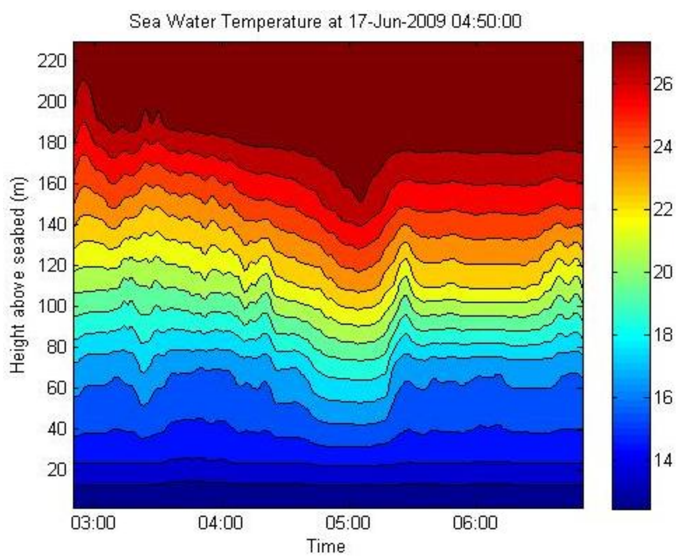

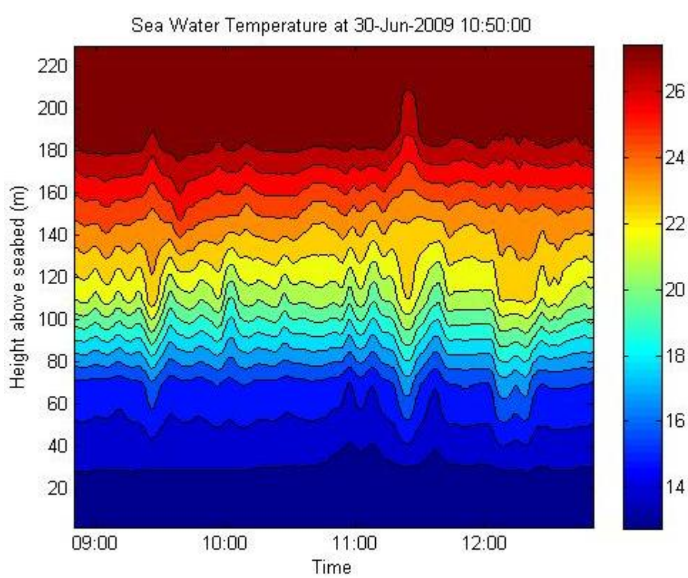

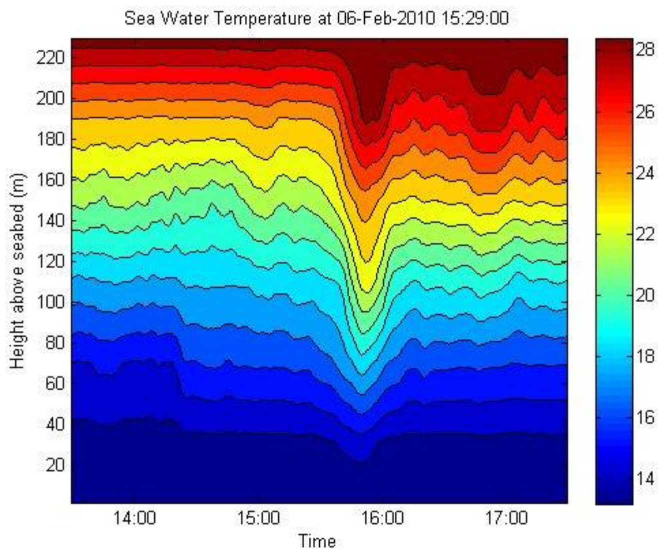
Sea Water Temperature at 06-Feb-2010 15:29:00
Height above seabed (m)
Time
14:00
15:00
16:00
17:00

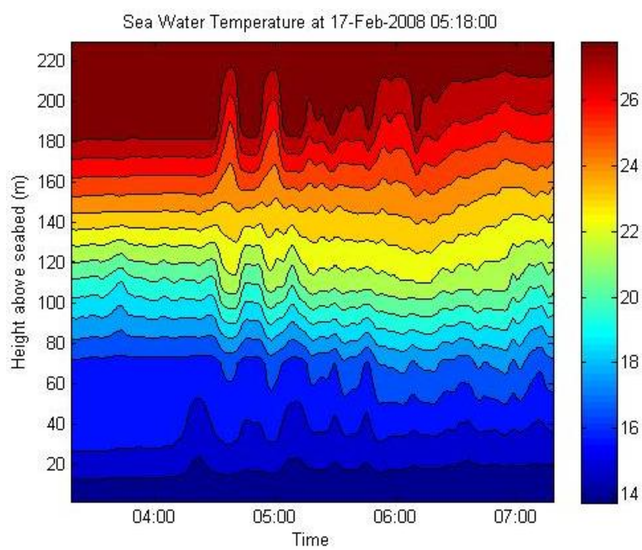
Sea Water Temperature at 17-Feb-2008 05:18:00
Height above seabed (m)
Time
04:00
05:00
06:00
07:00

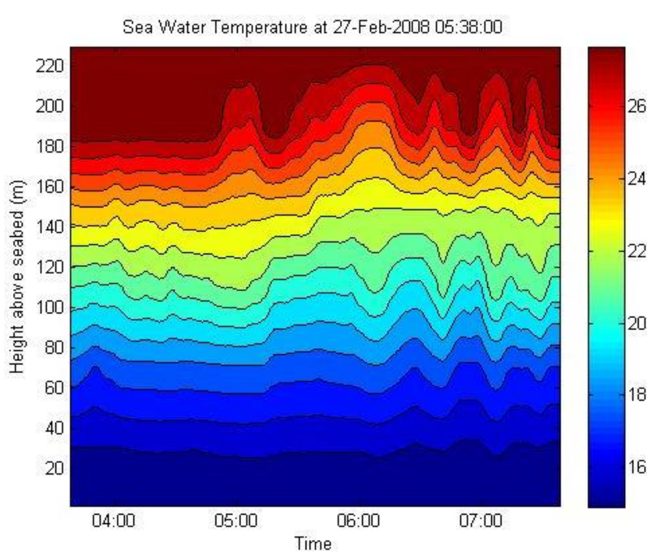
Sea Water Temperature at 27-Feb-2008 05:38:00
Height above seabed (m)
Time
04:00
05:00
06:00
07:00

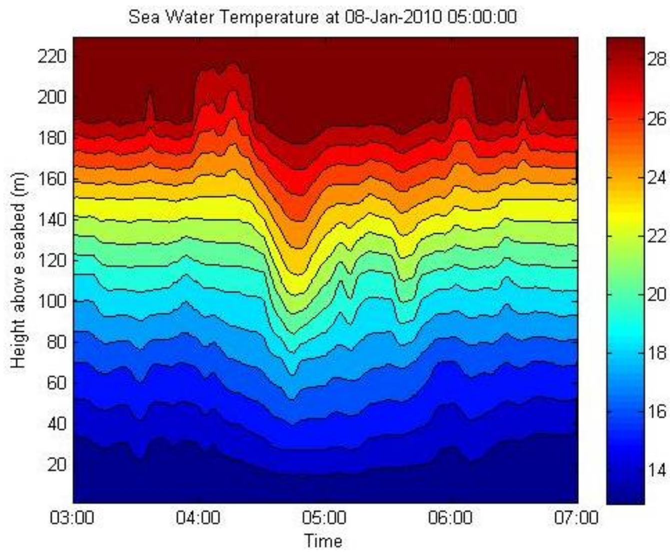
Sea Water Temperature at 08-Jan-2010 05:00:00
Height above seabed (m)
Time
03:00
04:00
05:00
06:00
07:00
220
200
180
160
140
120
100
80
60
40
20
28
26
24
22
20
18
16
14

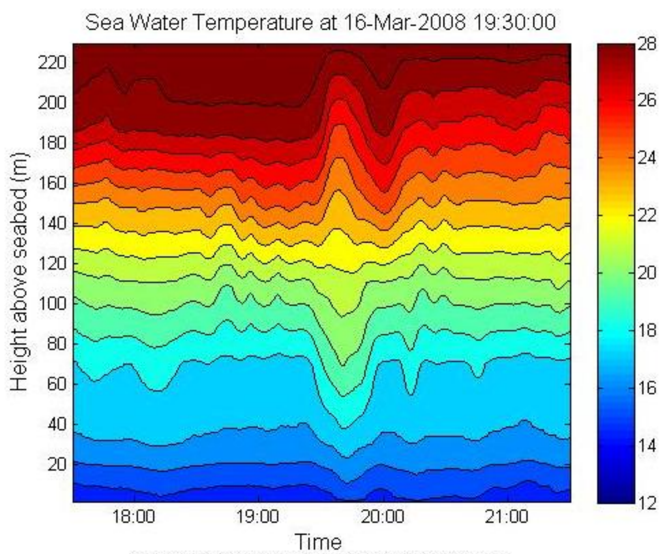
Sea Water Temperature at 16-Mar-2008 19:30:00
Height above seabed (m)
Time
18:00
19:00
20:00
21:00
220
200
180
160
140
120
100
80
60
40
20
28
26
24
22
20
18
16
14
12

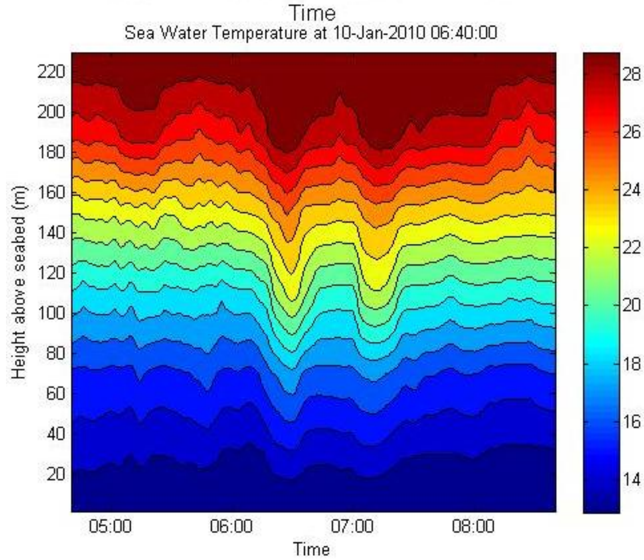
Sea Water Temperature at 10-Jan-2010 06:40:00
Height above seabed (m)
Time
05:00
06:00
07:00
08:00
220
200
180
160
140
120
100
80
60
40
20
28
26
24
22
20
18
16
14

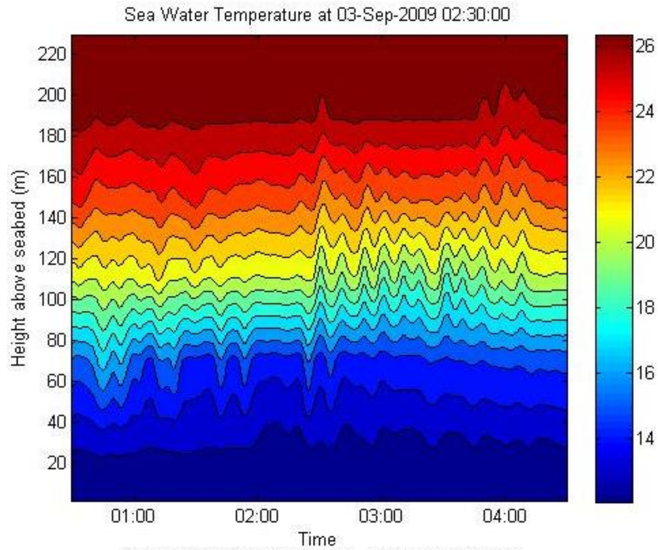
Sea Water Temperature at 03-Sep-2009 02:30:00
Height above seabed (m)
Time
220
200
180
160
140
120
100
80
60
40
20
01:00
02:00
03:00
04:00
26
24
22
20
18
16
14

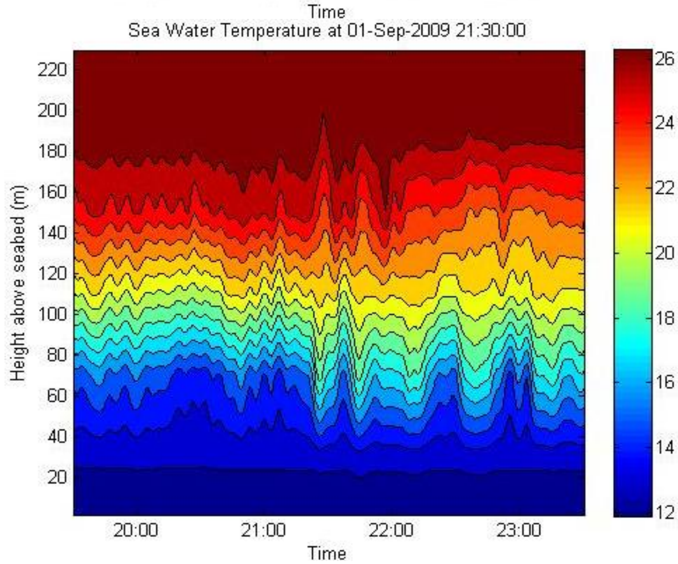
Sea Water Temperature at 01-Sep-2009 21:30:00
Height above seabed (m)
Time
220
200
180
160
140
120
100
80
60
40
20
20:00
21:00
22:00
23:00
26
24
22
20
18
16
14
12

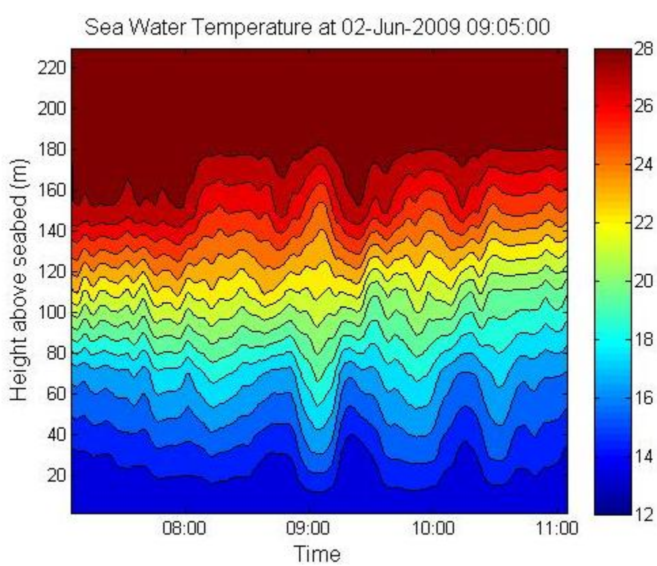
Sea Water Temperature at 02-Jun-2009 09:05:00
Height above seabed (m)
Time
220
200
180
160
140
120
100
80
60
40
20
08:00
09:00
10:00
11:00
28
26
24
22
20
18
16
14
12

Appendix III – Closed boundary simulations of the Browse Basin shelf

I. Introduction

As mentioned in section 7.2, numerical simulations were set up on three different grids with length 5200 m and closed boundaries. Only the results of one test were shown in that section. In this appendix, the numerical results of the other simulations are presented. Section 2 shows the initial conditions on the other cross-sections. In section 3, the results for the different shelf sections are presented. In section 4, the results of simulations with different thermocline slopes are discussed and the results of simulations with different stratification are shown in section 5.

II. Numerical set up

Figure 100 shows the three sections of the shelf that will be investigated. Section 1 has a slope of 0.2%, section 2 has a slope of 1.2% and section 3 has a slope of 2.0%. Water depths range from 250 m to 1200 m. The numerical domains are shown in Figure 101, Figure 102 and Figure 103.

Figure 100. Shelf break sections.

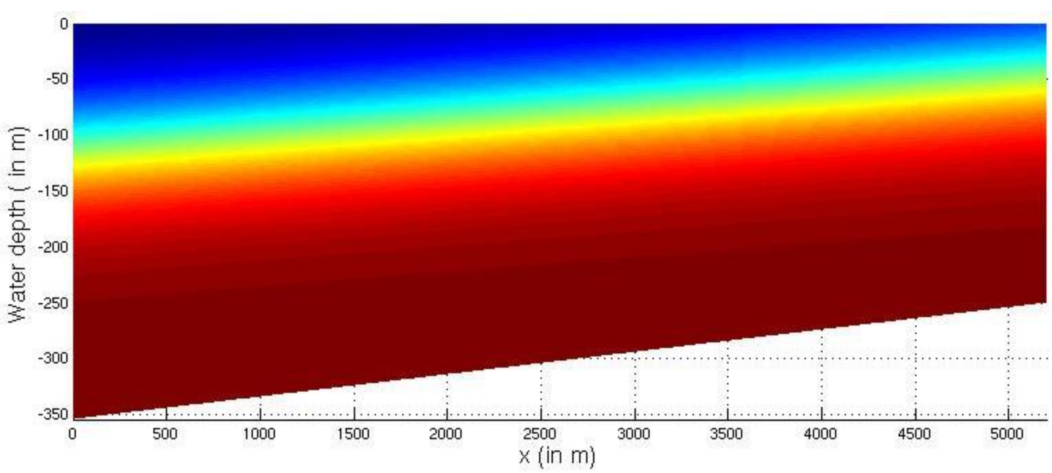

Figure 101. Numerical set up for shelf section 1.

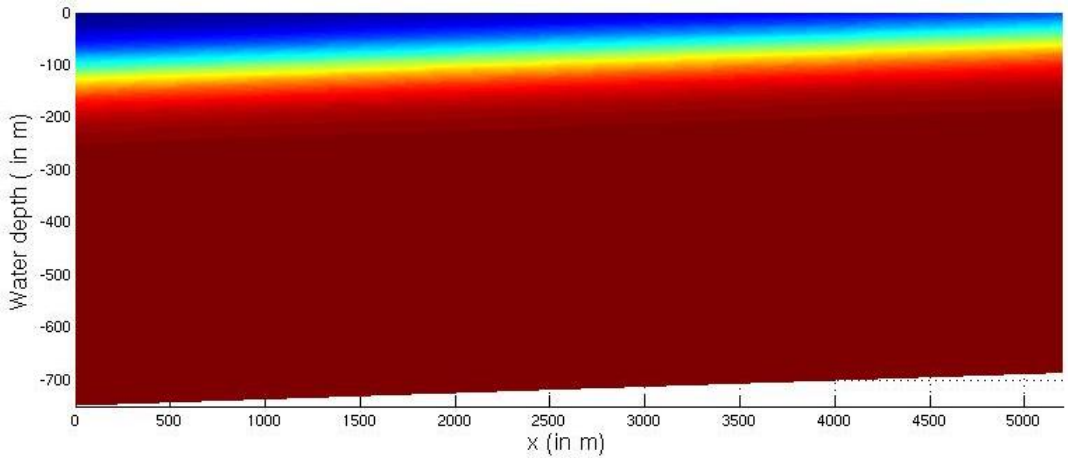

Figure 102. Numerical set up for shelf section 2.

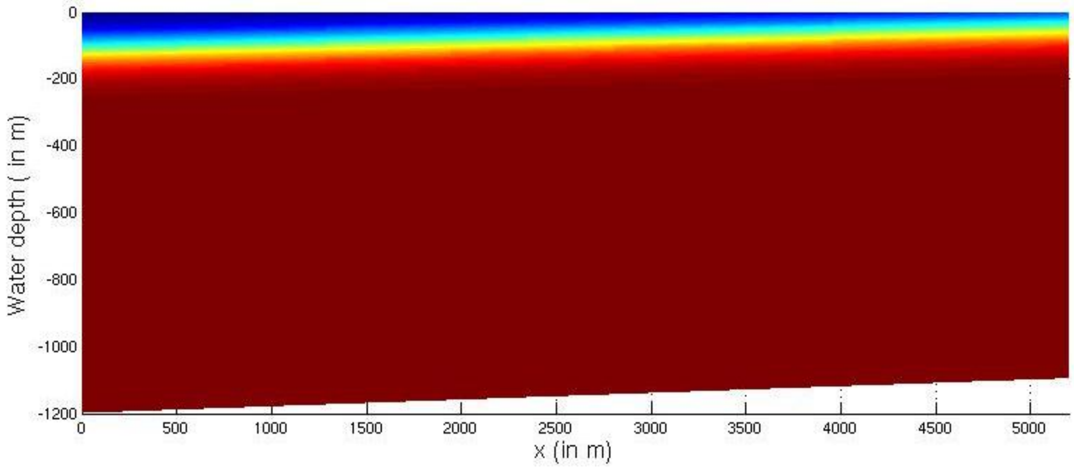

Figure 103. Numerical set up for shelf section 3.

III. Cross-sections

The stratification as mentioned in section 7.2.2 and a sloping thermocline with an angle of 0.013% are imposed on the three shelf sections. Figure 104 to Figure 106 show time series of the density contour displacements at x=1500 m for each of the cross-sections. Only the upper 255 m of water are shown as this is the layer where waves occur. All three figures show solitons.

The figures also show a number of differences. The solitons are generated much faster for shelf break sections 2 and 3. This could be explained by assuming that the steeper slopes speed up the process of steepening of the initial long wave. However, the waves at shelf break section 3 are much smaller. It is assumed that the deep water reduces the amount of steepening.

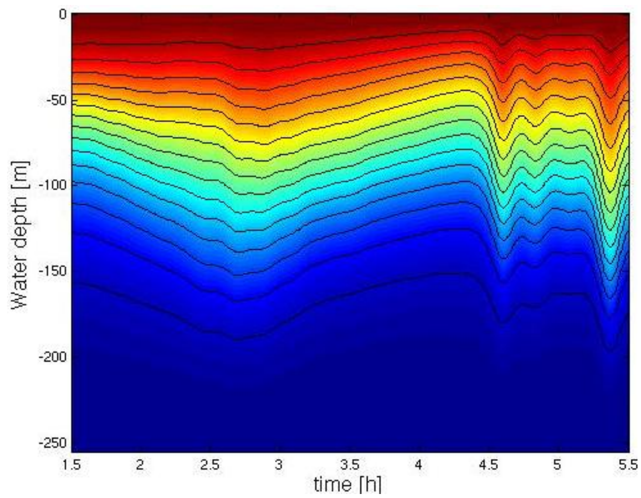

Figure 104. Density contours on shelf break section 1 at x=1500 m.

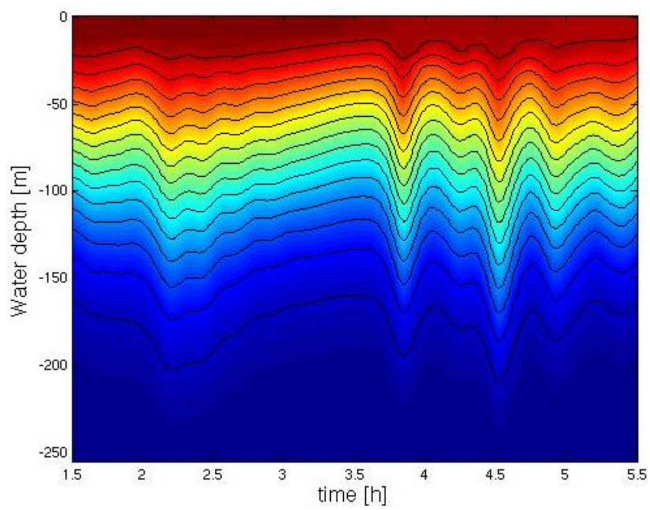

Figure 105. Density contours on shelf break section 2 at x=1500 m.

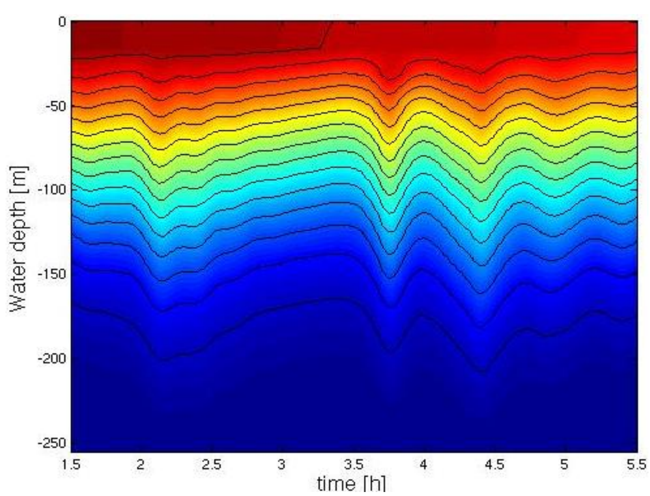

Figure 106. Density contours on shelf break section 3 at x=1500 m.

IV. Angle of thermocline slope

Two simulations are set up on the shelf break section 2 grid. The first one has a tilted interface with an initial amplitude of 67.5 m and the second one with an initial amplitude of 50 m. It is expected that the smaller initial amplitude feeds less energy into the system and therefore the resulting solitons will have lower amplitudes. The results are shown in Figure 107 and they are in accordance with this assumption.

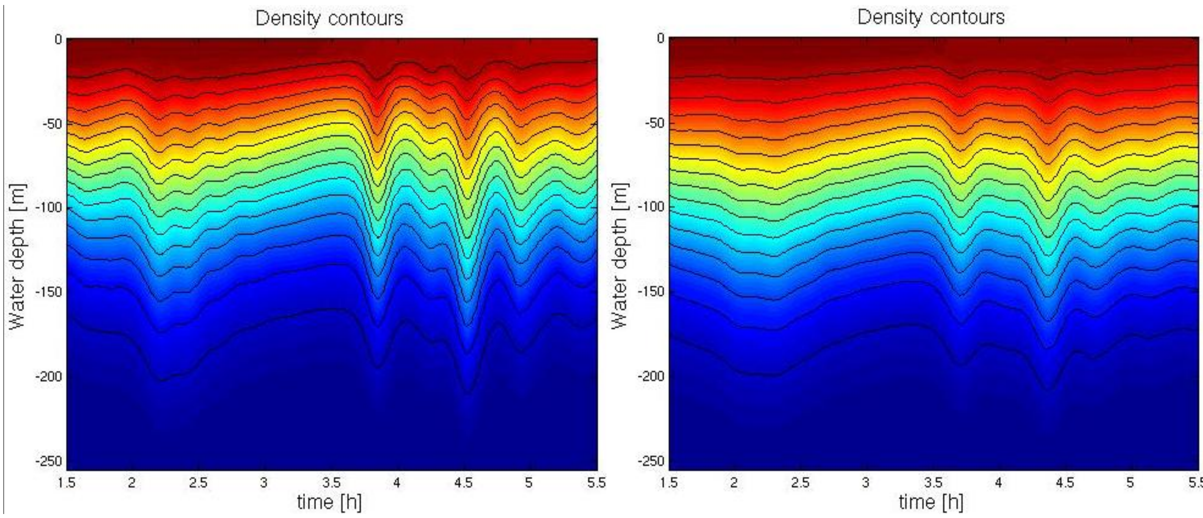

Figure 107. Density contours on shelf break section 2 at x =1500 m with 67.5m tilt (left) and 50.0 m tilt (right).

V. Stratification

Three different density distributions are now imposed on the shelf break grid and compared to the current one. The angle of the thermocline remains 0.013%. The density profiles are derived from the data and occurred on 09 June 2008, 02 June 2009 and 16 March 2008. The solitons observed on these dates are shown in Appendix II. The stratification influences the wave period of the generated solitons.

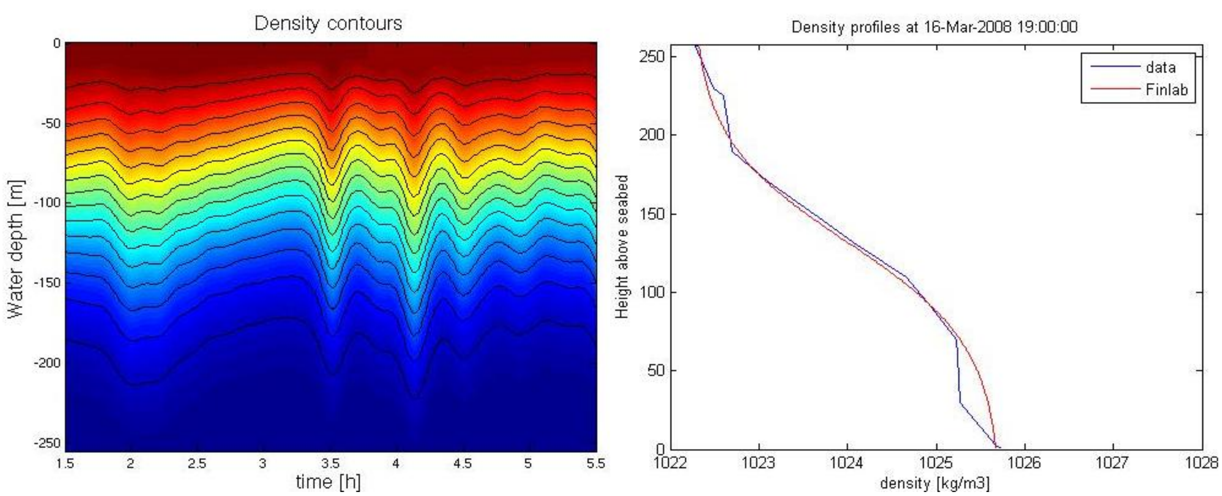

Figure 108. Numerical simulation (left) and stratification (right) on 16 March 2008.

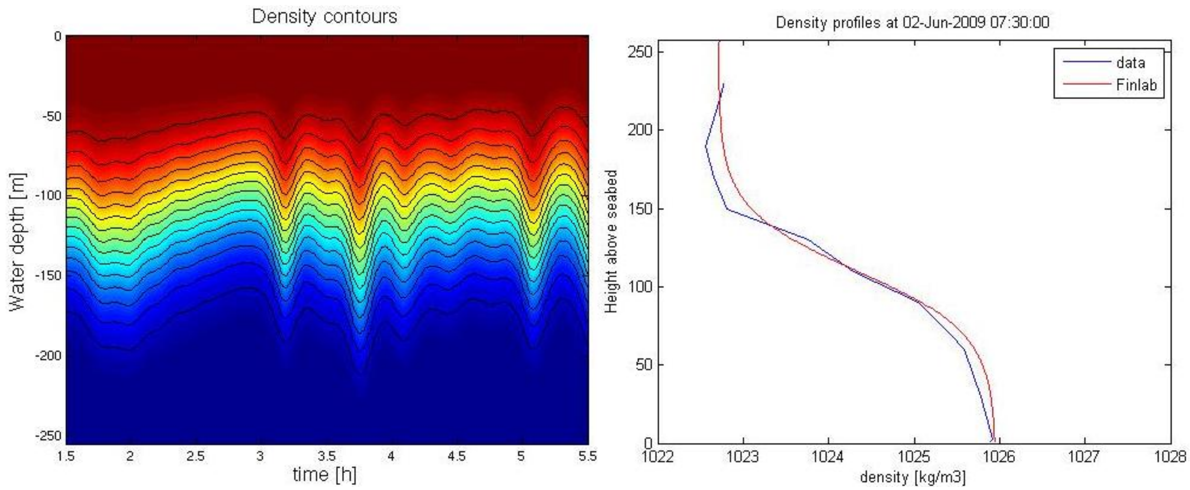

Figure 109. Numerical simulation (left) and stratification (right) on 02 June 2009.

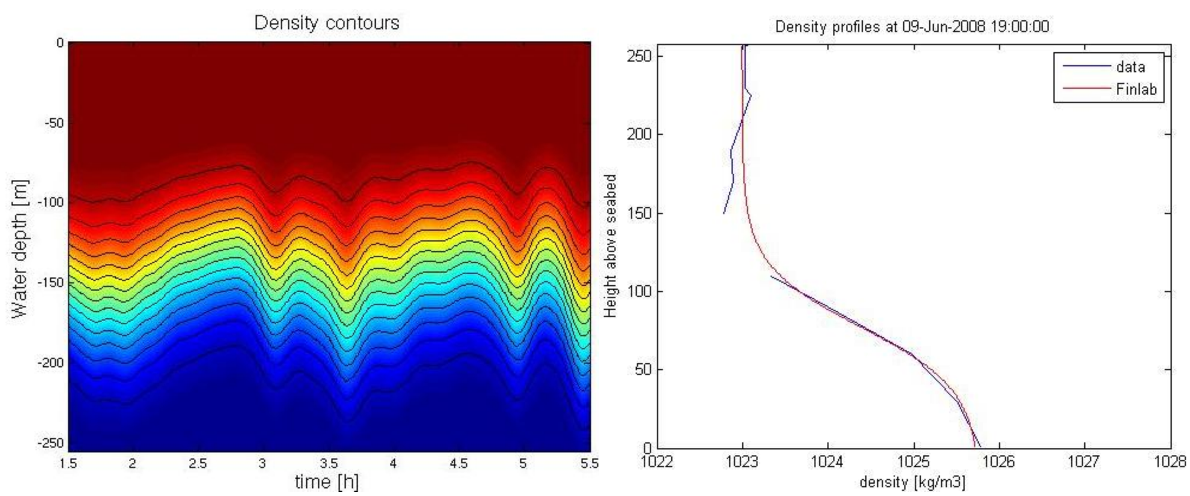

Figure 110. Numerical simulation (left) and stratification (right) on 09 June 2008.